



Séparation des signaux de deux extenseurs des doigts à partir d'électromyogrammes de surface haute densité et modélisation biomécanique du mécanisme extenseur

Anton Dogadov

► To cite this version:

Anton Dogadov. Séparation des signaux de deux extenseurs des doigts à partir d'électromyogrammes de surface haute densité et modélisation biomécanique du mécanisme extenseur. Traitement du signal et de l'image [eess.SP]. Université Grenoble Alpes, 2018. Français. NNT : 2018GREAS034 . tel-02409064v1

HAL Id: tel-02409064

<https://theses.hal.science/tel-02409064v1>

Submitted on 13 Dec 2019 (v1), last revised 18 Dec 2019 (v2)

HAL is a multi-disciplinary open access archive for the deposit and dissemination of scientific research documents, whether they are published or not. The documents may come from teaching and research institutions in France or abroad, or from public or private research centers.

L'archive ouverte pluridisciplinaire **HAL**, est destinée au dépôt et à la diffusion de documents scientifiques de niveau recherche, publiés ou non, émanant des établissements d'enseignement et de recherche français ou étrangers, des laboratoires publics ou privés.

UNIVERSITÉ GRENOBLE ALPES

THÈSE

pour obtenir le grade de

DOCTEUR DE L'UNIVERSITÉ DE GRENOBLE ALPES

Spécialité : Mouvement et Comportement pour la santé et l'Autonomie

Arrêté ministériel : 25 mai 2006

Présentée par

Anton Dogadov

Thèse dirigée par **Franck Quaine** et

codirigée par **Christine Servière**

préparée au sein du

laboratoire Gipsa-Lab

dans l'école doctorale **EDISCE**

Separation of signals from two finger extensor muscles by high-density surface electromyography and biomechanical modeling of the finger extensor mechanism

Thèse soutenue publiquement le **le 25 juin 2018**,
devant le jury composé de :

M. Philippe RAVIER

MCU, HDR, Université d'Orléans, Rapporteur

M. Laurent VIGOUROUX

MCU, HDR, Université Aix-Marseille, Rapporteur

M. Franck QUAINÉ

MCU, HDR, Université de Grenoble Alpes, Directeur de thèse

Mme. Christine SERVIÈRE

Chargée de recherche, CNRS, Codirecteur de thèse

M. Christian JUTTEN

Professeur, Université de Grenoble Alpes, Examineur, Président du jury

M. Roberto MERLETTI

Professeur, École polytechnique de Turin, Examineur

M. Pierre PORTERO

Professeur, Université Paris-Est Créteil, Examineur

M. Francisco VALERO-CUEVAS

Professeur, Université de Californie du Sud, Examineur

M. François MOUTET

Professeur, Université de Grenoble Alpes, CHUG, Invité



UNIVERSITÉ DE GRENOBLE ALPES
ÉCOLE DOCTORALE EDISCE
Ingénierie pour la santé la Cognition et l'Environnement

THÈSE

pour obtenir le titre de

docteur en sciences

de l'Université de Grenoble Alpes

**Spécialité : MOUVEMENT ET COMPORTEMENT POUR LA
SANTÉ ET L'AUTONOMIE**

Présentée et soutenue par

Anton DOGADOV

**Separation of signals from two finger extensor muscles by
high-density surface electromyography and biomechanical
modeling of the finger extensor mechanism**

Thèse dirigée par Franck Quaine et Christine Servière

préparée au laboratoire Gipsa-lab Grenoble Images Parole Signal
Automatique (Grenoble)

soutenue le 25 juin 2018

Jury :

<i>Rapporteurs :</i>	M. Philippe RAVIER	- Université d'Orléans
	M. Laurent VIGOUROUX	- Université Aix-Marseille
<i>Directeur :</i>	M. Franck QUAINÉ	- Université de Grenoble Alpes
<i>Codirecteur :</i>	Mme. Christine SERVIÈRE	- Université de Grenoble Alpes
<i>Président :</i>	M. Christian JUTTEN	- Université de Grenoble Alpes
<i>Examineur :</i>	M. Roberto MERLETTI	- École polytechnique de Turin
<i>Examineur :</i>	M. Pierre PORTERO	- Université Paris-Est Créteil
<i>Examineur :</i>	M. Francisco VALERO-CUEVAS	- Université du Californie du Sud
<i>Invité :</i>	M. François MOUTET	- Université de Grenoble Alpes

Acknowledgements

Firstly, I would like to thank my supervisors Dr. Franck Quaine and Dr. Christine Servière for guiding me through the work on this thesis and sharing with me their knowledge and experience. I deeply appreciate their support and patience.

I spent most of the time of this PhD work in Gipsa-lab, an institution uniting the researches from many different areas, including signal processing and control theory. Besides my supervisors, I met a lot of bright researches, who had an influence on my thesis. I would like to thank Dr. Mazen Alamir for his advices about model parametrization and Dr. Florent Chatelin for his expertise in signal classification. I would also like to thank Anton Andreev in helping me with the experiments carried in Gipsa-lab. I also had a possibility to collaborate with researchers from other laboratories of Grenoble Campus. I would like to thank Dr. Lionel Reveret for the measurement of the finger bone geometrical properties from the computer tomography scans, which he kindly performed. I would like to thank Dr. Jean-Claude Leon for the discussion about numerical methods of the solid properties modeling, that we had. I thank Professor François Moutet for helping me understanding finger anatomy and broadening my knowledge about finger pathologies.

An important part of this thesis was also done in LISiN laboratory (Politecnico di Torino, Italy). I would like to thank Professor Roberto Merletti and Dr. Marco Gazzoni for kindly acquiring me in their lab and helping me in carrying out the experiments and discussing their results. I would like to thank Nicolò Celadon for his assistance with the experiments.

A third part of the work, devoted to extensor mechanism modeling was partially done in Brain-Body Dynamics lab, making part of the University of the Southern California (Los Angeles, USA). I would like to thank Professor Valero-Cuevas for receiving me in the laboratory. I also thank Brian Cohn and Daniel Hagen for discussing finger biomechanics with me.

During the work on this thesis, I had two intern students Mathieu Heberlot in Gipsa-Lab and Vishweshwer Shastri in Brain-Body Dynamic lab. I thank them for their curiosity and their assistance.

I thank the students that I was teaching during the work on this thesis for asking me embarrassing question and I thank Dr. Marion Dohen and Dr. Bertrand Rivet for helping me to answer them.

I thank the committee members for their expertise of the thesis and for their feedback that helped me to improve the manuscript.

I thank Ekaterina Fedina for her drawings made for this thesis.

I apologize to all people that had influence on this work and whom I did not mention in this acknowledgement.

Articles and communications

The results of this thesis were partially presented in following articles and communications:

Journals

1. A. Dogadov, M. Alami, Ch. Serviere, F. Quaine, “The Biomechanical Model of the Long Finger Extensor Mechanism and its Parametric Identification”, Journal of Biomechanics, 2017 [\[paper\]](#)

Conference papers

1. A. Dogadov, Ch. Serviere, F. Quaine, Extraction of EI and EDM muscle sources from surface electromyographic signals using delay estimation. BioSMART, Dubai, UAE, December 2016 [\[paper\]](#)
2. A. Dogadov, Ch. Serviere, F. Quaine, Blind separation of surface electromyographic mixtures from two finger extensor muscles LVA/ICA, Liberec, Czech Republic, August 2015 [\[paper\]](#)

Conferences without proceedings

1. A. Dogadov, M. Alami, F. Quaine, Ch. Serviere, A parametrized model of the long finger extensor mechanism. International Society of Biomechanics Congress. Brisbane, Australia, July 2017 [\[abstract\]](#)
2. F. Quaine, A. Dogadov, C. Serviere, N. Celadon, and M. Gazzoni, “Integration of High Density sEMG and advanced biomechanical model for the study of muscle finger force,” BioSMART, Dubai, UAE, December 2016 [\[abstract\]](#)
3. A. Dogadov, F. Quaine, Ch. Serviere A model of the middle finger extensor mechanism with the retention apparatus. The European Society of Biomechanics Congress. Lyon, France, July 2016 [\[abstract\]](#)

Contents

Part 1. General context.....	6
Introduction	7
Chapter 1. Biomechanical model of the finger.....	9
1.1. Skeleton.....	9
1.2. Tendons	12
1.3. Muscles	14
1.4. Complete finger model.....	18
Chapter 2. Electromyographical signal	19
2.1. Physics of muscle electrical activity	19
2.2. Needle and Surface Electrodes.....	22
2.3. The link between EMG and the force	23
Chapter 3. Crosstalk problem.....	25
Conclusion and problem statement	27
Part 2. Separation of several sources from HD EMG-recordings.....	28
Introduction	29
Chapter 1. MUAP detection and feature estimation.....	31
1.1. Signal acquisition and simulation	31
1.2. MUAPs detection	33
1.3. Feature extraction.....	35
1.4. Performance of the estimation.....	43
1.5. Overlapping of MUAPs from the different MU of the same muscle	47
1.6. Overlapping of MUAPs from different muscles. Crosstalk problem	55
Chapter 2. MUAP Classification.....	63
2.1. Signal acquisition and simulation	63
2.2. MUAP Classification (unmixed case).....	65
2.3. MUAP Classification (mixed case).....	71
Conclusion.....	80
Part 3. The extensor mechanism modelling.....	82
Introduction	83
Chapter 1. Model description	85
1.1. Simulation algorithm.....	85
1.2. Analyzed topologies.....	86
1.3. Force distribution coefficient estimation.....	89
1.4. Tendon moment and fingertip wrench estimation.....	91
Chapter 2. Extensor mechanism simulations	92
2.1. Study of the parameter influence	92
2.2. Study of the postural influence.....	99

2.3. Study of the activation level influence	106
Conclusion.....	111
General conclusion	113
References	116
Annex. Experimental data.....	121

Nomenclature

ARC	Averaged rotation center	MHAT	Mexican hat wavelet
AP	Action potential	MU	Motor unit
CWT	Continues wavelet transform	MUAP	Motor unit action potential
DIP	Distal interphalangeal joint	MVF	Maximum voluntary force
EM	The extensor mechanism	PCSA	Physiological cross-sectional area
EMG	Electromyogram	PIP	Proximal interphalangeal joint
FFS	Feasible force set	RMS	Root-mean-square
FTFS	Feasible tendon force set	sEMG	Surface electromyogram
HD-sEMG	High-density surface electromyogram	SFAP	Single fiber action potential
IRC	Instant rotation center	SL	Segment length
MCP	Metacarpal joint	SNR	Signal-to-noise ratio

Part 1. General context

Introduction

The biomechanical model is a description of the relationship between the muscle forces and the trajectory, torques and forces of the extremity. The current work is devoted to biomechanical model of a finger, which links the forces of the muscles, mobilizing a finger, with the fingertip force. Namely, we will focus on the static problem, when the muscle forces are balanced by external ones and no movement occurs, *i.e.* when a finger applies force against a fixed resistance.

The direct and inverse problem, applied to biomechanical model, may be considered. The direct problem is a problem of calculating the fingertip forces for given muscle forces and chosen posture. The inverse biomechanical problem consists in finding the forces in muscles for given fingertip force and chosen posture.

In the case of direct problem the muscle forces, which are supposed to be known, are used to calculate the fingertip force. This problem can be applied, for example, to a prosthesis control, where solving the direct problem gives the required force, executed by a manipulator. The muscle forces can be estimated from the electromyographical (EMG) recordings, performed either by needle (invasive) electrode, or by the surface ones.

The needle EMG recordings suffer for a number of limitations because of the invasiveness and the non-representation of the whole muscle activity for low muscle contraction. The surface EMG (sEMG) techniques do not have these disadvantages and is more convenient for force estimation. The main limitation of sEMG recordings is that each surface electrode records a signal from a large area that usually contains muscles, other than the muscle of interest. This is a so-called crosstalk problem. Hence, to estimate the force from sEMG recordings, the crosstalk problem must be solved.

Once the muscle forces are known, they may be used as an input of a biomechanical model to estimate a fingertip force. However, the biomechanical model also contains a number of parameters, for example the lengths and shape of segments, stiffness of tendons. The model parameters may have a strong influence on model behavior. Hence, before the model can be used for solving the direct or inverse problem, the parametric identification of the model must be performed. One of the most complicated structures of the finger model with high number of parameters is the extensor mechanism of the finger. It is a complex element of the musculoskeletal apparatus of the finger, which does not have an exhaustive biomechanical description. The extensor mechanism plays an important role in finger extension and even flexion.

In this thesis, we focused on the extensor muscles of index and little finger, *extensor indicis* and *extensor digiti minimi*. These muscles are situated close to each other and create a significant amount of mutual crosstalk. We firstly extracted the activities of each muscle from crosstalk and used a static biomechanical model to link the extracted forces of the extensor muscles with the fingertip force. To model the force transmission by tendons, a biomechanical model of the extensor mechanism was created and parametrized.

The thesis is organized in three parts. Part 1 presents the general context of the work. Part 2 is dedicated to estimation of the individual muscle activities from the signal mixture using high-density

surface EMG recordings (HD-sEMG). Also a method of separating the activities of individual muscles from HD-sEMG signals is presented. Part 3 of the work is dedicated to modeling of the extensor mechanism and its parametric identification.

Chapter 1. Biomechanical model of the finger

The purpose of this chapter is to describe the commonly used biomechanical model of the finger, including bones, tendons and muscles.

1.1. Skeleton

In this section, we will speak about the bones and the joints between them, which introduces the geometrical dependencies to the biomechanical model.

1.1.1. Bones

As in this thesis we will focus only on finger biomechanics, hence we will consider only phalanx bones and a metacarpal one. Each finger, from II to V consists in 3 phalanx bones (distal, medial, and proximal). The proximal phalanx has an articular connection with a metacarpal bone. Each bone consists of base, body and head (Figure 1).

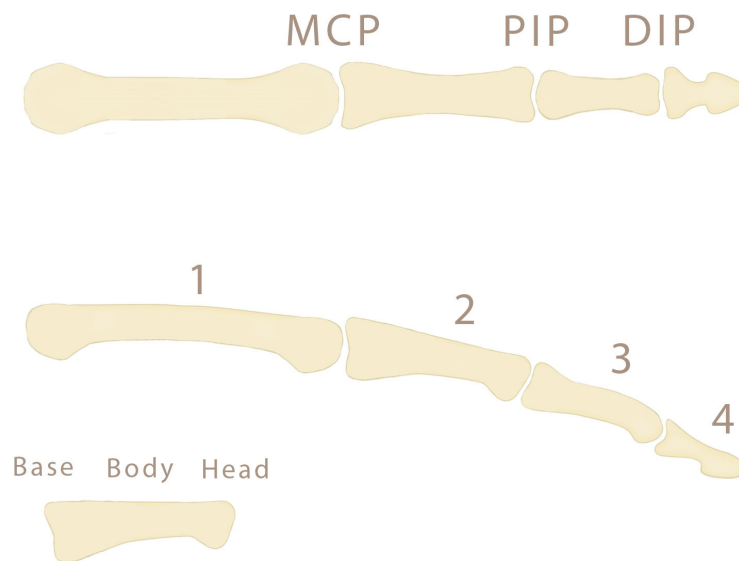


Figure 1 The bones of middle finger and metacarpal bone.

The head of all bones, except distal phalanx has a round prominence, which is called a condyle. Condyles of one bone with joint cavity of the other bone form two surfaces of the joint.

1.1.2. Joints

The finger joints are: metacarpal joint (MCP), proximal interphalangeal joint (PIP) and distal interphalangeal joint (DIP) (see Figure 1). The movement in carpal joints will not be taken into consideration in the current work. To describe the posture of the finger the angles in all finger joints must be defined.

According to geometry of joint surfaces, the finger joints may be divided into two groups:

1. Hinge joint, which enables rotation around one axis – PIP and DIP joints. In the current model they enable rotation only around z axis (see Figure 3);
2. Condylloid joint, which enables rotation around two axis – MCP joint. In the current model it enables rotation around both y and z axis.

At whole, a finger presents thus four rotations. In most of biomechanical studies (Valero-Cuevas et al., 2007; Vigouroux et al., 2007) joints are modeled as ideal constraints. Strictly speaking, it may be true only for joint surfaces, which has constant curvature, *i.e.* we should assume that DIP and PIP joints are ideal circular cylinders and MCP is an ideal sphere. In this case, the rotation center always lies on the cylinder axis or coincide with the center of the sphere. In reality, the joint geometry is more complicated. Hence, it is more reasonably to speak about the instant rotation center of the joints (IRC). Hence, for each constant posture IRC is a point inside the bone head, around which the adjacent bone is rotating, under condition that the rotation angle is infinitely small. Nevertheless, Buchholz et al. (1992) concluded that in most cases, except some critical domains as joint prosthetics, the position of IRC could be assumed as the same for all postures in finger joints. Therefore, an averaged center of rotation (ARC) is a relevant representation of an IRC set. As a conclusion, in the current study we will consider only ARC for the definition of joint center of rotation for the finger joints

The distance between two consecutive ARC is called a segment length (SL). For the distal phalanx, SL is chosen as the distance between ARC₄ and an endpoint, or fingertip (Figure 2).

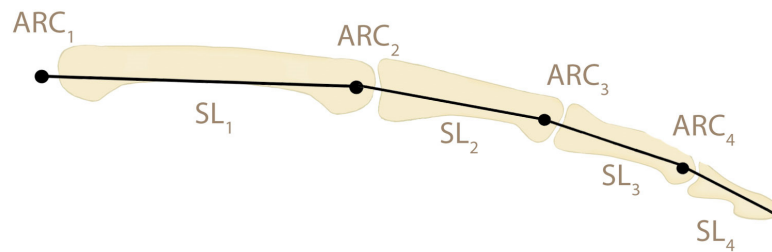


Figure 2. The segment length. Average centers of curvature and segment lengths are shown.

To define the posture, the frames of references (Cartesian coordinate systems) are usually introduced. Each frame of reference is related to one segment. Origins of local frames of reference $O_1 \dots O_4$ correspond to ARC; origin of the last frame of reference O_5 corresponds to an endpoint.

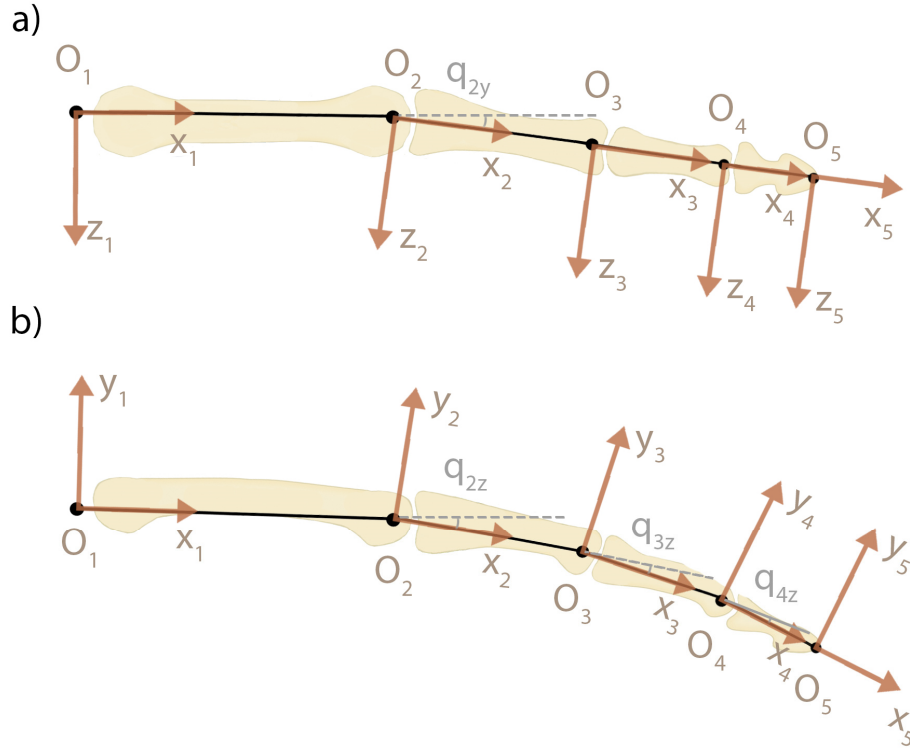


Figure 3. The finger model with five frame of references. The first frame of reference is related to the carpal joint, the last frame of reference is related to the fingertip. a) The XOZ projection; b) The XOY projection.

The global frame of reference must be immobile with reference to a moving finger. We will assume that the first frame of reference with the origin in point O₁ is the global frame of reference.

The vector \mathbf{q} defines the posture uniquely for given segment length:

$$\mathbf{q} = (q_{2y} \ q_{2z} \ q_{3z} \ q_{4z})^T, \quad (1)$$

where q are called the generalized coordinates. In the case of finger biomechanics the generalized coordinates are the joints angles, *i.e.* the angles between the frames of references.

The vector \mathbf{g} defines the endpoint location in global frame of reference. The endpoint of the finger, presented in Figure 3 has four degrees of freedom. Hence, vector \mathbf{g} has four elements:

$$\mathbf{g} = (x_5 \ y_5 \ z_5 \ \alpha_5)^T, \quad (2)$$

where $x_5 - z_5$ are the coordinates of O₅ (endpoint) in the global frame of reference; α_5 is a rotation angle of the distal phalanx in xOy plane. It should be noticed that the angle in xOz plane could not be set independently, hence, this angle is not included to \mathbf{g} .

Finally, the Jacobian must be defined as:

$$\mathbf{J}(\mathbf{q}) = \frac{\partial \mathbf{g}(\mathbf{q})}{\partial \mathbf{q}}. \quad (3)$$

The Jacobian shows how the change in joint angles influences the endpoint location. Moreover, the transpose inversed Jacobian can be used to link the moments in joints, produced by the tendons, with the

forces and moments, produced by the fingertip. This use of the Jacobian is shown in [section 1.4](#) “Complete finger model”.

Thus, in this section the main geometrical relationships were presented. These relationship are introduced to biomechanical model by the bones, which are mobile segments, and joints, who constrain the movement of these segments in space. In the next section, we will speak about the tendons, which transmit muscle forces to finger joints.

1.2. Tendons

The finger is a tendon-driven system (Valero-Cuevas, 2015). It means that the forces, produced by the muscles are transmitted by the means of the tendons.

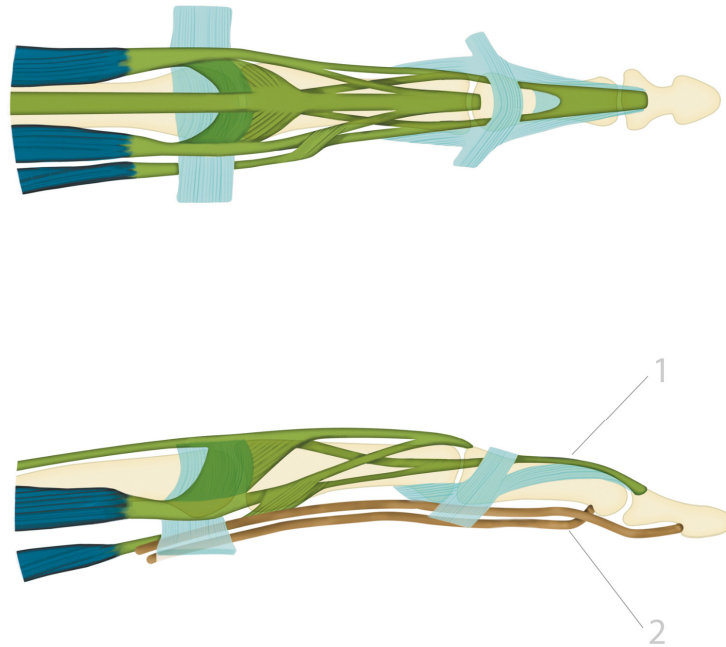


Figure 4. Artist view of the finger tendons. 1 – the extensor mechanism, 2 – flexor tendons (Dogadov et al., 2017)

In the most common case, tendons are modeled as strings (Valero-Cuevas et al., 2007). Hence, the moments, created by the tendon, crossing the joint may be calculated as a vector product of the force in the tendon and a moment arm:

$$\vec{M} = \vec{r} \times \vec{f}. \quad (4)$$

Instead of the using the moments in vector form, as written in (4), only scalar values of the moment may be kept. One can only calculate the scalar value of the moment around z axis for hinge joints (PIP, DIP) and the values of the moment around y and z axis for condyloid joints (MCP).

Hence, the equation (4) may be generalized in the matrix form to represent the relationship between the forces in tendons and moments in all joints, created by them.

$$\mathbf{m}(\mathbf{q}) = \mathbf{R}(\mathbf{q})\mathbf{f}, \quad (5)$$

where \mathbf{f} – the forces in tendons; \mathbf{m} – the moments in all joints; \mathbf{R} – a matrix of moment arms.

In the case of finger, the vectors \mathbf{m} , \mathbf{f} and matrix \mathbf{R} become:

$$\mathbf{m} = \begin{pmatrix} m_1^y \\ m_1^z \\ m_2^z \\ m_3^z \end{pmatrix}, \mathbf{R} = \begin{pmatrix} r_{11}^y & r_{12}^y & \cdots & r_{1N}^y \\ r_{11}^z & r_{12}^z & \cdots & r_{1N}^z \\ r_{21}^z & r_{22}^z & \cdots & r_{2N}^z \\ r_{31}^z & r_{32}^z & \cdots & r_{3N}^z \end{pmatrix}, \mathbf{f} = \begin{pmatrix} f_1 \\ f_2 \\ \vdots \\ f_N \end{pmatrix}, \quad (6)$$

where m_1^y and m_1^z are the moments in MCP around y and z axis correspondingly; m_2^z is a moment in PIP and m_3^z is a moment in DIP joint; f_i is the force in i -th tendon.

1.2.1. Finger flexor tendon forces

The flexor tendons are the tendon of *flexor profundus* and *flexor superficialis*. The flexor tendons are supported by a sequence of pulleys (Doyle, 1989; Moutet, 2003). It is usually considered that the forces in flexor tendons are equal to the forces in corresponding muscles:

$$\begin{cases} f_{fp} = \varphi_{fp} \\ f_{fs} = \varphi_{fs} \end{cases}, \quad (7)$$

where f_{fp} – force in the *flexor profundus* tendon, f_{fs} – force in the *flexor superficialis* tendon; the muscle forces are: φ_{fp} – force of *flexor profundus* muscle, φ_{fs} – force of *flexor superficialis* muscle.

1.2.2. Finger extensor tendon forces

The extensor tendons form the so-called extensor mechanism of the finger. The extensor mechanism is a complex tendinous structure, situated in the dorsal part of each finger. This structure combines forces of extrinsic extensors and intrinsic muscles. The biomechanical modeling of this structure is performed in the Part 2 of this thesis. The extensor mechanism is connected with the flexor tendons by the means of the transverse retinacular ligament.

The extensor mechanism is usually introduced by an equation system proposed by Chao et al. (1989) which represents the internal-force distribution in the tendon network. With the experimentally obtained coefficients, this system becomes (8) for the long finger in the extended posture:

$$\begin{cases} f_{te} = 1.000 f_{ub} + 1.000 f_{rb} \\ f_{rb} = 0.167 \varphi_{ed} + 0.133 \varphi_{ri} + 0.667 \varphi_{lu} \\ f_{ub} = 0.313 \varphi_{ui} + 0.167 \varphi_{ed} \\ f_{me} = 0.313 \varphi_{ui} + 0.167 \varphi_{ed} + 0.133 \varphi_{ri} + 0.333 \varphi_{lu} \end{cases}, \quad (8)$$

where f_{te} – force in the terminal extensor tendon te (10 in Figure 4), f_{rb} – in the radial lateral band rb (9, radial side), f_{ub} – in the ulnar lateral band ub (9, ulnar side), f_{me} – in the medial extensor tendon me (6); the muscle forces are: φ_{ui} – force of ulnar dorsal interosseus ui (13), φ_{ed} – force of extensor digitorum ed , φ_{ri} – force of radial dorsal interosseus ri (15), φ_{lu} – force of lumbrical lu (16).

The equations, linking the forces in flexor and extensor tendons and in muscles may be generalized in matrix form. The matrix $\mathbf{E}(\mathbf{q})$ may be introduced that will link the vector \mathbf{f} of tendon forces with muscle force vector $\boldsymbol{\varphi}$:

$$\mathbf{f}(\mathbf{q}) = \mathbf{E}(\mathbf{q})\boldsymbol{\varphi}. \quad (9)$$

The matrix $\mathbf{E}(\mathbf{q})$ is posture dependent, especially because of the extensor mechanism deformation with posture. The force distribution among the extensor mechanism and, hence, the coefficients in the equations (8) are known to depend on posture (Hurlbut and Adams, 1995). However, the values of these coefficients were experimentally defined by Chao et al. (1989) only for extension posture and there is a lack of biomechanical studies, defining their values for other postures than extension. In some biomechanical studies (Brook et al., 1995; Vigouroux et al., 2007) these coefficients are determined for various finger postures using the optimization procedures. However, no deep analysis of determined coefficients has been performed, making their relevance hard to determine.

The Part 3 of this thesis is devoted to creating a precise model of the extensor mechanism, which will be used to simulate the force distribution among the tendons for all feasible physiological postures.

In this section, we firstly discussed how the moments in joints depend on forces in tendons and, secondly, how the latter depends on muscle forces $\boldsymbol{\varphi}$. The next section will present the muscles and discuss the factors, which influence the muscle force.

1.3. Muscles

Muscles are the actuators, creating forces in tendons. Below we discuss how the muscle capacities depend on its biomechanical and anatomical properties at different organizational levels.

1.3.1. The force of individual fiber

Muscles contain muscle fibers (muscle cells, myocyte), which are structural elements of muscle tissue. Muscle fibers contain sarcoplasm, which is a cytoplasm of a muscle fiber. The sarcoplasm is filled by myofibrils, which are long protein cords. Myofibrils are composed of contractile elements. The length of muscle fiber vary from 1 to 500 mm in length and from 10 to 60 μm in diameter (Kandel et al., 2013).

According to its properties, muscle fibers can be divided into two types: type I (low force, low fatigue) and type II (high force, high fatigue).

The muscle fibers are associated in motor units (MU), which are the sets of fibers, innervated by the same motoneuron. MU are the smallest functional elements of muscle.

1.3.2. The force of individual motor unit

All fibers belonging to a MU have similar properties and belong to the same type (I or II). A number of fibers in one MU is called an innervation number. MUs of one muscle have an innervation number, varying in wide range (approximately from 21 to 1770 for first dorsal interosseous muscle (Kandel et al., 2013)). It means that the properties of different MUs across the muscle are different.

The MU response to an action potential (AP) arriving from a motoneuron by a short contraction, known as a twitch contraction. To maintain a force for longer time, motoneuron sends a series of action potentials to a MU. Twitch contractions of each AP superimpose to form a tetanic contraction, or tetanus (Figure 5).

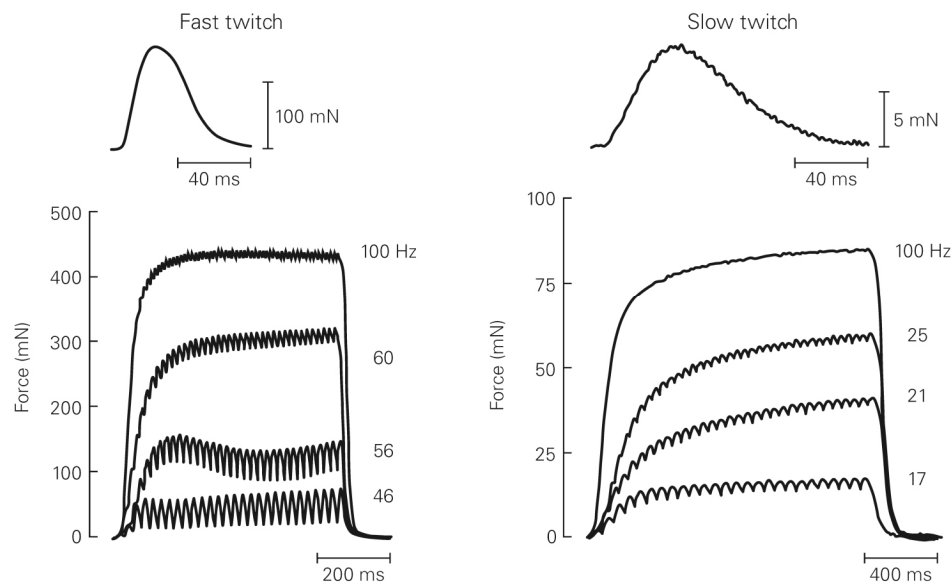


Figure 5. The twitch contraction (upper row) and tetanic contraction (lower row) of fast MU (left column) and slow MU (right column). Adapted from (Botterman et al., 1986).

1.3.3. The resulting force of a muscle

This resulting force of a muscle is a vector sum of the forces of parallel muscle fibers. The nervous system controls the muscle force by varying the frequency of AP sequence and varying of number of recruited MUs. The muscle capacities, such as maximal force, range of motion and shortening velocity depend on:

1. Muscle properties;
2. Muscle state (length and velocity);

Muscle properties depend on characteristics of individual muscle, such as pennation angle, physiological cross-sectional area of muscle (PCSA), ratio of fibers of type I and type II. PCSA takes into account the muscle cross-action and a pennation angle.

Variation of muscle force with muscle length and contraction velocity are similar for all muscles and are related to particularities of contractile element functioning (Figure 6).

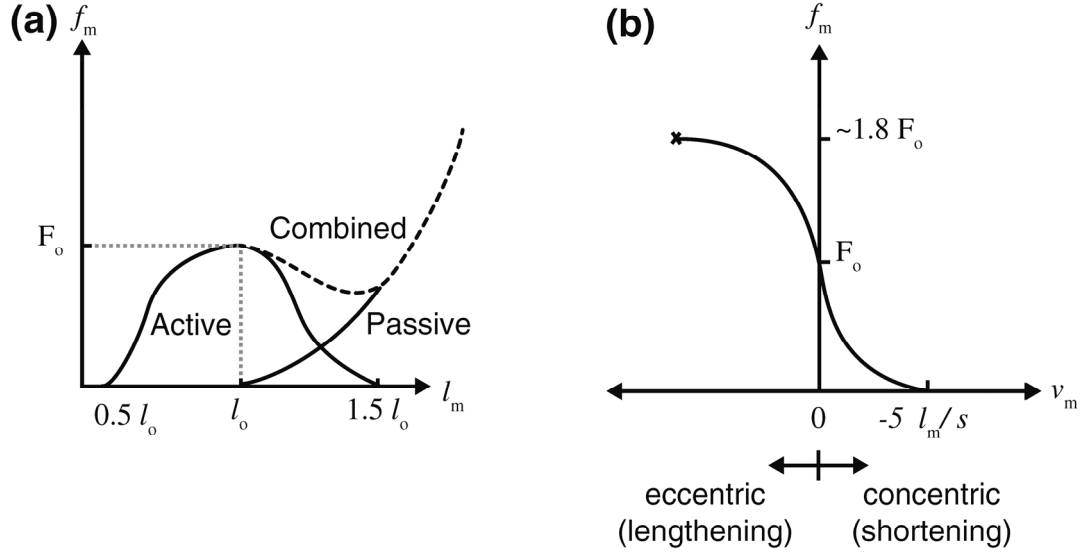


Figure 6. The force-length (a) and force-velocity (b) relationship for a muscle. Adapted from (Valero-Cuevas, 2015).

The above-listed factors determine the muscle capacity to produce movement and define maximal force that can be produced by muscles in given state. However, the muscle force depend also on voluntary (or involuntary in case of a spasm, for example) activation command. The activation command a_i shows the level of activation of i -th muscle in relative values from 0 to 1. The muscle force may be related with activation command as follows:

$$\varphi_i = PCSA_i \cdot \sigma_i \cdot a_i, \quad (10)$$

Where σ_i is a maximal feasible muscle tension, which is usually fixed at 35 N/cm^2 for the finger muscles (Zajac, 1989).

In matrix form, the muscle forces may be related with the activation command by the following relationship.

$$\boldsymbol{\varphi}(\mathbf{q}) = \mathbf{F}(\mathbf{q})\mathbf{a}. \quad (11)$$

Where \mathbf{a} is the activation vector, \mathbf{F} is a diagonal matrix, which transforms the activation vector into a force vector. The matrix \mathbf{F} contains the information about the muscle capacity of force producing, which depends on muscle anatomy. Moreover, \mathbf{F} is posture \mathbf{q} dependent for static problems (and also depends on $\dot{\mathbf{q}}$ for dynamic ones) because of force-length and force-velocity relationships (Fenn and Marsh, 1935; Hill, 1938, 1922).

1.3.4. Finger muscles

Each finger is controlled by extrinsic and intrinsic muscles. The list of these muscles are given in Table 1. This table also gives PCSA of each muscle.

Table 1. A list of muscles, mobilizing fingers II-V, with their PCSA (Chao, 1989).

Finger	Muscle name	PCSA (cm ²)
Index	<i>Extensor digitorum communis II</i>	1.1±0.3
	<i>Extensor indicis</i>	1.3±0.6
	<i>Flexor digitorum profundus II</i>	4.1±2.4
	<i>Flexor digitorum superficialis II</i>	3.6±2.1
	<i>Lumbrical</i>	0.3±0.1
	<i>Dorsal interosseous I</i>	2.1±0.5; 2.0±0.8; 0.1±0.2 ¹
	<i>Palmar interosseous I</i>	1.4±0.4
Long	<i>Extensor digitorum communis III</i>	1.7±0.8
	<i>Flexor digitorum profundus III</i>	4.1±1.4
	<i>Flexor digitorum superficialis III</i>	4.2±1.8
	<i>Lumbrical</i>	0.2±0.1
	<i>Dorsal interosseous II</i>	1.4±1.0; 1.4±0.8; 0.7±0.4 ¹
	<i>Dorsal interosseous III</i>	1.0±0.8; 1.2±0.7; 0.7±0.2 ¹
Ring	<i>Extensor digitorum communis IV,</i>	1.2±0.4
	<i>Flexor digitorum profundus IV</i>	3.7±1.1
	<i>Flexor digitorum superficialis IV</i>	2.4±1.2
	<i>Lumbrical</i>	0.2±0.1
	<i>Dorsal interosseous IV</i>	1.1±0.8; 1.1±0.7; 0.6±0.2 ¹
	<i>Palmar interosseous II</i>	1.2±0.3
Little	<i>Extensor digitorum communis V</i>	0.5±0.8
	<i>Extensor digiti minimi</i>	1.5±0.9
	<i>Flexor digitorum profundus V</i>	2.5±0.9
	<i>Flexor digitorum superficialis V</i>	2.1±1.4
	<i>Lumbrical</i>	0.2±0.1
	<i>Abductor digiti minimi</i>	0.8±0.3; 0.9±0.2 ²
	<i>Palmar interosseous III</i>	1.3±0.4

¹Radial head; ulnar head; superficial head

²Superficial head; deep head

Hence, the muscles were presented in this section. The final section of this chapter is devote to complete finger model, linking the forces in individual muscles with the fingertip wrench.

1.4. Complete finger model

In this section, a complete static model of the finger will be discussed. In most common case, this model links a set of muscle forces with a fingertip wrench vector \mathbf{w} , produced by a fingertip. Vector \mathbf{w} includes all feasible forces and moments, produced by a fingertip.

$$\mathbf{w}(\mathbf{q}) = \begin{pmatrix} F_5^x & F_5^y & F_5^z & M_5 \end{pmatrix}^T. \quad (12)$$

The fingertip wrench vector \mathbf{w} is linked with the joint torques \mathbf{m} by an inverse transposed Jacobian:

$$\mathbf{w}(\mathbf{q}) = \mathbf{J}(\mathbf{q})^{-T} \mathbf{m}, \quad (13)$$

The torques in the joints \mathbf{m} depend on forces in tendons \mathbf{f} and moment arms \mathbf{R} , and may be found using (5). By replacing the moments in joints by tendon forces, (13) transforms to:

$$\mathbf{w}(\mathbf{q}) = \mathbf{J}(\mathbf{q})^{-T} \mathbf{R}(\mathbf{q}) \mathbf{f}, \quad (14)$$

The forces in tendons \mathbf{f} are related with muscle forces $\boldsymbol{\phi}$ by equation (9). Hence, (14) becomes:

$$\mathbf{w}(\mathbf{q}) = \mathbf{J}(\mathbf{q})^{-T} \mathbf{R}(\mathbf{q}) \mathbf{E}(\mathbf{q}) \boldsymbol{\phi}, \quad (15)$$

Finally, the muscle forces may be expressed in terms of muscle activations. Hence, replacing in (15) the muscle forces by muscle activations, one obtains:

$$\mathbf{w}(\mathbf{q}) = \mathbf{J}(\mathbf{q})^{-T} \mathbf{R}(\mathbf{q}) \mathbf{E}(\mathbf{q}) \mathbf{F}(\mathbf{q}) \mathbf{a}, \quad (16)$$

It should be emphasized that in this equation, matrices \mathbf{J} , \mathbf{R} , \mathbf{E} , and \mathbf{F} are posture \mathbf{q} dependent. However, hereinafter the argument \mathbf{q} will be omitted for simplicity.

The equation (16) transforms the vector of activations \mathbf{a} ($1 \times M$) to an output wrench vector \mathbf{w} ($1 \times N$). As M is usually bigger than N , the direct problem (16) is an overdetermined problem and, vice versa, the inverse problem is an underdetermined problem, which has an infinite number of solutions. Most advanced used method of the inverse biomechanical problem solving take into account motor control strategies and use the electromyographical signals as indicators of muscle activity (Paclet and Quaine, 2012; Vigouroux et al., 2007).

This chapter was devoted to biomechanical model of the finger. We presented how the muscle forces are transmitted to finger joints by the means of tendons. The equation, linking muscle forces with the fingertip wrench was also given. Furthermore, in addition to mechanical work, muscles produce the electrical signals, electromyogram, which is presented in the next chapter.

Chapter 2. Electromyographical signal

In this chapter, we discuss the electrical effects, which accompany force production by the muscle. We firstly discuss how the electrical effects in muscle fibers occurs and how they are mapped into the electrical potential on the skin. The potentials may be observed only by means of an electrode system, either surface or invasive. This observation is not a pure potential, created by physiological activity in one particular point, but a result of interaction between the electrode surface and medium. The distortions, introduced by the electrode, are discussed later in this chapter. Finally, we discuss the relationship between the observed electrical activity and the muscle force. The important problem of interference from nearby muscles, which occurs during signal acquisition, is presented in the next chapter.

2.1. Physics of muscle electrical activity.

In this section, we speak about the physics of electrical activity of the muscle. This section is organized in the same way as a section, devoted to muscle biomechanics. We will start the description from a fiber to finish with a whole muscle.

2.1.1. The action potential of individual fiber

The action potential (AP) arrives from motoneuron to a motor end plate (or neuromuscular junction) of muscle fiber. It results in a local depolarization of the outer muscle-fiber membrane (the sarcolemma), also known as single fiber action potential (SFAP). The resulting depolarized zone, which has length of few millimeters, starts to propagate along the muscle fiber from the neuromuscular junction to the tendon ending. The velocity with which the action potential propagates depends on the fiber diameter and type and is called a conduction velocity (CV). The typical CV values are 3-5 m/s (Merletti and Parker, 2004). Figure 7 illustrates a depolarized zone of a muscle fiber.

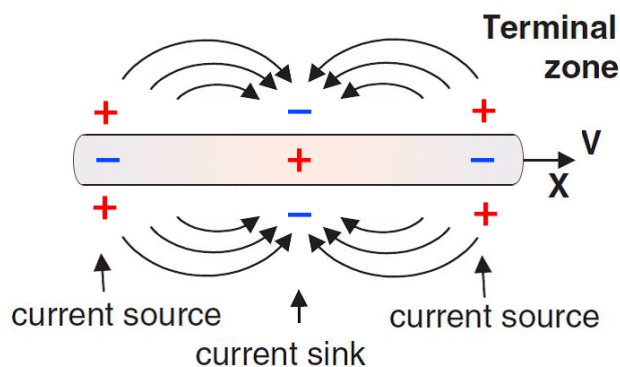


Figure 7. A depolarized zone in a muscle fiber

When the SFAP stops at the tendon junction, it generates a non-propagating burst, which may have different form at different locations. This phenomenon is known as end-of-fiber effect (Merletti and Parker, 2004)

The sources of the signal are separated from the recording electrodes by biological tissues, which act as volume conductor. The volume conductor has an effect of spatial low-pass filters on the spatial potential distribution ϕ , created by a SFAP over the skin (Merletti and Parker, 2004).

2.1.2. The action potential of individual motor unit

This translation from single fiber to MUAP is not simply the amplification of SFAP amplitude. The conduction time for different APs may be different because the differences in propagation velocity and in travelling distance. These differences are results of the variability of fiber diameters, lengths, and to end-plate locations. Hence, the constituent APs, generated by different fibers of the MU, are not perfectly synchronous. Consequently, the waveform of a MUAP is more complicated than a waveform of composing SFAPs (Figure 8). Furthermore, there is a great variability among the MUAPs of different MUs of one muscle.

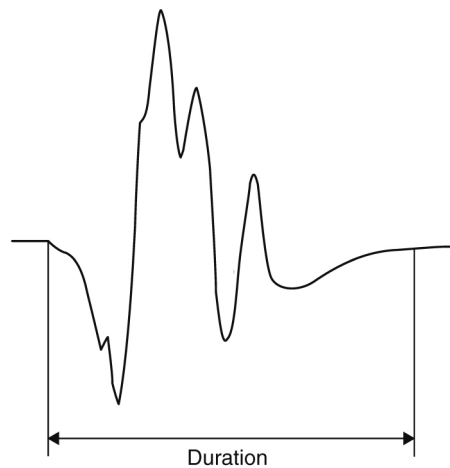


Figure 8. A MUAP. Adapted from Merletti et al., 2004

2.1.3. The resulting interferential pattern of a muscle. sEMG signal

All active MUs in the muscle contribute in creating an interferential pattern, which is a distribution of the potential on the skin. This pattern is the result of many physiological and anatomical factors, among them the firing behavior of MUs and fiber type composition of the muscle (de Luca, 1997). When these potentials are recorded from the skin, the obtained signal is called a surface electromyographic signal, or sEMG. The schematic representation of the EMG signal production is given in Figure 9. The interferential EMG is shown to be a sum of MUAP train from different MUs of the muscle.

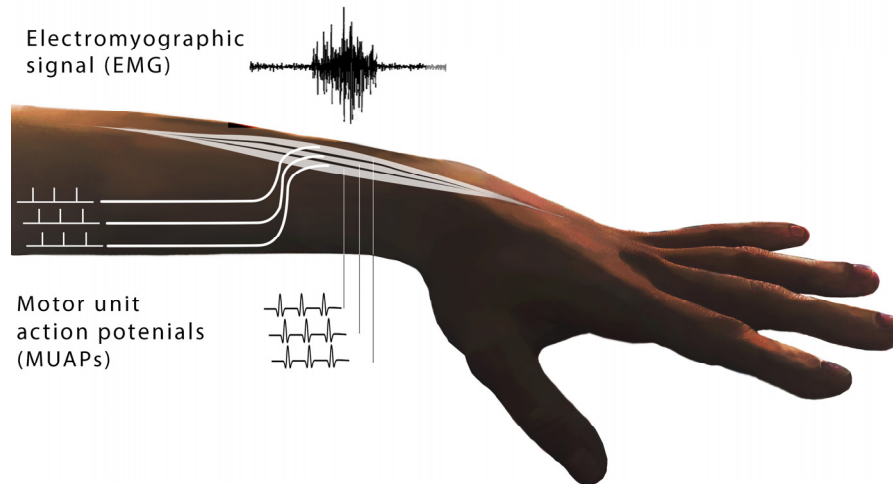


Figure 9. The schematic representation of the EMG signal production

The distribution of the potential on the skin is not homogenous over the muscle. Along the muscle axis the signal RMS is highest near the innervation zone and decreases to myotendinous junction. Along the transversal axis the RMS decreases from muscle center to lateral edge. (Figure 10).

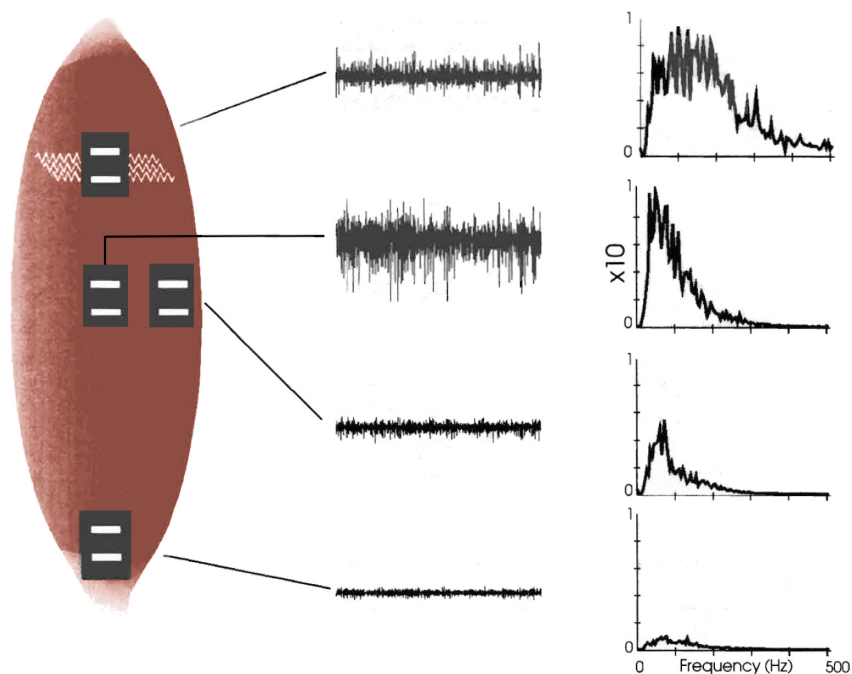


Figure 10. Differences in sEMG signal recorded from different regions of a muscle. Adapted from (de Luca, 1997).

The signal spectrum lies below 400 Hz and the median frequency shifts with fatigue.

As sEMG is a sum of MUAP from many MUs, MUAPs from different MU can overlap, distorting the form of MUAPs.

2.2. Needle and Surface Electrodes

Muscle activity creates the distribution of the electric potential over the skin and inside the tissues. These potentials are recorded by the means of electrodes, either intramuscular (invasive, needle), or surface (noninvasive). As the observed electrical activity strongly depends on electrode type, we will briefly present describe the influence of electrode properties on recorded signal.

2.2.1. Intramuscular electrodes

Intramuscular electrodes are usually used in clinical conditions to study the physiology and pathology of the MU. For example, by means of intramuscular electrodes one can study loss of nerve supply to the muscle, the ability of the nerve to regenerate, diseases affecting the muscle fiber itself, diseases of the neuromuscular junction, and MU recruitment and firing patterns.

There exists several types of intramuscular electrodes: macro electrodes, the concentric needle electrode, the monopolar needle electrode, and single-fiber needle electrodes. These electrodes differ by recoding area size (listed in recoding area descending order (Merletti and Parker, 2004)).

When used in biomechanical studies the electrodes which larger recording area may be preferable. For example, Vigouroux et al. (2007) used concentric needle electrodes with 0.07 mm^2 recording area to estimate finger flexor and extensor muscle activation.

However, needle electrodes have several limitations. Firstly, they usually do not cover the whole area of muscle; secondly, recording may be difficult to perform in dynamic conditions, as the electrode is situated inside the contracting muscle body; finally, the procedure is usually painful for a subject, hence it may be difficult to place too many intramuscular electrodes during an experiment. Hence, the surface electrodes seem more appropriate for biomechanical studies.

2.2.2. Surface electrodes: Monopolar and differential

Surface electrodes are usually better suited for studies focused on activity of the muscle as a whole.

The signals may be recorded either in monopolar or in differential scheme. In the case of monopolar recordings, each signal is a difference of the electrical potentials between one signal electrode and a reference electrode with respect to a ground electrode. In differential case, each signal is a potential difference between two signal electrodes, situated close to each other, with respect to a ground electrode

Although all advantages, surface electrodes can distort the sEMG signal because of several factors, which should be taken into account when working with surface electrodes.

First of all, it should be noticed that the potential recorded by an electrode is an average of the potential over the electrode area. Hence, bigger the electrode is, larger is area of averaging and less is the electrode's selectivity. Secondly, the metal surface in contact with the skin will force the area of contact to be equipotential, therefore modifying the skin potential distribution in the neighborhood (Merletti and Parker, 2004). Thirdly, the capacitive component of the electrode-skin component is important in EMG frequency. Finally, there exist so called "battery effect", related to DC voltage at metal-electrolyte contact.

This voltage may disappear if it is the same at both electrodes in a differential pair (or in a signal and a reference electrode). Otherwise, this voltage stays uncompensated.

To analyze the activity of the whole muscle the matrices of monopolar electrodes may be more informative, as they provide information about the activity of the muscle as a whole, and at the time they have a high spatial resolution.

2.2.3. Matrix of monopolar electrodes

The matrix of monopolar electrodes (Figure 11) can represent an activity of the muscle as a whole, providing information about the potential in high number of individual locations over the skin. The size of electrodes in the matrix is usually sufficiently small to distinguish the activity of individual motor units.

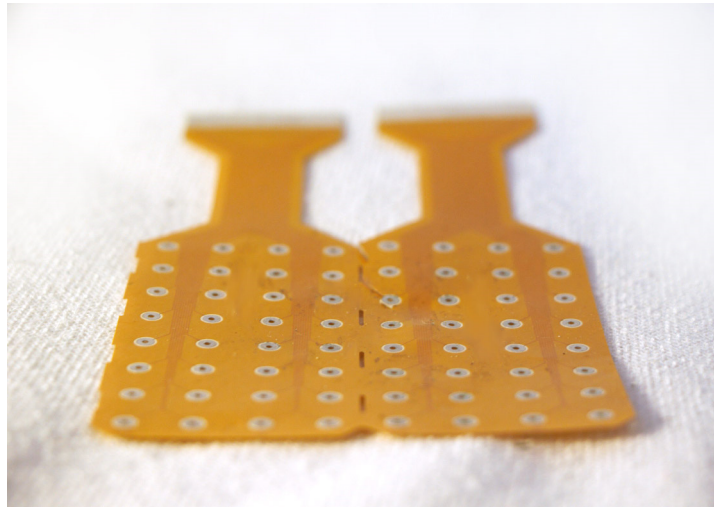


Figure 11. The 8-by-8 HD EMG matrix with 10 mm interelectrode distance, developed in LISiN

The signal from electrode matrix provides information about the change of the potential in both time and in space. Furthermore, we will call “a map” the recorded distribution of the potential over the space, either instantaneous or averaged during a certain time window. Hence, the Nyquist criterion must be satisfied in both frequency domain (by choosing appropriate sampling frequency) and spatial frequency domain (by choosing appropriate interelectrode distance).

Moreover, the electrodes act like filters in spatial domain. Hence, the form of electrode changes the transfer function of the filter and has an important influence on recorded potential map.

2.3. The link between EMG and the force

There is a monotonic relationship between the RMS (or envelope) of sEMG and force of muscle. This relationship depends on anatomical and detection conditions.

$$a_m(t) = \alpha \hat{s}(t)^\beta, \quad (17)$$

where \hat{s} is an envelope of EMG, a_m – muscle activation, β – parameter.

This function can represent all possible relationships, which are linear, non-linear with upward concavity, and non-linear with downward concavity.

Linear relationship between the force and envelope of EMG signal ($\beta = 1$) was used in a number of studies and represent a sEMG-force relationship for most biomechanical problems. However, nonlinear relationship ($\beta \neq 1$), may be more general approximation of a sEMG-force relationship (Botter et al., 2011).

It should be also noted that there is a delay between muscle activation, detected by the EMG signal and determined by muscle force generation (de Luca, 1997).

This chapter briefly presented the physics and physiology of the EMG signal generation. We also observed the models that links muscle activation with EMG signals. However, these models may be properly applied only if the sEMG recordings contain only the signals from the muscle of interest. However, it is not always the case, especially for the hand muscles. In the hand, there is a high number of muscles, located in the limited volume. Therefore, these muscles are the sources of mutual crosstalk. Hence, before the EMG recording may be used for the force estimation, the signals of individual muscles must be firstly extracted from a signal mixture, or crosstalk reduction. The next chapter of the introduction presents the crosstalk problem and the methods, used for crosstalk reduction.

Chapter 3. Crosstalk problem

Surface electromyographic signals (SEMG) are widely used in medicine, prosthesis control and biomechanical studies (Holobar and Farina, 2014). Integrated SEMG (IEMG) is commonly used in biomechanics as an estimator of muscle activations (Léouffre et al., 2013). Muscle activations, denoted as \mathbf{a} , may be reconstructed from the measured muscle EMG activity \mathbf{s} using a model $f(\mathbf{s})$:

$$\mathbf{a} = f(\mathbf{s}) + \mathbf{n}, \quad (18)$$

where \mathbf{n} is noise.

However, when estimating the activity of muscles situated close to each other, crosstalk is a significant issue because it reduces the accuracy of sEMG-based force estimation. In this case, instead of recording pure EMG activity \mathbf{s} one records signal mixtures \mathbf{x} ,

$$\mathbf{x} = \mathbf{B}\mathbf{s} + \mathbf{n}, \quad (19)$$

where \mathbf{B} is a mixing matrix.

In particular, the sEMGs from hand muscles suffer from this problem (Léouffre et al., 2013; Mesin et al., 2009) because of the high number of muscles situated in the forearm. Figure 12 gives an illustration of the crosstalk problem. Two electrodes shown by circles record the activity of two muscles. Each electrode captures the signal from the closest muscle (the muscle of interest) as well as from the nearby muscle (crosstalk).

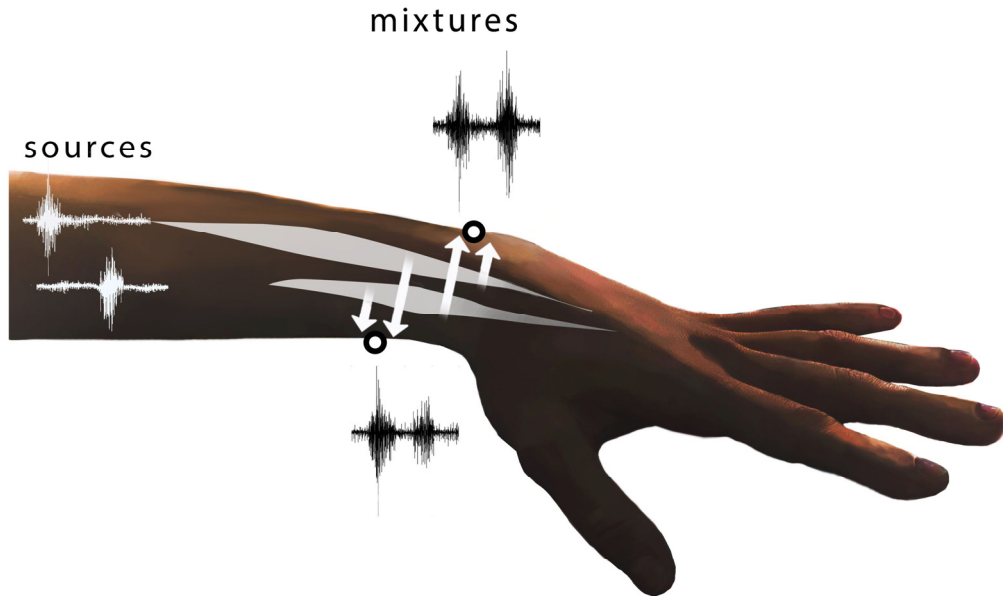


Figure 12. The schematic representation of the crosstalk problem

This effect may cause precision decrease of IEMG-based force estimations.

Several approaches may be used to reduce the crosstalk from different muscles. Among them, there are instrumental methods, such as using differential and double differential electrode systems, which reduces the amount of signals captured from distant muscles. Moreover, a special attention must be paid to proper electrode placement. From the other hand, there are computational methods, such as blind source separation methods (BSS). These methods may perform additional crosstalk reduction once the instrumental methods were applied.

BSS is a method of source signal recovering from several mixtures when no a priori information is available on source properties (source spatial position etc.). To reduce the crosstalk from neighbor muscles BSS is applied to mixtures, in which each muscle is thought to be a source, and mixture signals are thought to be transformed vectors of source signals. Most of mixing transformations are supposed to be linear, instantaneous or convolutive. A linear instantaneous model can be used in the case of small muscles located close to each other (Farina et al., 2004). However, validity of the instantaneity hypothesis is very sensitive to electrode location (Léouffre et al., 2013). Merletti (Merletti et al., 2008) explained the limitations of the instantaneous model by a convolutive effect of a volume conductor and by action potential propagation.

To estimate the source signals Independent component analysis (ICA) is usually used. ICA is a group of methods, aimed to transform a set of recordings into a set of independent source signals. ICA could be performed in time-domain if instantaneous model is chosen, or in time frequency domain in the case of convolutive model. Different types of diversity can be used to perform ICA: non-gaussianity (Infomax, FastICA, EFFICA, JADE, EBM, RADICAL etc), sample dependence (AMUSE, SOBI, WASOBI etc) or nonstationarity.

The number of studies uses the first type of diversity to perform BSS on EMG signals. Naik et al (2016) performed a comparison of JADE, FastICA and Infomax ICA methods. They applied ICA on EMG signals, preliminary decomposed into intrinsic mode functions by the ensemble mode decomposition algorithm. The separated sources were used to classify each EMG recording as normal or pathological one. The classifications performance was significantly higher when FastICA method was used.

The methods, using the second type of diversity were also used to separate the EMGs. Jiang and Farina (2011) proposed an extension of a BSS technique based on second-order moments (SOBI) for the case of sources being delayed in the mixtures. The proposed method was based on the transformation of the delayed mixtures to the mixtures of original sources and their first derivatives by the first-order Taylor approximation. The method is applicable only to mixtures with small delay.

The application of ICA was developed by Farina et al (2004). They investigated linear mixtures of EMG signals using Spatial Time-Frequency Distribution of EMG.

However, blind source separation methods based on source independence (Léouffre et al., 2013) may fail in separation of the signals from individual muscles because each muscle consists of motor units, which also may be considered as individual sources by a source separation algorithm. Hence, there is no evidence if the separated sources are the signals produced by different muscles or from different motor units (MU) of the same muscles. Moreover, the question if the EMG signals produced by different muscles are always statistically independent remains open.

Conclusion and problem statement

In the current thesis, we firstly extracted the activities of little and index finger extensor muscles from a mixture and, secondly, proposed a biomechanical model of the extensor mechanism that transmits the extensor muscle forces to a fingertip force. According to this order, the main body of the thesis is structured in two parts, Part 2 and 3 (Figure 13).

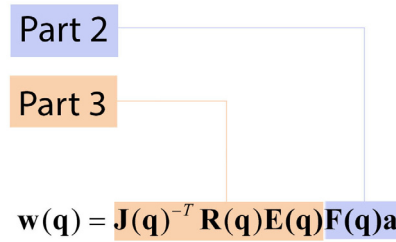


Figure 13. The structure of the thesis

Part 2 deals with extraction of activations of extensor muscles from the signal mixtures, recorded using the HD-EMG techniques. The signals were recorded from the extensors of index and little finger, which are situated close to each other and are strong mutual crosstalk sources. To extract the individual muscle activations from the mixture, the MUAPs were detected in mixtures and classified according to a source muscle. Finally, the activity of individual muscles were reconstructed. The HD sEMG signals, used in this part, were acquired in collaboration with LISiN laboratory (Turin, Italy) using the electrode matrices and acquisition system, developed by LISiN team

Part 3 presents the modeling and analysis of the finger extensor mechanism. To perform a simulation of the extensor mechanism, a computational environment was created and presented in this part. Two models of the extensor mechanism with different topologies were proposed. The first model was represented by a net of individual elastic bands. This topology is suitable for performing a detailed analysis of the extensor mechanism, but oversimplifies the model anatomy. The second model was a detailed model of the extensor mechanism, which includes two layers of intercrossing fibers and represents some elements of the extensor mechanism as elastic membranes (instead of individual bands). The latter model was created in collaboration with Brain-Body Dynamics Laboratory (Los Angeles, USA).

Part 2. Separation of several sources from HD EMG-recordings

$$\mathbf{w}(\mathbf{q}) = \mathbf{J}(\mathbf{q})^{-T} \mathbf{R}(\mathbf{q}) \mathbf{E}(\mathbf{q}) \mathbf{F}(\mathbf{q}) \mathbf{a}$$

Introduction

The purpose of this part is to extract the activities of the two intercrossing muscles from a mixture of HD-sEMG signals using classification of individual potentials, which corresponds to the right part of the equation (16):

$$\mathbf{w}(\mathbf{q}) = \mathbf{J}(\mathbf{q})^{-T} \mathbf{R}(\mathbf{q}) \mathbf{E}(\mathbf{q}) \mathbf{F}(\mathbf{q}) \mathbf{a}$$

Part 2

In current work, we focused on separating the activities of little and index finger extensor muscles. Both of these fingers are controlled by two extrinsic extensor muscles. The extrinsic extensors of index finger are *extensor indicis* (EI) and a part of *extensor digitorum communis* (EDC₂); the extensors of the little finger are *extensor digiti minimi* (EDM) and a part of *extensor digitorum communis* (EDC₅). As the EI and EDM muscles overlap, they are the sources of strong mutual inference (Figure 14).

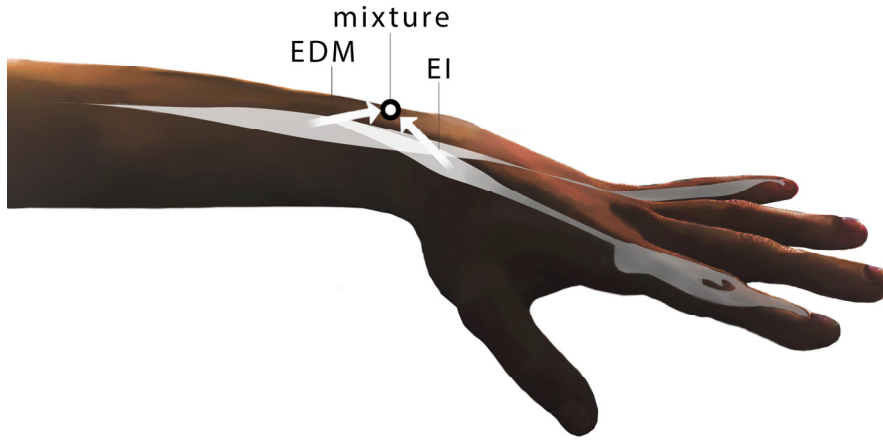


Figure 14. A schematic representation of intercrossing extensor indicis and extensor digiti minimi muscles, used in current study. Extensor digitorum muscle, also participating in extension of index and little finger is not shown.

Moreover, these fingers are known to be biomechanically independent (Zatsiorsky et al., 2000). Therefore, EI and EDM muscles represent a system with two sources, which may create a signal mixture, when activated simultaneously, or may be activated individually. This makes these two muscles an appropriate system for studying methods of muscle activation separation.

The HD EMG signals from finger extensors were recorded in LISiN laboratory (Turin, Italy). Moreover, we performed the simulation of HD EMG signals for similar conditions using the simulator,

designed by Farina and Merletti (Farina and Merletti, 2001). The simulation were performed to characterize the performance of the feature estimator and the classifier on signals with known characteristics. The signal acquisition and simulation are described in [chapter 1](#).

The proposed method of muscle activation separation consists in detecting MUAPs in HD-sEMG signals that may be the mixtures of activities of index and little finger extensors, estimating the features of the detected MUAPs and classifying each MUAP in one of two classes, according to source muscle. We firstly address the question of detection of motor unit action potentials and describe the extraction of MUAP features, which are the propagation direction and depth of originating MU (chapter 1). Next, we discuss the ability of the classifier to distinguish between two classes of MUAPs, detected during individual contraction of corresponding muscles (chapter 2, [section 2.2](#)). Finally, we address the question of classification of potentials, detected in a signal mfixture, when two muscle were active at the same time (chapter 2 [section 2.3](#)).

Chapter 1 MUAP detection and feature estimation

This chapter presents the detection of MUAPs in HD-sEMG signals and estimating their properties (features). We firstly present the methods for signal recording and simulation ([section 1.1](#)). Next, we present the algorithms for detection of MUAPs ([section 1.2](#)) and estimation of their properties, propagation direction and depth of originating MU ([section 1.3](#)). The performance of the feature estimators is shown in [section 1.4](#). Then we discuss, how the estimation performance is changed when the MUAP is overlapped by another MUAP of the same muscle with similar properties ([section 1.5](#)) or by a MUAP produced by a MU in another muscle ([section 1.6](#)). The latter case occurs when two muscles are active at the same time (signal mixture or crosstalk case)

1.1. Signal acquisition and simulation

In this study, the HD-sEMG signals recorded with 8×8 electrode matrix were used. The matrix was placed over the intersection area of *extensor indicis* (EI) and *extensor digiti minimi* (EDM) muscles to record the individual activity of these muscles as well as a mixture of signals, produced during their simultaneous activations. The similar signals were also simulated using the simulator, designed by Farina and Merletti (Farina and Merletti, 2001). This section firstly presents the experimental signal acquisition and processing and secondly describes the signal simulation.

1.1.1. Experimental signals

Ten healthy subjects (age between 24 and 30 years) participated in the experiments. Before starting the tests, subjects signed an informed consent to the procedures of the study, conducted in accordance with the Declaration of Helsinki.

Experimental setup

The HD-sEMG signals were recorded with a monopolar configuration using a 64-electrode grid (8x8 electrodes, 10 mm inter-electrode-distance, LISiN, Italy) positioned on the right forearm. Before electrode placement, the skin was shaved and slightly abraded in order to reduce electrode-skin impedance. The distal margin of the electrode array was positioned in correspondence of the proximal extremity of the ulna's head. The positioning was designed according to (Leijnse et al., 2008), and allowed acquiring the sEMG activity of extensors of little and index finger, *extensor indicis* (EI) and *extensor digiti minimi* (EDM). These muscles were identified by palpation, in order to determine the lateral portion of the forearm covered by the electrode grid. It should be noticed that extension of index and little finger is also controlled by two parts of *extensor digitorum communis*, EDC₂ and EDC₅ (see Figure 15). The applied electrode grid also covered distal portions of EDC₂ and EDC₅ muscles. The sEMG signals were recorded using a multichannel amplifier (W-EMG amplifier, Bitron Industries and LISiN – Politecnico di Torino, Torino, Italy) connected to the host computer via an Ethernet port. The gain was set to 200, the signal was sampled

at 2441 Hz and digitally converted (24 bit A/D converter). Two reference electrodes were placed on the distal portion of ulna and radius, next to the wrist joint.

The index, middle, ring and little fingers were fastened into inextensible plastic rings at distal interphalangeal joint. These rings were mounted on 3D force transducers (KISTLER 9017B) to acquire force values during the experiment. The position of the subject fingers was adjusted in a comfortable position, with the hand open in a relaxed position. The force signals were recorded as auxiliary input of the W-EMG amplifier, sampled at 2441 Hz, and shown on a computer screen as feedback to the subject.

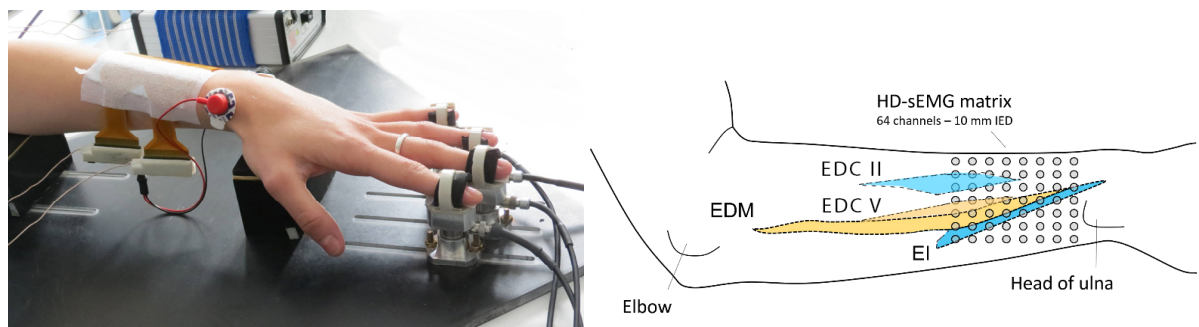


Figure 15. The 64-channel electrode grid (8x8 channels, 10 mm inter-electrode-distance, LISiN, Italy) used to record the sEMG activity from extensors of index and little finger of the right arm.

1.1.2. Simulated signals

The HD-sEMG signals were generated using a simulator, designed by Farina and Merletti (Farina and Merletti, 2001). A simulator represents a hand as multilayer cylinder. Figure 16 (based on simulator visualization) shows a skin tissue layer (blue), fat tissue layer (yellow) and muscle tissue layer (red). The bone is shown by a green cylinder in the center. The muscle is represented by a set of MUs, and each MU consists of a number of muscle fibers. Two MUs, orange and pink, are shown in the figure. Diameter of the first MU₁ and one muscle fiber are shown in an embedded image.

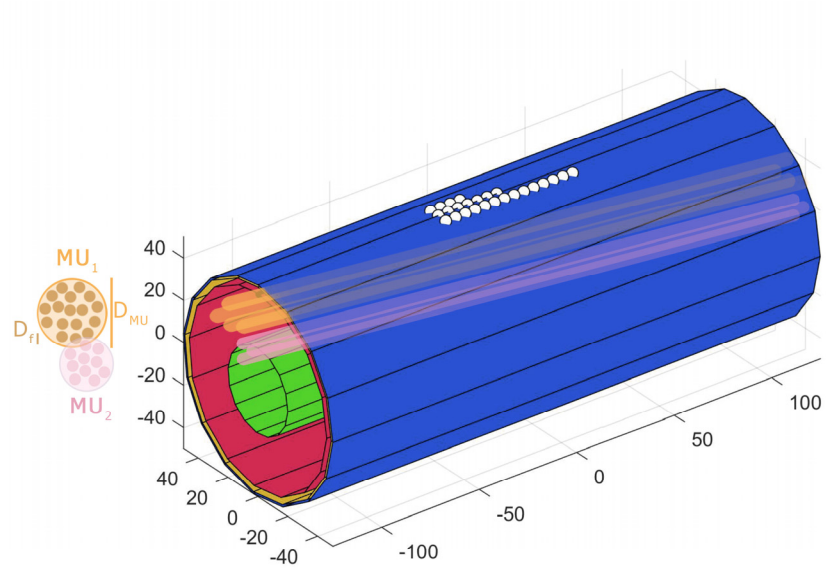


Figure 16. A model of the hand used in the simulator (Farina and Merletti, 2001). Blue, yellow and red layers corresponds to skin, fat and muscle tissue correspondingly. Green cylinder in the center corresponds to the bone. Two MUs, orange and pink, are shown.

All MUs were considered to be parallel in one muscle, and each MUs was modeled as a set of parallel fibers.

1.2. MUAPs detection

1.2.1. Time localization of MUAP

The MUAPs were detected in each channel individually, based on a technique, proposed by Farina et al. (Farina et al., 2000). The discretized continuous wavelet transform (CWT) was performed to transform each signal into a CWT coefficient time-scale space using a Mexican hat (MHAT) wavelet, which was shown to fit well the MUAP shape in case of monopolar EMG recordings (Laterza and Olmo, 1997). MHAT wavelet is a second order derivate of a Gaussian function:

$$\psi(t) = k \left(1 - t^2\right) e^{-\frac{t^2}{2}}, \quad (20)$$

Figure 17 shows a MHAT wavelet waveform.

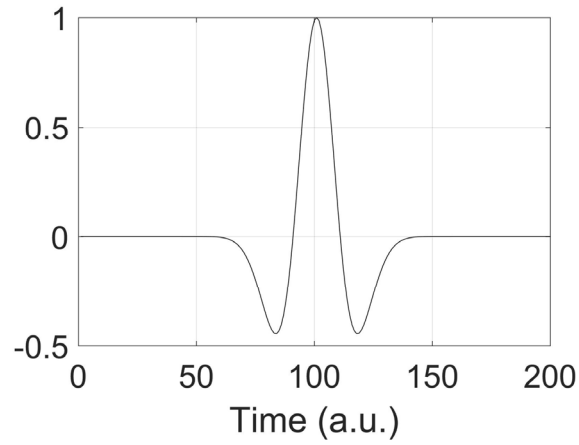


Figure 17. A MHAT wavelet waveform

CWT coefficients EMG signal (time window 0,4 s) are shown in Figure 18a.

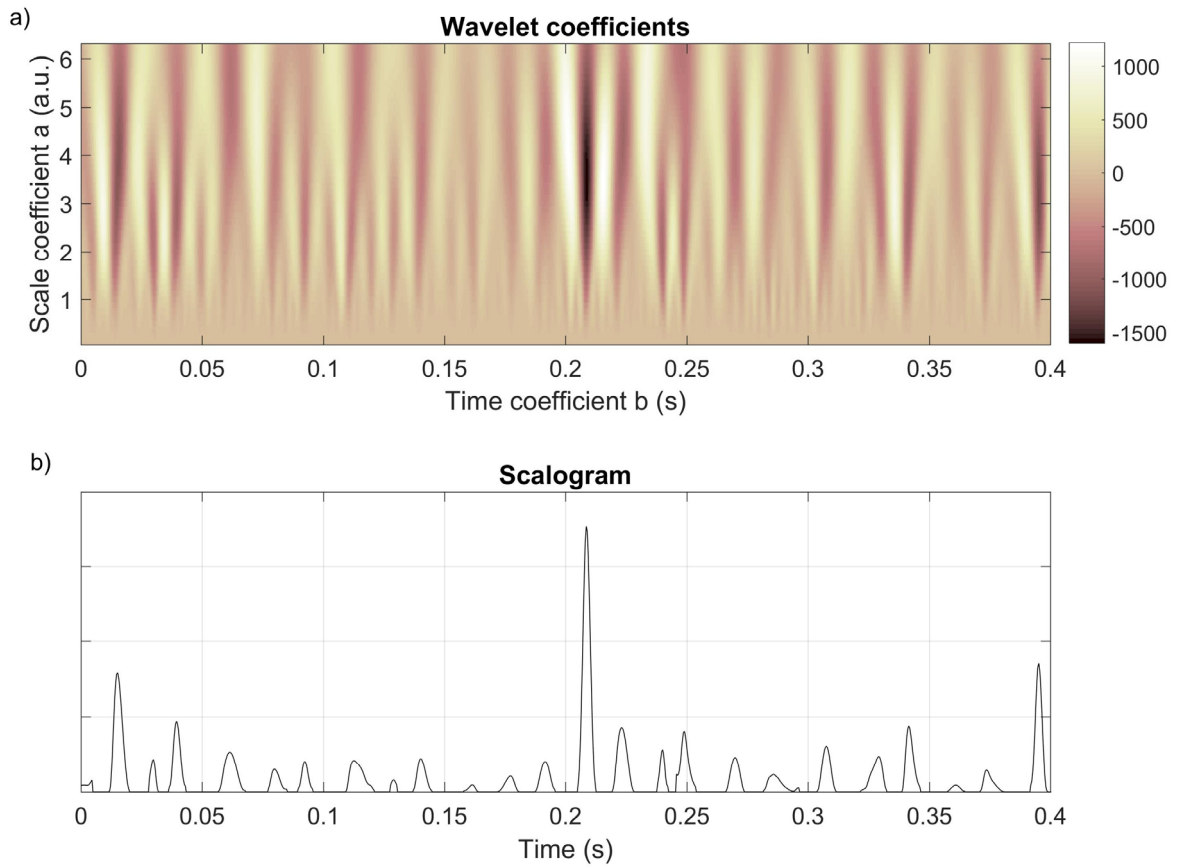


Figure 18. a) The wavelet transform of EMG signals b) The scalogram, calculated as an integral of the wavelet transform over the scale dimension

Next, the CWT coefficient space were integrated over the scale dimension to calculate the scalogram for the values of the scale coefficient a from 0.125 to 6.250. The scalogram's maxima corresponding to MUAP negative phase were found and considered as time locations of MUAPs.

1.2.2. MUAP selection

To avoid redundancy for each detected MUAP we verified if the originating motor unit (MU) was located closer to the current electrode than the electrodes, adjacent to the current one (Figure 19a). The MU was considered closer to current electrode than the adjacent ones if the potential at the current electrode at the moment when MUAP was detected was higher than the potential on adjacent electrodes.

1.3. Feature extraction

Below we present the methods used for MUAP feature estimation, which were propagation direction as well as originating MU depth.

1.3.1. MUAP propagation direction estimation

Under the assumption that MUAPs propagate parallel to the electrode plane, the delay between the observance of a MUAP in current electrode and its k -th neighbor depends on the MUAP propagation angle α (see Figure 19b):

$$\tau_k = \frac{l_k \cdot \cos(\alpha - \alpha_k)}{v} + \varepsilon, \quad (21)$$

where v is a MUAP propagation speed, l_k is a distance between the current electrode and its k -th neighbor, α_k is a direction from the current electrode to its k -th neighbor, ε – error.

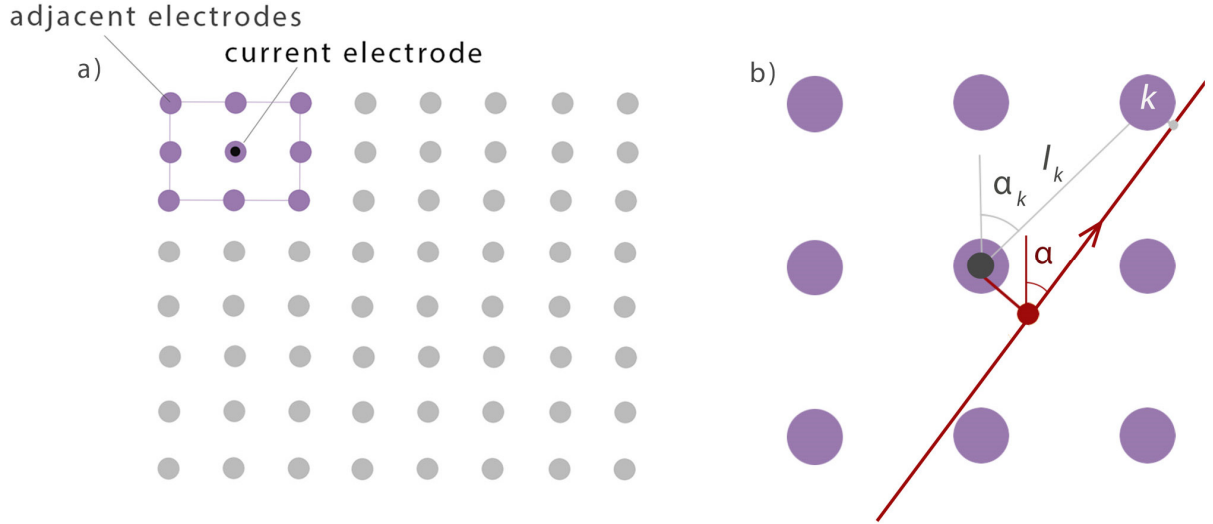


Figure 19. a) The electrode grid. An electrode with its adjacent electrodes is shown; b) the schema of MUAP propagation direction estimation. The MUAP, shown by a red circle, propagates in the direction α

This equation can be rewritten as

$$\tau_k = \frac{\cos \alpha}{v} \cdot l_k \cdot \cos(\alpha_k) + \frac{\sin \alpha}{v} \cdot l_k \cdot \sin(\alpha_k) + \varepsilon. \quad (22)$$

For simplicity, we will introduce a vector \mathbf{u} , which contains the information about the MUAP propagation direction and speed.

$$\mathbf{u} = \begin{bmatrix} \frac{\cos \alpha}{v} & \frac{\sin \alpha}{v} \end{bmatrix}^T. \quad (23)$$

The components of this vector will be denoted as u_1 and u_2 . Hence, the sum of the squared residuals may be written as:

$$e = \sum_{k=2}^K (\tau_k - u_1 \cdot l_k \cdot \cos(\alpha_k) - u_2 \cdot l_k \cdot \sin(\alpha_k))^2, \quad (24)$$

The least squares estimation of the components of \mathbf{u} may be found by solving an equation system, minimizing e :

$$\begin{cases} \frac{\partial}{\partial u_1} \sum_{k=2}^K (\tau_k - u_1 \cdot l_k \cdot \cos(\alpha_k) - u_2 \cdot l_k \cdot \sin(\alpha_k))^2 = 0 \\ \frac{\partial}{\partial u_2} \sum_{k=2}^K (\tau_k - u_1 \cdot l_k \cdot \cos(\alpha_k) - u_2 \cdot l_k \cdot \sin(\alpha_k))^2 = 0 \end{cases}, \quad (25)$$

After calculating the derivatives, the system becomes

$$\begin{cases} \sum_{k=2}^K u_1 \cdot l_k^2 \cdot \cos(\alpha_k)^2 + \sum_{k=2}^K u_2 \cdot l_k^2 \cdot \cos(\alpha_k) \cdot \sin(\alpha_k) = \sum_{k=2}^K \tau_k \cdot l_k \cdot \cos(\alpha_k) \\ \sum_{k=2}^K u_1 \cdot l_k^2 \cdot \cos(\alpha_k) \cdot \sin(\alpha_k) + \sum_{k=2}^K u_2 \cdot l_k^2 \cdot \sin(\alpha_k)^2 = \sum_{k=2}^K \tau_k \cdot l_k \cdot \sin(\alpha_k) \end{cases}, \quad (26)$$

or under a matrix notation,

$$\mathbf{K} \times \mathbf{u} = \mathbf{T}, \quad (27)$$

where

$$\mathbf{K} = \begin{bmatrix} \sum_{k=2}^K l_k^2 (\cos \alpha_k)^2 & \sum_{k=2}^K l_k^2 \cos \alpha_k \sin \alpha_k \\ \sum_{k=2}^K l_k^2 \cos \alpha_k \sin \alpha_k & \sum_{k=2}^K l_k^2 (\sin \alpha_k)^2 \end{bmatrix}, \quad \mathbf{T} = \begin{bmatrix} \sum_{k=2}^K \tau_k l_k \cos \alpha_k \\ \sum_{k=2}^K \tau_k l_k \sin \alpha_k \end{bmatrix}. \quad (28)$$

Given the delay observations from all adjacent electrodes $k = 2 \dots K$, the least squares estimation of \mathbf{u} is:

$$\hat{\mathbf{u}} = \mathbf{K}^{-1} \times \mathbf{T}, \quad (29)$$

where the components of the $\hat{\mathbf{u}}$ vector will be denoted as \hat{u}_1 and \hat{u}_2 .

Once $\hat{\mathbf{u}}$ is calculated, the estimation of propagation direction was found as:

$$\begin{cases} \hat{\alpha} = \arctan\left(\frac{\hat{u}_2}{\hat{u}_1}\right) & \text{if } \hat{u}_1 \geq 0 \\ \hat{\alpha} = -\pi + \arctan\left(\frac{\hat{u}_2}{\hat{u}_1}\right) & \text{if } \hat{u}_1 < 0 \end{cases} \quad (30)$$

As it was shown above, the estimation of propagation direction depends on inter-electrode delay τ_k estimation, which is described below. For each instant t_i , at which a MUAP was detected, we selected a $n = 5$ ms signal window around t_i . This window was used as a template, containing the MUAP. The adjacent channels contain the images of the MUAP, which may be shifted in time due to activation propagation. We supposed, that the signal in adjacent channel contain the template if cross-correlation between it and the template has a maximum higher than 0.7 in the $m = 11$ ms window around t_i . The value of n and m was chosen based on mean MUAP duration and propagation velocity.

The delay τ_k between the current channel and adjacent channel k were calculated as a sum of two components: a main component of delay δ , which is bigger than one sample and a minor component $\Delta\delta$, which is smaller than one sample. For a given sampling frequency of HD-sEMG signals, the sampling period $\tau_s \approx 0.4$ ms. Therefore,

$$\tau_k = \delta + \Delta\delta. \quad (31)$$

Firstly, the main delay component δ was calculated accurate within one sample using maximum of cross-correlation between the current and adjacent channel. Figure 20a shows the initial MUAPs from the current channel and the delayed MUAP from the adjacent one; the delay between the signals is clearly seen. Figure 20b shows the cross-correlation function between the channels. The maximum of the cross-correlation lies at 6 samples ($\delta = 2.46$ ms). Figure 20c shows the initial signals with main component of the delay δ compensated. Secondly, when the main delay component was compensated, the minor part of the delay $\Delta\delta$, which is less than one sample, was calculated as slope of the unwrapped MUAP phase shift between the MUAP from the current channel and the MUAP from adjacent channel shifted by δ . The slope of the phase shift was calculated for the frequencies $[20; 200]$ Hz which are the lower frequencies of MUAP spectrum (Figure 20d). Figure 20e shows the MUAP after compensation of both main and minor components of the delay.

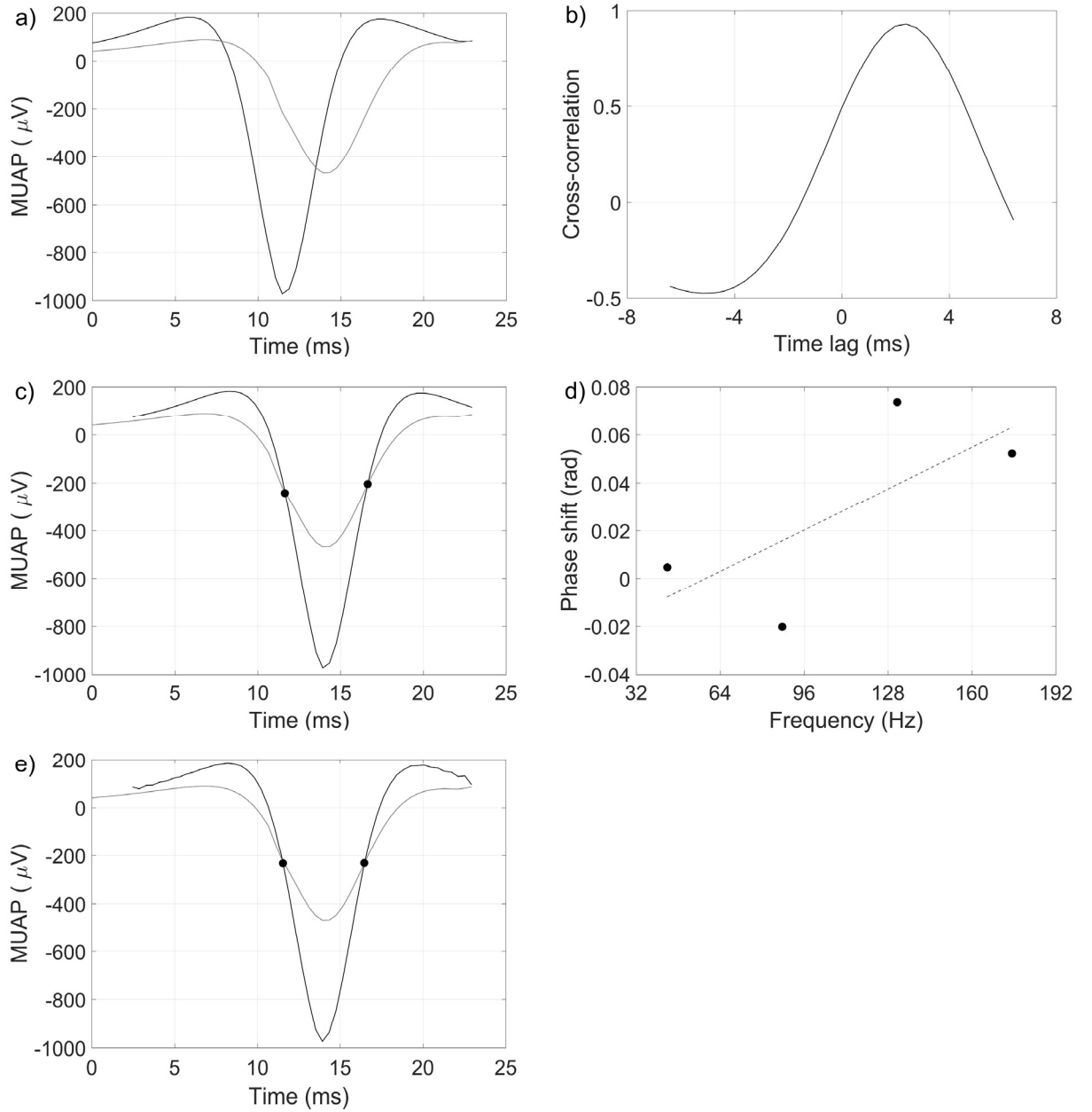


Figure 20. The scheme of the delay estimation. a) A MUAP from the current channel and an adjacent one. The delay between the signals is clearly seen. b) A cross-correlation signal between these two signals. c) The initial signals with the delay, compensated up to a whole number of samples. However, a phase-shift, which is less than one sample, still exists. d) A phase shift between the signals in the image (c) as a function of frequency. e) The signals with the compensated delay, estimated from the phase shift

The above-described procedure was used to estimate the propagation direction for each detected MUAP in each channel individually. Based on these estimations, the mean value and standard deviation of the propagation angle among all detected MUAP in one channel can be calculated. The distribution of the mean values and standard deviations of the propagation angles among all the channels of the electrode grid may be represented as a “quiver” plot. An example of such plot is shown in Figure 21. This plot represents the propagation direction map calculated from the signals of index finger activity of one representative subject #4. The propagation maps calculated from the acquired signals from all subjects during the activity of index, little and simultaneous activity of both fingers may be found in the annex. Orientation of each

arrow shows the mean propagation direction of the MUAPs detected in corresponding electrode. The fine lines around each arrow give information about standard deviation of the propagation direction. The length of each arrow correspond to a number of MUAPs, detected in corresponding channel.

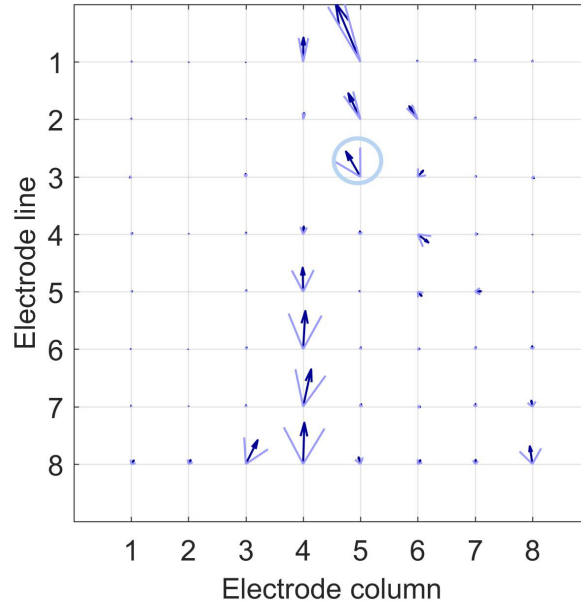


Figure 21. The propagation direction map calculated from the signals of index finger activity of the subject #4

1.3.2. MU depth estimation

The second estimated feature of a MUAP was the depth of an originating MU. The proposed MU depth estimator was based on a source localization algorithm (Kay, 1993; Lee, 1975). The proposed estimator uses the relationship between the measured value of a MUAP and the distance between the originating MU and electrode. For two points over the skin a and b , the measured potentials are related with distances by following relationship, reported by Monster and Chan (Monster and Chan, 1980):

$$\frac{U_a}{U_b} = \left(\frac{d_b}{d_a} \right)^p, \quad (32)$$

They have also shown that the power p lies between 0.5 ... 1.2. In the current study we assumed $p = 1$.

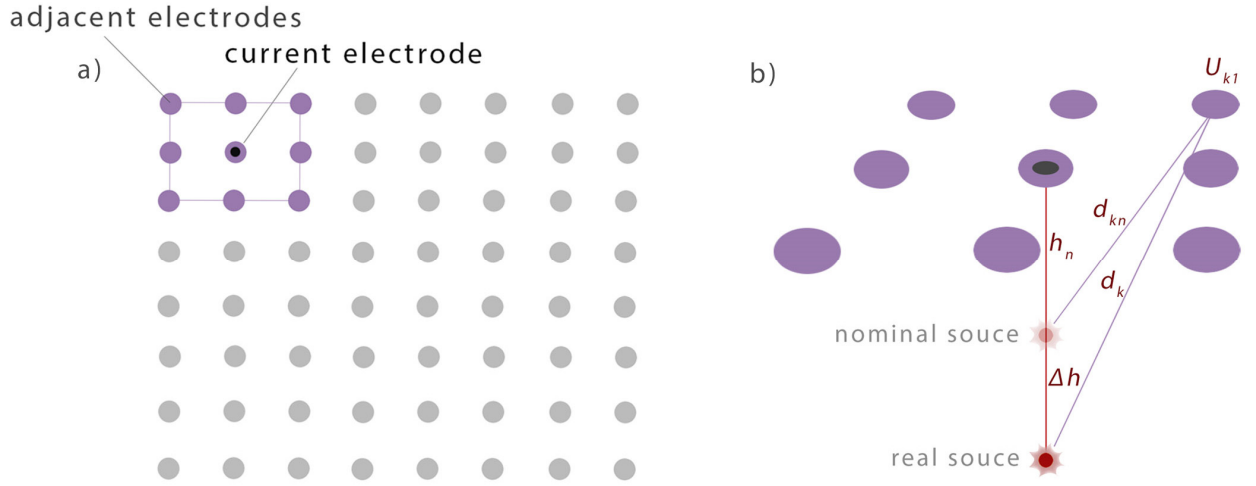


Figure 22. a) The electrode grid. An electrode with its adjacent electrodes are shown; b) the schema of originating MU depth estimation. The real source is considered located under the current electrode near a some nominal source with known location. The depth of the nominal source h_n and distances from the nominal source to k -th adjacent electrode d_{kn} are known. The difference between the depth of the real and nominal source is Δh

The depth estimator uses the distribution of the measured potentials over $K-1$ electrodes, adjacent to the current one at the time, when the MUAP were detected by the current electrode. Potential values, measured by the current electrode and its adjacent, depend on the depth of the MU as well as the intensity of the MUAP. To keep only information about the depth, the potentials measured by $K-1$ neighbors of the current electrode were normalized by the potential at the current electrode:

$$U_{k1} = \frac{U_k}{U_1}. \quad (33)$$

We assumed that the MU lies under the current electrode in the vertical line, passing through the center of the current electrode. Therefore, the distances between the MU and the electrodes depend only on MU depth. This assumption became possible due to MUAP selection step, in which only the potentials, close to current electrode were kept.

We also assumed that the MU originating the observed potentials (real source) is lying near some nominal source, which is located at the same line as the real source at the depth h_n (Figure 22b). The localization of the nominal source was considered to be known and was predefined as a starting point of the algorithm. The difference between the depth of the nominal and real source is denoted Δh , which is possible, if the real source is deeper, than the nominal one, and negative, if the nominal source is more superficial than the nominal.

The distance between the nominal source and k -th electrode was denoted as d_{kn} . Given the distance between the nominal source and k -th electrode and the difference between the depth of the nominal and real source, the distances between the k -th electrode and a real source may be found from the triangle ACB (Figure 23).

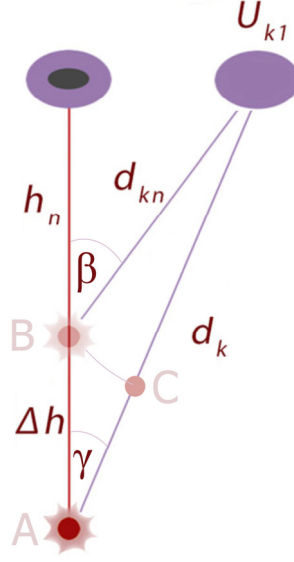


Figure 23. The schematic representation of the nominal source (B) and real source (A).

Under the assumption that the nominal source is close to the real one, ACB may be considered to be the right angle. Moreover, the angles γ and β may be considered to be similar. Therefore, the distance from the real source to k -th electrode may be represented as:

$$d_k \approx d_{kn} + \Delta h \cdot \sin(\gamma) \approx d_{kn} + \Delta h \cdot \sin(\beta). \quad (34)$$

The angle β may be found from the depth of the nominal source and the distance from the nominal source to the k -th electrode, which are both predefined:

$$d_k \approx d_{kn} + \frac{h_n}{d_{kn}} \Delta h = \frac{d_{kn}^2 + \Delta h \cdot h_n}{d_{kn}}, \quad (35)$$

Hence, using (32) – (35) we expressed the normalized potential at the k -th neighbor of the current electrode as a function of Δh :

$$U_{k1} = \frac{d_{kn}(\Delta h + h_n)}{d_{kn}^2 + \Delta h \cdot h_n} + \varepsilon, \quad (36)$$

where ε is an error.

Hence, the sum of the squared residuals may be written as:

$$e = \sum_{k=2}^K \left(\frac{d_{kn}(\Delta h + h_n)}{d_{kn}^2 + \Delta h \cdot h_n} - U_{k1} \right)^2 \quad (37)$$

The least squares estimation of the distance between the nominal and real source $\hat{\Delta h}$ may be solving the equation, minimizing e :

$$\frac{\partial}{\partial(\Delta h)} \sum_{k=2}^K \left(\frac{d_{kn}(\Delta h + h_n)}{d_{kn}^2 + \Delta h \cdot h_n} - U_{k1} \right)^2 = 0. \quad (38)$$

After calculating the derivative, the equation becomes

$$\sum_{k=2}^K \frac{d_{kn}(\Delta h + h_n) - U_{k1}(d_{kn}^2 + \Delta h \cdot h_n)}{d_{kn}^2 + \Delta h \cdot h_n} \cdot \frac{d_{kn}(d_{kn}^2 + \Delta h \cdot h_n) - h_n d_{kn}(\Delta h + h_n)}{(d_{kn}^2 + \Delta h \cdot h_n)^2} = 0. \quad (39)$$

Finally, the LS-estimation of the difference between the nominal and real source $\hat{\Delta h}$ is

$$\hat{\Delta h} = \frac{\sum_{k=2}^K d_{kn}^2 U_{k1} - \sum_{k=2}^K d_{kn} h_n}{\sum_{k=2}^K d_{kn} - \sum_{k=2}^K U_{k1} h_n}, \quad (40)$$

This difference between the depth of the nominal and real source was estimated under the assumption that the real source is located close to the nominal source. Owing that the depth of the nominal source was chosen without any prior knowledge about the real source location, (40) was iteratively repeated. At each new iteration the estimated depth of the source was taken as a nominal source depth and the following loop was repeated until convergence:

$$\left\{ \begin{array}{l} \text{while } \hat{\Delta h} > eps \\ \hat{\Delta h} \leftarrow LS \\ h_n^{(m+1)} = \hat{\Delta h} + h_n^{(m)} \\ \hat{h} = h_n \end{array} \right. \quad (41)$$

Hence, \hat{h} obtained in (41) is the estimation of depth of the real source.

Similarly to the propagation direction estimation, the depth of originating MU was estimated for each detected MUAP in each channel individually. These estimations can be used to show the distribution of the originating MUs among the volume conductor. An example of such distribution is shown in Figure 24 (subject #4, index finger activity). The color represents the relative number of MUAPs detected in each voxel. It was calculated as a number of MUAPs detected in each voxel divided by the maximal number of MUAPs detected among all voxels.

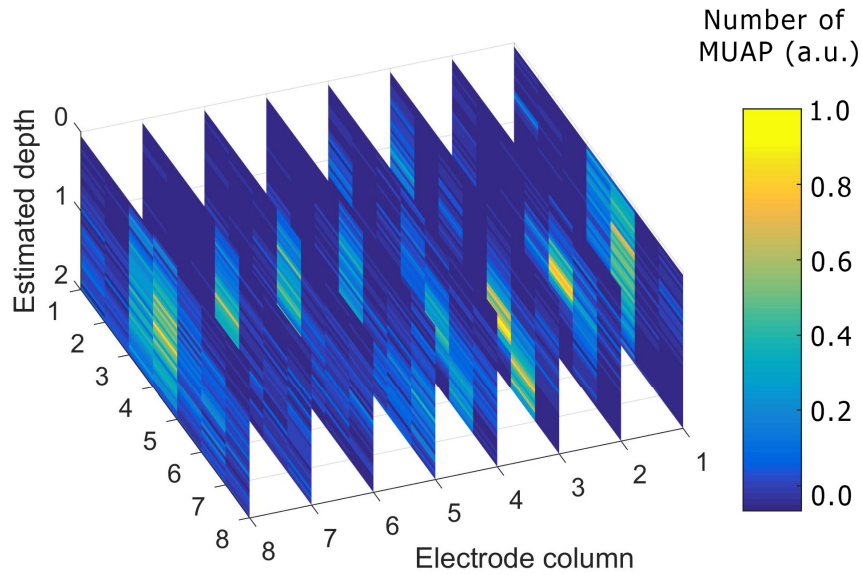


Figure 24. The MU depth distribution calculated from the signals of index finger activity of the subject #4

1.4. Performance of the estimation

In this section, we present the performance of the feature estimation of the individual MUAP, not overlapped by any other MUAPs. To calculate the estimator performance, the individual MUAPs were simulated with predefined parameters (direction and depth). The influence of the noise on estimation performance was also analyzed.

1.4.1. Direction estimation

Noiseless case

Firstly, a single MU with 20 fibers was simulated with propagation directions from -90° to 90° and a step of 1° . In each direction, one MUAP produced by the MU was simulated. No noise was added to simulated MUAP to study the estimation performance in noiseless conditions. For each MU direction, a MUAP was detected and its propagation direction was estimated. The propagation angles, was compared with the real angle, used in simulator. Figure 25a traces the estimated angle as a function of the real one. For ideal estimator, the estimated angle is equal to real; therefore, this relationship becomes a straight line. Deviations from the strait line correspond to estimation error in noiseless case. The error between the estimated and real angle is shown in Figure 25b. It can be seen from this figure that error is minimal when the MU direction is equal to $\frac{\pi}{2} \cdot n, n \in \mathbb{Z}$.

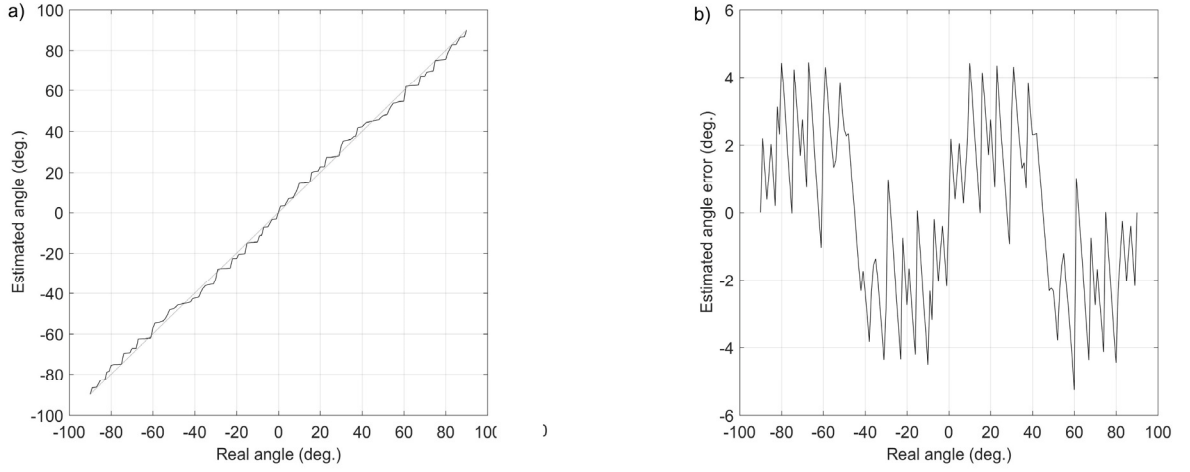


Figure 25. a) The estimated angle as a function of the defined angle; b) the error between the estimated and defined angle.

The form of the error plot is close to sinusoid with a period of $\frac{\pi}{2}$ which may be explained by the relationship between the error of the delay estimation and the angle. Figure 26a shows a MUAP in current channel and a delayed MUAP recorded by adjacent electrode. Figure 26b shows the cross-correlation function between the MUAP in the current channel and a delayed MUAP in adjacent channel, estimated in a short window (11 ms, shown in gray in Figure 26a) and a full window (105 ms). The error between two cross-correlation functions is clearly seen.

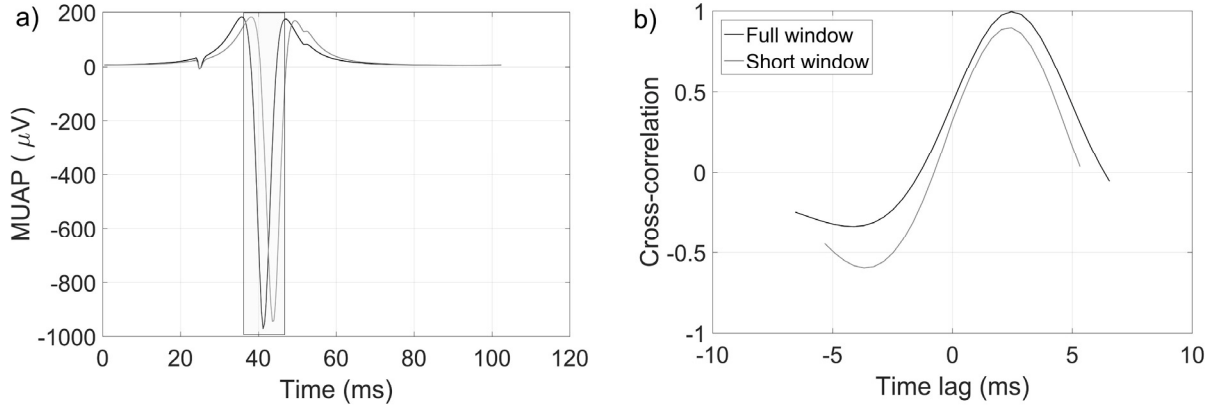


Figure 26. a) A MUAP in current channel and a delayed MUAP recorded by adjacent electrode. b) The cross-correlation function estimated for full-window (105 ms) and a short window (18 ms, shown in gray in image (a)).

To estimate a MUAP propagation direction a short signal window is used, which may result in bias. More the delay between the MUAP from the current and the adjacent electrode is, closer to the boundary the MUAP from the adjacent electrode is, and, consequently, more is the delay estimation error.

Noisy case

To study the direction estimation performance in noisy MUAPs, white Gaussian noise with different mean power was added to MUAPs, simulated with propagation directions from -90° to 90° . Thirty

realizations of the Gaussian noise were added to each simulation at three levels of noise power (signal-to-noise ratio SNR=20 dB, 6 dB and 0 dB). The mean error and standard deviation of the estimated propagation angle were calculated among all 30 noisy simulations for each propagation angle and noise power (Figure 27).

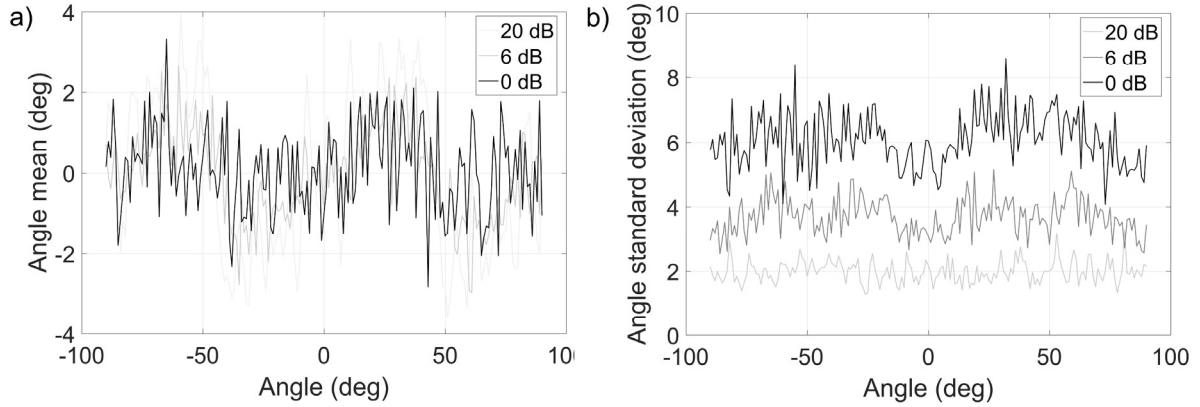


Figure 27. The standard deviation of the estimated angle as a function of propagation angle for signal-to-noise ratio equal to 20 dB, 6 dB, 0 dB

It is seen from the figure Figure 27a that the mean error between the estimated and defined angle has the similar form as in the noiseless case (Figure 25b) and does not significantly change with the noise power. Figure 27b shows how the standard deviation of the estimated angle increases with noise power. It can be also noticed, that the standard deviation form is close to the form of the mean error absolute value (Figure 27a) with minimal values at $\frac{\pi}{4} \cdot n, n \in \mathbb{Z}$.

1.4.2. Depth estimation

Noiseless case

To study the single MU was simulated with different depths, from 3 mm to 9 mm and 0.1 mm step. The propagation angle was set to 0° for all simulations. Figure 28 shows the estimated depth as a function of the real depth, used in simulation.

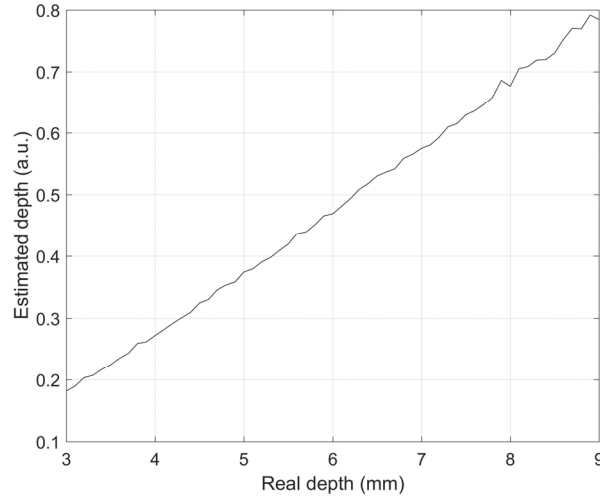


Figure 28. The estimated depth as a function of the simulated depth.

It is seen from the figure; that the relationship between the predefined and estimated depth of MU is linear. The estimated depth values are given in arbitrary units, because estimation of the MU depth in millimeters requires information about tissue conductivity, which may be different among the subjects and which may be difficult to obtain. However, the purpose of this study is to use the information about the MU depth to distinguish the signals from different muscles, therefore, the relative depth values are sufficient for this purpose.

Noisy case

Similarly with the study of the propagation direction estimation, Gaussian noise with different mean power was added to simulated MUAPs to compute the influence of noise on standard deviation of the estimated MU depth. Thirty realizations of the Gaussian noise were added to each simulation at three levels of noise power (SNR=20 dB, 6 dB and 0 dB). The standard deviation of the estimation was calculated among all 30 noisy MUAP simulation at given depth and noise power (Figure 29).

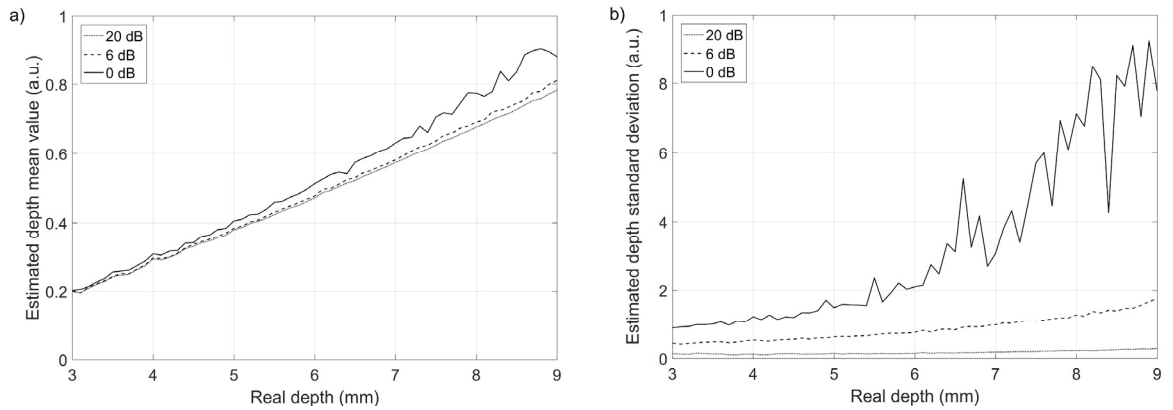


Figure 29. The standard deviation of the estimated MU depth as a function of defined depth for signal-to-noise ratio equal to 20 dB, 6 dB, 0 dB

It can be seen from the Figure 29a that increase of the noise power influence the depth estimation, especially for deep MUAPs. From the Figure 29b one can notice that the standard deviation of depth estimation increases when SNR decreases. It may be also noticed that the standard deviation of the depth estimation increases with the defined depth. It can be explained by the fact that MUAPs become more spread with originating MU depth.

In this section, the performance of the estimators of both features, used for MUAP classification (propagation direction and depth) was studied. We compared the performance of the estimator in noiseless MUAP simulations as well as in simulations with added white Gaussian noise. It was shown that the performance of both estimators depends on real value of the estimated parameter. The estimation variance is higher for the MUAPs from the deeper MUs. The next section shows how the estimation performance changes if MUAP is overlapped by another MUAP from another MU of the same muscle, i.e. having the similar properties.

1.5. Overlapping of MUAPs from the different MU of the same muscle

It was shown in previous section, that the depth and direction of one individual (not overlapped) MUAP can be estimated with high degree of precision. However, this case is only possible at small activation level. During voluntary contractions of one muscle, active at moderate and high force level, MUAPs of one MU are usually overlapped by MUAPs produced by other active MUs of the same muscle.

We will firstly analyze, what is a probability of a MUAP to be overlapped by MUAPs from the other MUs at different force levels.

1.5.1. Theoretical ground

Below MUAP will be modeled as a rectangular impulse with duration τ for simplicity. We assume that this MUAP occurs at time $t = 0$ s. We will consider that this MUAP is overlapped by a MUAP from another MU, if the latter occurs in $(-\tau; \tau)$ s (Figure 30). We define the occurrence instance of the MUAP from the second MU as $T + dT$ s, where T depends on a firing period of the second MU and a dT is a random variable, corresponding to physiological variability of the firing rate of the second MU. Under the assumption, that there is no synchronization between the firing of the first and the second MU, we can assume that T is distributed with the uniform law:

$$T \sim \mathcal{U}(-0.5T_f, 0.5T_f), \quad (42)$$

where T_f is a firing period of the second MU.

In other words, if the first MUAP occurs at the moment $t = 0$, the MUAP from the second MU will certainly occur in an interval of time $(-0.5T_f, 0.5T_f)$ given the firing period of the second MU T_f and

in absence of random component dT . The random component of the firing period dT can be modeled using the Gaussian law:

$$dT \sim \mathcal{N}(0, \sigma_n). \quad (43)$$

Hence, the probability distribution function PDF of the occurrence time of the MUAP from the second MU can be found as a convolution between the PDFs of T and dT :

$$p(t) = -\frac{1}{2T_f} \left(\operatorname{erf} \left(\frac{t - 0.5T_f}{\sigma_n \sqrt{2}} \right) - \operatorname{erf} \left(\frac{t + 0.5T_f}{\sigma_n \sqrt{2}} \right) \right). \quad (44)$$

Figure 30 shows a model of a MUAP and a PDF of the occurrence time of the MUAP from the second MU.

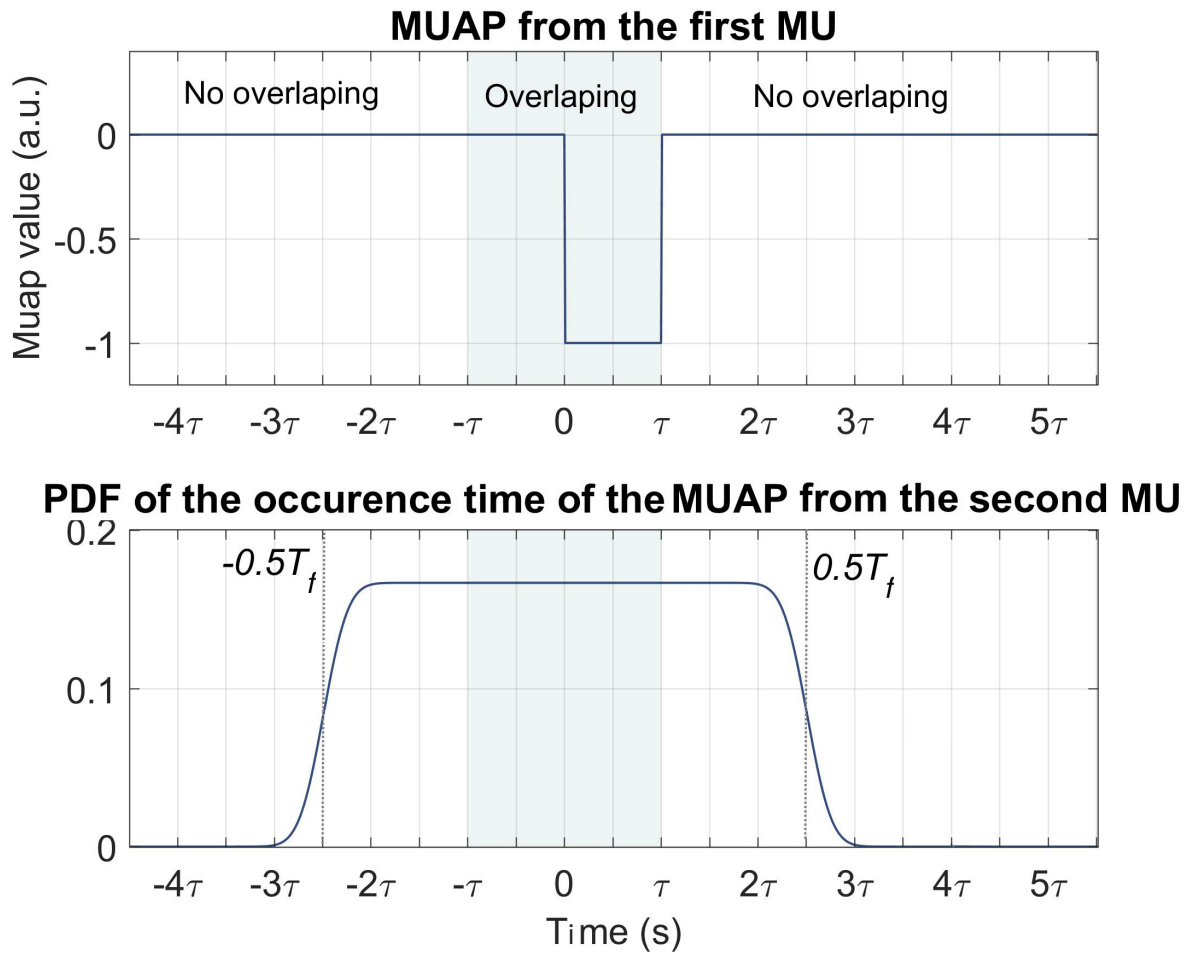


Figure 30. The PDF of occurrence time of the MUAP from the second MU in a muscle with two active MUs. Time $t=0$ corresponds to occurrence of the first MUAP. If the second MUAP occurs in time interval, shown in blue, the MUAPs will be overlapped.

The MUAP from the first MU will be overlapped by a MUAP from the second MU from the same muscle if it occurs in a time interval $(-\tau, \tau)$, highlighted by blue in Figure 30. Hence, the probability of the overlapping of the first MUAP by the second one is

$$P = \int_{-\tau}^{\tau} p(t)dt . \quad (45)$$

For example, for $\tau = 5$ ms, $T_{max} = 50$ ms, and $\sigma_n = 10$ ms the probability of overlapping of the MUAP by a MUAP from the second MU is $P = 0.12$.

In real muscle, the firing period of the second MU T_f depends on muscle activation level, hence, the higher the muscle activation level is, the higher is the overlapping probability.

Moreover, when the force continues increasing, more MUs become involved in contraction. To take this into account we will suppose that there are $N+1$ active MUs in muscle, the current one and N others.

The first MUAP of the muscle will not be overlapped only if it is not overlapped by a MUAP from any other N MUs. Hence, using the binominal law, the probability $P_m(N, m)$ that the current MUAP is overlapped by m MUAPs from the same muscle with N other active MUs may be calculated as:

$$P_m(N, m) = \frac{N!}{m!(N-m)!} P^m (1-P)^{N-m}, \quad (46)$$

Figure 31 shows the overlapping probability $P_m(N, m)$ for $m=0$ overlapping and $m=1, 3, 5, 7$ overlappings for different N .

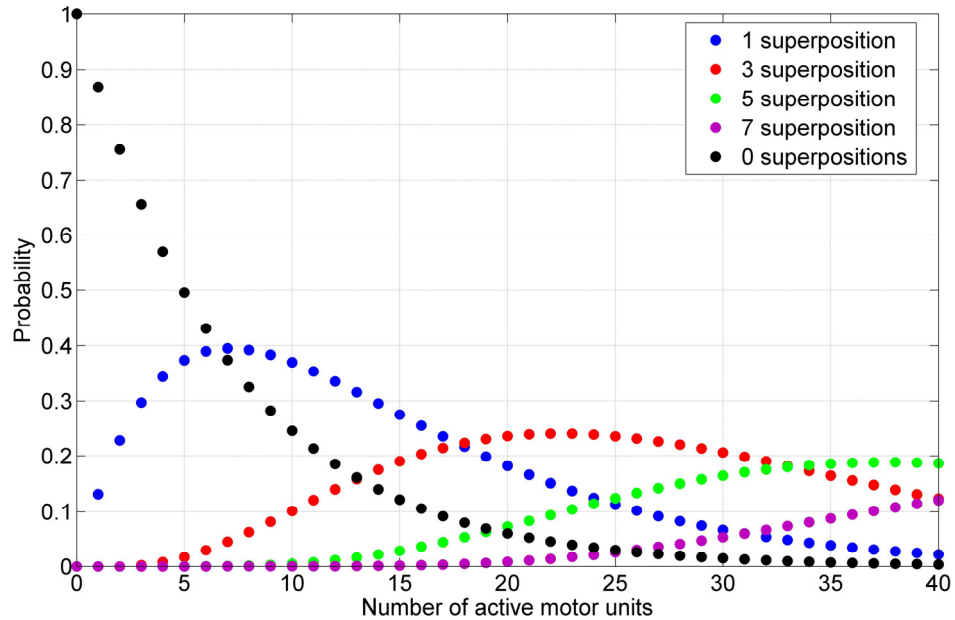


Figure 31. The probability of MUAP to be overlapped by another MUAP of the same muscle as a function of a number of active MUs in muscle.

The black points show the probability that the detected potential is a pure MUAP, produced by only one MU and not overlapped by MUAPs from other MUs. For the same time parameters, as in previous

example ($\tau = 5$ ms; $T_{max} = 50$ ms, and $\sigma_n = 10$ ms) and five active MUs in muscle $N = 5$, the probability that a MUAP will not be overlapped by any other MUAP from the same muscle is 0.53. Hence, a MUAP has almost the same probability to be or not to be overlapped by any MUAP from different MU of the same muscle.

This illustration is a simplified model, which may be used only as a rough estimate of the probability of a MUAP to not be overlapped or to be overlapped by other MUAPs from the same muscle.

Below we present the performance of the feature estimators in case when the MUAP of one MU is overlapped by MUAPs from other active MUs of the same muscle. We will analyze how the overlapping change the feature estimation. We will assume that the MUs in the same muscle has the similar properties (depth and direction).

1.5.2. Direction estimation

This subsection reports how overlapping of MUAPs from different MUs of the same muscle change the estimated direction.

To study this effect, we simulated a muscle by a set of MU with parallel fibers. The fibers were grouped in 32 MUs and the orientation of all fibers was 30° . All MUAPs were concentric to eliminate the influence of the depth. We simulated 20 s of HDs-EMG signal with different number of recruited MUs (1, 2, 4, 8, 16, 32). The MUAPs were detected in signals and their propagation direction was estimated. We studied how the propagation direction, estimated by the central electrode of the matrix, changes with recruitment of MUs. Figure 32 shows mean error (a) and standard deviation (b) of the estimated direction

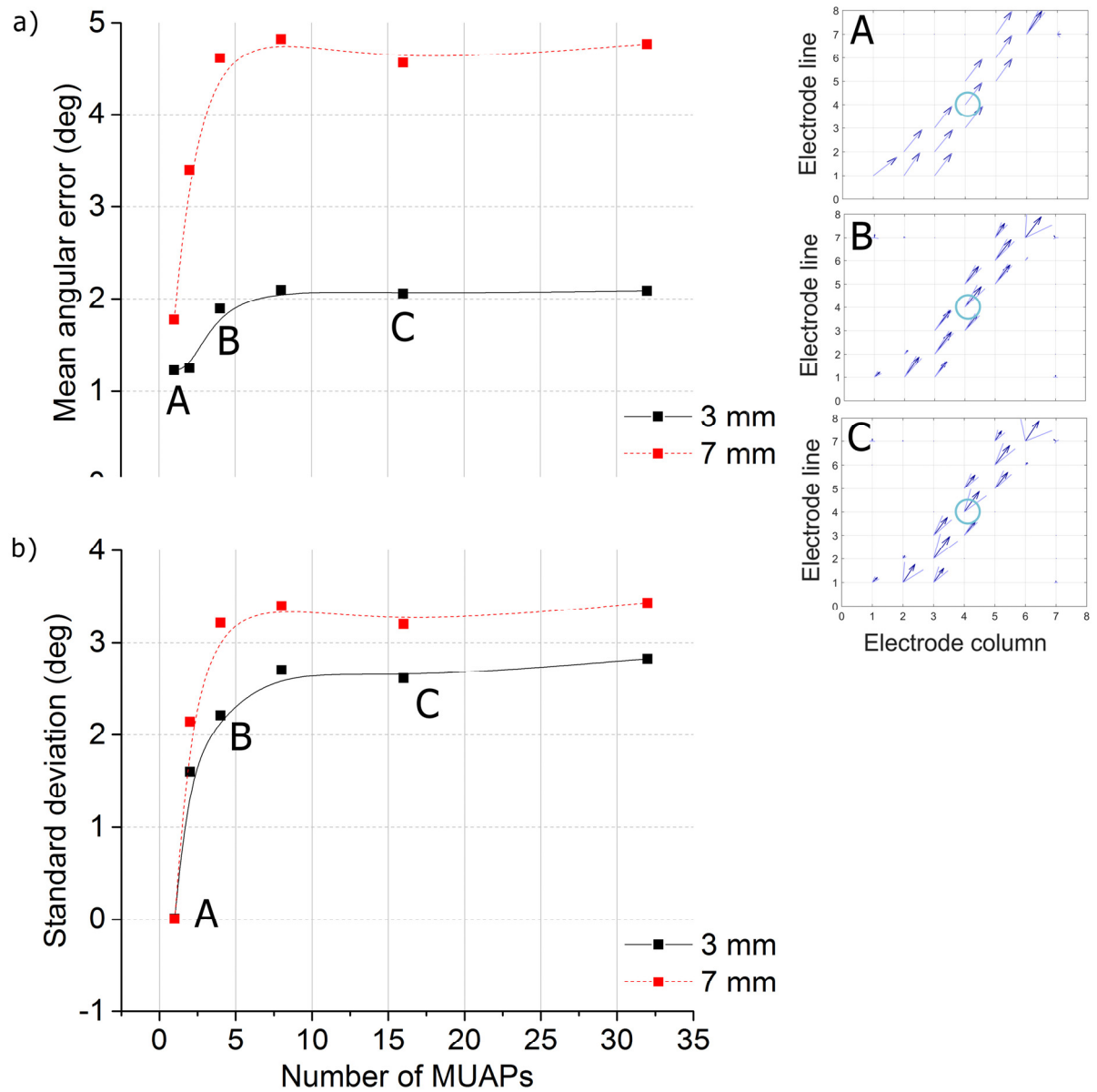


Figure 32. The influence of the number of MUAPs on mean error (a) and standard deviation (b) of direction estimation. The propagation maps are shown for 1, 4 and 16 MUs (A, B, C).

Images A, B, and C at the right side of the figure show the propagation direction maps in case when 1, 4 and 16 MUs were recruited. The maps show mean propagation direction and its standard deviation for each electrode. The electrode, used to calculate the mean error and standard deviation of estimated propagation direction is shown by a blue circle. Two curves for mean error and standard deviation are plotted: a black solid line corresponds to a muscle located at the depth of 3 mm, and a red dashed line corresponds to a muscle located at the depth of 7 mm. Each point represents a mean error or standard deviation of the propagation direction calculated over all detected peaks in the central electrode. The number of detected peaks for different muscle depth and number of active MUs is shown in Table 2.

Table 2. A number of MUAPs, detected in central channel from 20s HD-sEMG signal simulations for different number of active MUs and muscle depth

Muscle depth (mm)	Number of peaks detected in the central electrode					
3	196	693	1035	1081	1074	1074
7	197	659	906	854	874	865
	Number of active MUs					
	1	2	4	8	16	32

It can be seen from the figure that when the number of MUs increases, the mean error and the standard deviation of estimated direction increase as well. As is may be seen from the Table 2 the number of MUAPs, detected in 20s window, increases with the number of active MUs at the beginning (up to four active MUs). With the further increase of the number of active MUs, the number of detected MUAPs arrives to saturation, which may be an indicator of MUAPs overlapping. Overlapping a MUAP by another MUAP from the same muscle changes the MUAP form and may have influence on the estimation of the interelectrode delay, which is the base for propagation estimation. Two overlapping MUAPs may give a wider peak as a sum. At the same time, interelectrode delay estimation can have a higher error for wider peaks. This may be one possible explanation of how the MUAP overlapping changes the propagation estimation.

Moreover, the muscle depth also can influence the direction estimation, because the depth changes the observed MUAP form, making in wider. It may be seen from the figure that for the same number of active MUs, the standard deviation and a mean error is higher for a deeper muscle

In this subsection, we presented how the overlapping of the MUAPs from different MUs of the same muscle may influence direction estimation. It was shown that the precision of the propagation direction decreases with a number of active MUs for both mean error and standard deviation. It was also shown that this precision decrease is higher for deeper muscles. The next subsection shows how the depth estimation is influenced by the MUAP overlapping.

1.5.3. Depth estimation

At the other hand, the MUAP overlapping change the MU depth estimation. Indeed, the sum of two overlapped MUAPs has a form that differs from the individual MUAP waveform that modifies the estimation. Figure 33 shows how the estimated depth of a peak (black), composed by two overlapping MUAPs (pink and blue) with the same form changes as a function of the delay between the composing MUAPs.

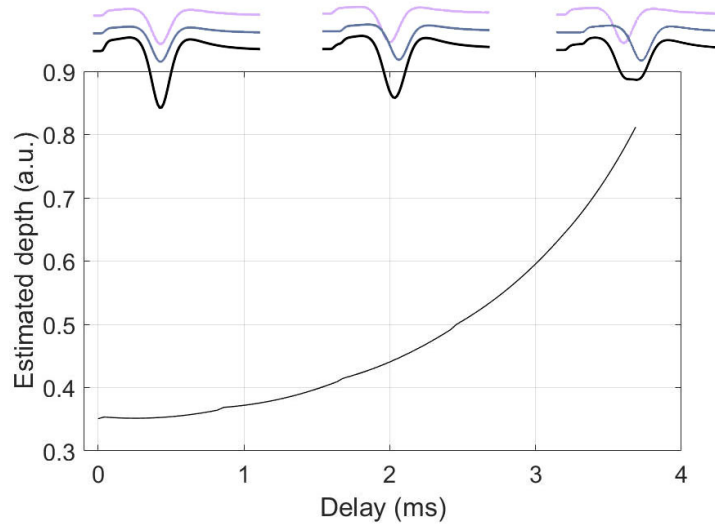


Figure 33 The influence of the delay between two overlapped MUAP with the same properties on the estimated depth

The MUAPs were created with a simulator, and the depth of the resulting peak was calculated using the estimator (41). It is seen from the figure that resulting peak becomes larger with the increase of the delay between the composing MUAPs, which increases the estimated depth of the observed peak.

We used the simulated signals, presented in the [previous subsection](#) to study the influence of the overlapping between the MUAPs from the different MUs of the same muscle on the estimated depth. These signals correspond to the signals from simulated muscles with different number of active MUs. All MUs were concentric, i.e., each MUAP from a muscle has a same depth. However, the observed depth may be deteriorated by MUAP overlappings. Figure 34 shows mean and standard deviation of the estimated depth as a function of a number of recruited MUs in muscle.

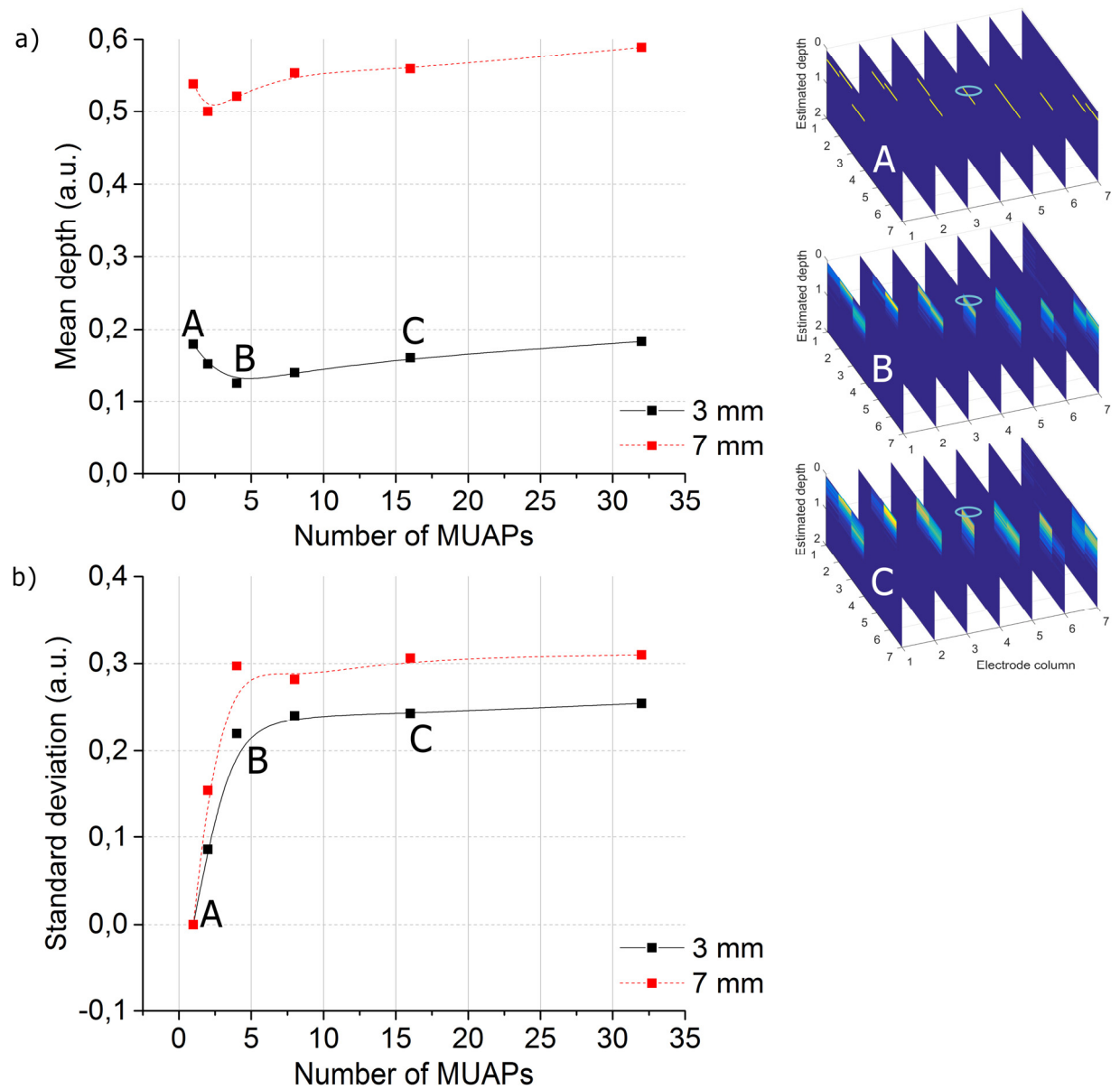


Figure 34. The influence of the number of MUAPs on mean value (a) and standard deviation (b) of the estimated depth. The depth distribution is shown for 1, 4 and 16 MUs (A, B, C)

The images A, B, and C show the estimated MUAP depth distribution for 1, 4, and 14 recruited MUs. It is seen from the figure that mean and standard deviation of the estimated depth increase with the number of active MUs. As it was discussed in [previous subsection](#), the number of overlapping increases with the number of recruited MUs. Two overlapped MUAPs may give a resulting peak, which has properties, different from the composing MUAPs. That affects the depth estimation of the resulting peak. It may be also noticed that the standard deviation of the depth estimation is higher for the deeper muscle, which may be explained by the fact, that the observed MUAPs from the deeper muscle are wider and may strongly affect the depth estimation when overlapping.

The current section deals with the overlapping of the MUAPs from the different MUs of the same muscle. We firstly presented the theoretical model which shows how the number of MUAP overlapping increases with the number of active MUs in muscle. The proposed model showed that for 5 active MUs in

muscle the probability that a MUAP, produced by one of these MUs will not be overlapped by any other MUAP from the other MUs is 0.53. However, we do not take into account the fact, that the overlapping of two MUAPs from remote MUs does not have the same effect on the signal as the overlapping from close MUs. Secondly, we showed how the overlapping of MUAPs from different MUs of the same muscle influences the estimated propagation direction and depth. We showed that the estimated propagation direction and depth of the resulting peak, which is composed of sum of individual MUAPs may be different from that of the composing peaks. We assumed that the muscle consists of parallel fibers grouped in MUs and all MUs in a muscle are concentric, which is a simplified model used to focus only on the effects of MUAP overlapping. The next section shows how the estimation of the MUAP properties may be affected by MUAPs from the second muscle, *i.e.* it deals with crosstalk from different muscles.

1.6. Overlapping of MUAPs from different muscles. Crosstalk problem

In this section, we focus on case, when two muscles are active at the same time, *i.e.* when the crosstalk problem appears. In this case, a MUAP from a MU belonging to one muscle may be overlapped by a MUAP from the second muscle. We assumed that the parameters of the MUAPs from the second muscle (direction, depth) are significantly different from the parameters of the first muscle. We will analyze how overlapping of the MUAPs from different muscles influences the estimation of propagation direction and depth.

1.6.1. Direction estimation

Below we analyze the propagation direction of a sum of MUAPs from different muscles, *i.e.* propagating in different directions. We firstly simulated two MUAPs, the first with the propagation angle -30° and the second with propagation angle equal to 30° . Two MUAPs were multiplied by a weight coefficient and summed in-phase to form an aggregate potential. We studied how the RMS ratio between the composing MUAPs, forming an aggregate potential, influences the estimated direction of the aggregate potential. The RMS ratio was varied by the means of a weight coefficient.

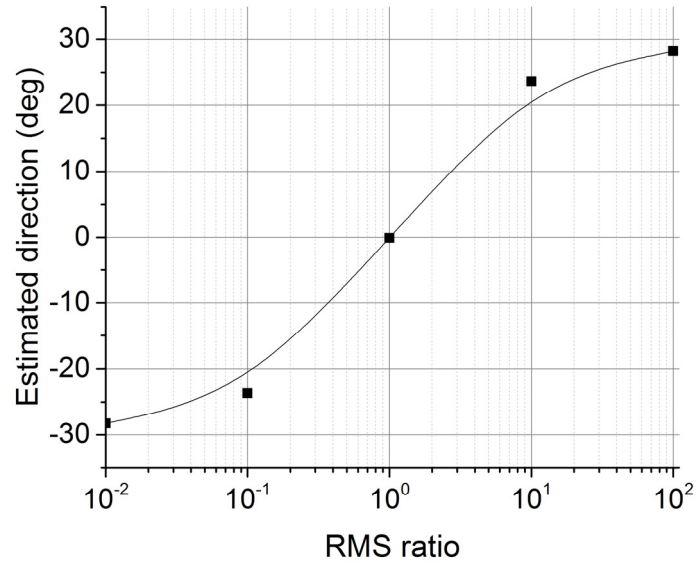


Figure 35. The influence of the RMS ratio of two in-phase overlapped MUAPs, generated by MUs with different direction, on the observed propagation direction of superposed MUAPs. Simulation result.

It may be seen from the figure that the estimated propagation direction of a resulting peak, obtained as a sum of two MUAPs, propagating in different directions is a function of RMS-ratio of overlapping MUAPs. More the power of one MUAP becomes prevailing, more the estimated propagation direction of the resulting peak becomes closer to the real propagation direction of this dominant MUAP.

Secondly, we simulated two intercrossing muscles with different propagation angles, -30° and 30° , and the same depth. We studied how the estimated propagation direction depends on number of active MUs in muscles. Figure 36 shows the visualization of estimated direction for two simultaneously activated intercrossing muscles. The simulation were performed for 1 MU, 4 MU and 16 MUs in each muscle (left, central and right columns). The upper line (images a, b, c) represents the direction maps, which maps the mean direction and standard deviation for all MUAPs detected in the sum of the simulated HD-sEMG signals from two muscles. The middle line (images d, e, f) represents the estimated propagation directions for peaks, detected in the central electrode from the sum of EMG signals. The direction of MUs detected from individual simulated signals of each muscle are shown in the same images for comparison. The lower line (images g, h, i) shows the distribution of the propagation direction of peaks detected in central electrode from the sum of the simulated signals from two muscles.

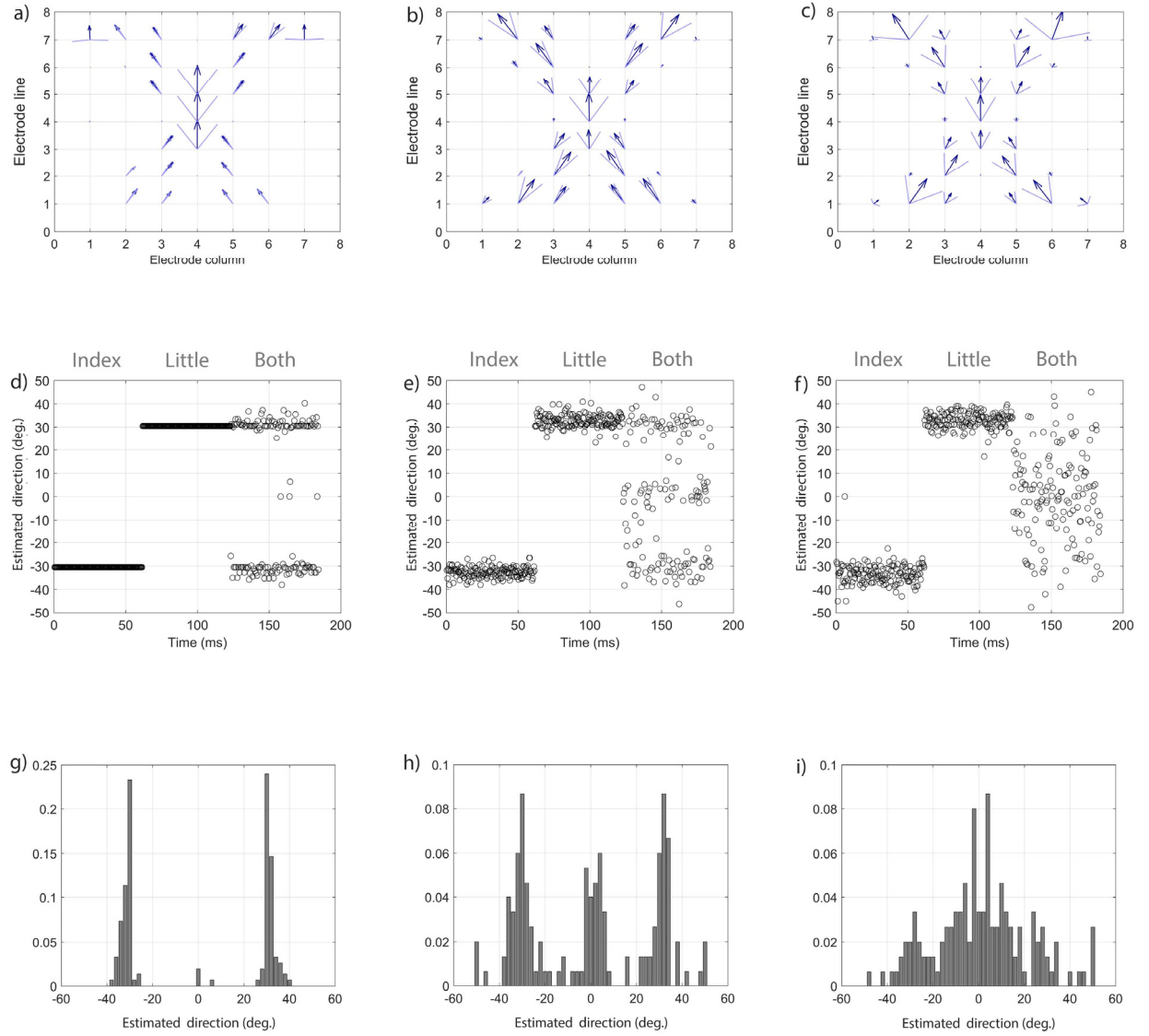


Figure 36. The influence of MU number in intercrossing muscles on direction estimation. Upper line: The estimated direction of peaks detected from intercrossing muscle simultaneous contraction with 1 (a), 4 (b), and 16 (c) MUs in each muscle. Middle line: the estimated direction of peaks detected in electrode 4,4 during the contraction of both muscles for 1 (d), 4 (e), and 16 (f) MUs in each muscle. The figures also contain the estimated directions during individual muscle contraction for comparison. Lower line: the distribution of estimated direction of peaks, detected in electrode 4,4 during the contraction of both muscles for 1 (g), 4 (h), and 16 (i) MUs in each muscle

The left column shows the case when both muscles contain only one active MU. It can be seen from the image (a) that there is almost no variance of the estimated propagation direction in electrodes located along the muscle axes and far from muscle intersection. Image d shows the propagation direction of the peaks detected in central electrode from the signal sum as well as from composing signals. One can notice that most of the peaks, detected from the sum of the signals, have the same direction with the peaks, detected during the individual activation of these muscles. It may be explained by the fact that the signals are sparse and the probability of MUAP overlapping is low. Image g shows the distribution of the propagation direction of the peaks, detected from the sum of simulated signals. As from the previous image, it may be seen that the sum of the simulated signals mostly consists of the non-overlapped peaks which form two distinguishable classes.

When both muscle contain 4 active MUs (central line), the number of overlappings between the MUAPs produced by the MUs of the same muscle increase, as well as a number of overlapping between the MUAPs, produced by MUs of different muscles. It can be seen from the image b, that when the number of MUs increases, the variance of estimated direction increases for located along the muscle axes and far from muscle intersection. From the image e it may be noticed that the estimated propagation direction of the peaks detected from the sum of two signals is distributed between the propagation angle of the MUs in the first and second muscle. One can distinguish from this image the MUAPs from one muscle that are not overlapped by the peaks from the second muscle. They have the same propagation direction that the peaks, detected during individual extension of muscles. The peaks that are the sum of MUAPs produced by MUs of different muscles, have the estimated propagation direction, close to zero. The increase of the number of peaks with estimated propagation direction, which is close to 0 may be seen from the distribution (h).

Finally, when 16 MUs were recruited in both muscles (right column) the variance of the direction estimation in electrodes located over the muscle axes far from the intercrossing zone is higher than in cases where 1 and 4 MUs were recruited. It may be also seen from the image f that in the number of overlapping between the MUAPs from different muscle is very high, therefore, two classes of MUAPs may not be distinguished anymore, as it was in case of 1 and 4 active MUs. One can see from the distribution of the estimated direction from the sum of simulated signals that there is only a small number of MUAPs which are not overlapped and which form two groups around -30° and 30° correspondingly.

In this subsection, we analyzed how the estimated direction of a MUAP may be influenced when a MUAP is overlapped by another MUAP with different propagation direction. In the next subsection, we will study how overlapping between MUAPs from different muscle influence on estimated MUAP depth.

1.6.2. Depth estimation

This subsection is devoted to studying how overlapping of MUAPs from different muscles influence the depth estimation. Similarly with the [previous subsection](#), we firstly focus on a case, when each of two muscles has one active MU. We assumed that two MUAPs appear at the same moment in two muscles, located on different depth. We studied how the RMS ratio between two overlapping MUAPs modifies the depth estimation (Figure 37). The pink waveform corresponds to a MU from a deeper MU, the blue waveform corresponds to a more superficial one, the black one is a sum of the pink and blue waveforms.

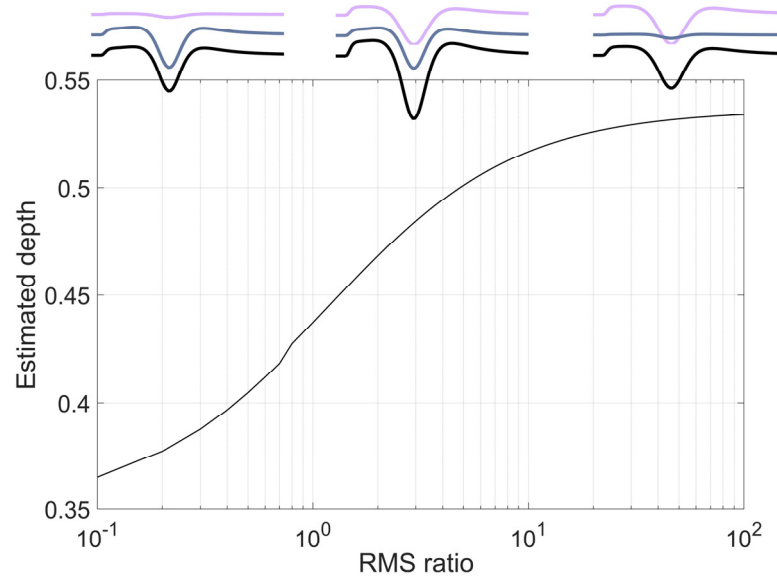


Figure 37. The influence of the RMS ratio of two in-phase overlapped MUAPs, generated by MUs with different depth, on the observed depth of superposed MUAPs. Simulation result.

It may be seen from the Figure 37 that the estimated depth of a resulting peak, obtained as a sum of two MUAPs, from superficial and deep MUs, is a function of RMS-ratio of overlapping MUAPs. More the power of one MUAPs becomes prevailing, more the depth estimation from a peak, which is sum of two MUAPs, becomes close to the real depth of this dominant MUAP. This relation is close to relationship between the estimated propagation direction and RMS-ratio between the MUAPs, composing the resulting peak (Figure 35).

Figure 38 shows the visualization of estimated depth for two simulated muscles with different depth, 3 and 7 mm correspondingly. The simulations were performed for 1 MU, 4 MU and 16 MUs in each muscle (left, central and right columns). The upper line represents the depth maps, where the color corresponds to a number of peaks, detected at each depth for each electrode. The middle line represents the estimated MUs depth for peaks, detected in the central electrode from the sum of simulated signals. The depth of MUs detected during individual simulated signals from each muscle is shown in the same images for comparison. The lower line shows the distribution of the depth of detected peaks during simultaneous muscle extension.

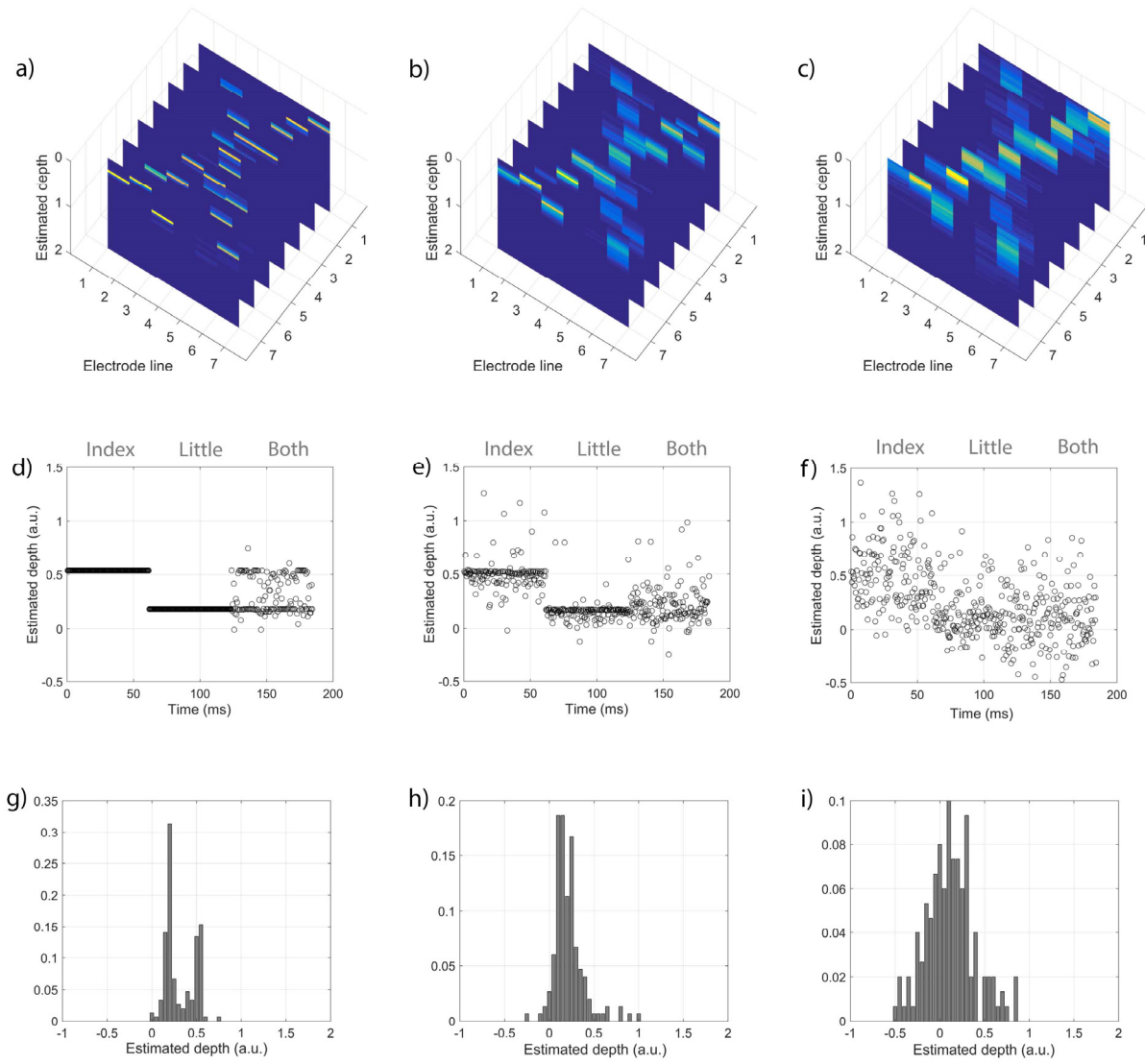


Figure 38. The influence of MU number in intercrossing muscles on depth estimation (simulated signals). Upper line: the estimated depth maps of peaks detected from intercrossing muscle simultaneous contraction with 1 (a), 4 (b), and 16 (c) MUs in each muscle. Middle line: the estimated depth of peaks detected in electrode 4,4 during the contraction of both muscles for 1 (d), 4 (e), and 16 (f) MUs in each muscle. The figures also contain the estimated depths during individual muscle contraction for comparison. Lower line: the distribution of estimated depths of peaks, detected in electrode 4,4 during the contraction of both muscles for 1 (g), 4 (h), and 16 (i) MUs in each muscle.

The left column corresponds to the case when both intercrossing muscles contain only one MU. It is seen from the image that the depth of both muscles is calculated with low variance at the electrodes located along the muscle axes and far from intersection zone. The signal from the central electrode, which lays over the muscle intersection, contains a sum of the signals from two muscles. However, these signals are sparse and only few peaks detected from the signals are overlapped, i.e. have the estimated depth which is different from the estimated depth of the MUAPs from the composing signals (image d). Image g shows the distribution of the estimated depth of the MUAPs detected from a sum of simulated signals at the central electrode. It can be seen from the distribution, that MUAPs from the sum of the signals form two groups with different depth.

When a number of active MUs in muscles increases up to 4 and 16 (central and left column) one can notice an increase of the standard deviation of the depth estimation of the MUAPS detected from the electrodes located along the muscle axis and far from muscle intercrossing (figures b and c). The peaks detected from the sum of simulated signals at the central electrode do not form two classes anymore and their depth is distributed between the depths of the source muscles (figures e and f). It may also be seen that the distributions of the estimated depth of the peaks detected in a signal sum do not form two distinguishable groups anymore (figures h and i).

In this subsection, we analyzed how the estimated depth of a MUAP may be influenced when a MUAP is overlapped by another MUAP with different depth, while the previous subsection was devoted to the similar study of the estimated direction of the overlapping MUAPs. It was shown in both studies that more one MUAPs prevails over the second, more the estimated direction and depth of the resulting peak is close to the direction and depth of a MUAP, which energy is higher. The limitation of this approach is that we studied only the in-phase sum of MUAPs and did not deal with cases when the composing MUAPs are summed with a delay. It was also shown that in case than only one MU was active in both muscles, there was a high number of non-overlapped MUAPs in summarized signal, which estimated direction and depth was similar to those of the MUAPs from initial signal. However, with increase of number of active MUs in muscles, increases the number of overlappings between the MUAPs from different muscles, which form aggregate peaks. The estimated propagation direction and depth of the aggregate peaks lies between those of the composing MUAPs.

This chapter was devoted to detection of the MUAPs and estimating their features: propagation direction and depth. We firstly studied how the estimation performance depends on noise level in non overlapped MUAP simulations. Secondly, we studied the performance of the MUAP feature estimation in case if MUAP is overlapped by a MUAP produced by another active MU of the same muscle. We found that this probability that a MUAP will be overlapped at least by one another MUAP from the different MU of the same muscle is 0.53 (for five active MUs in muscle and the MUAPs parameters, listed in the example in [subsection 1.5.1](#)). Moreover, we studied how the number of active MUs in muscle changes the features of the peaks, detected from the simulated signal. It was shown that the mean error and standard deviation of the features calculated for a set of detected MUAPs increase with the increase of the number of active MUs in muscles. Finally, we analyzed the case when a MUAP is overlapped by a MUAP from another muscle, which has different parameters. We studied how the estimated features of the aggregated peak, formed by an in-phase sum of two MUAPs from different muscles, depend on RMS ratio between the composing MUAPs. It was shown that more one MUAPs prevails over the second, more the estimated features of the aggregated peak are close to the features of a MUAP, which energy is higher. It was also shown that when the number of active MUs in muscles is low, the features of the detected peaks from the summarized signal form two distinguishable groups characterized by different features. In case, when the number of active MUs is high, most of detected peaks are sums of MUAPs from different muscles. The features of these MUAP lie between the features of originating MUAPs.

The next chapter is devoted to classification of the detected MUAPs in two groups, according to source muscle, *extensor indicis* EI or *extensor digiti minimi* EDM, The classification was based on estimated features. We used both simulated and real HD-sEMG signals of the individual activity of the extensor of index finger and little finger and simultaneous activity of both muscles. We firstly study the ability of classifier to distinguish the MUAPs detected from the individual signals at the electrode, located over the muscle intersection. In this case, each detected peak was either an individual MUAP or a sum of MUAPs from different MUs of the same muscle. Secondly, we study the classification of the peaks detected from the signal mixtures (case of crosstalk from different muscle).

Chapter 2 MUAP Classification

The purpose of this chapter is to show how the potentials, detected during muscle activations can be classified according to active muscle using the estimated features. Firstly, we present the ability of the classifier to distinguish the MUAPs detected during the individual activations of index and little finger ([section 2.2](#)). In this case, there is no signal mixture, and each detected peak is assumed either an individual MUAP, or a sum of several MUAPs, produced by the different MUs of the same muscle. The second case, when two muscles are active at the same time with high force level and there is a possibility of overlapping between MUAPs, produced by different muscles, is studied in [section 2.3](#).

2.1. Signal acquisition and simulation

Classification was performed on real and simulated signals. Below we present the experimental protocol for real signal acquisition as well as describe the simulated signals.

2.1.1. Real signal

Subjects performed cyclic isometric extensions of index and little fingers. The subjects were asked to follow a force profile presented on the computer screen (i.e., gradual increase, plateau, gradual decrease) with the plateaus of 30, 50 and 70% maximum voluntary force (MVF) of the respective finger. Each contraction lasted for 7 s (2 s rise time, 3 s plateau, 2 s fall time) with 3-s rest intervals in-between. A bar indicating the currently generated force was displayed on the screen as the feedback for the subject. Each task consisted in 10 isometric repetitions of index finger and little finger extensions, repeated at the three force level. The fingers were activated alternately. To avoid fatigue, the task was split in two recordings of five repetitions each. Before the beginning of the measurement session, the subjects familiarized with the experimental setup and tasks.

The signals recorded in a monopolar mode were filtered forward and backward by with order 8 Butterworth filter in [20; 500] Hz. Also, a notch filter was applied for rejecting the 50 Hz interference. Figure 39 shows the root mean square (RMS) maps of one representative subject during the extension of index finger (a), little finger (b), and simultaneous extension of index and little finger (c). The RMS values were calculated over 40 000 samples of signal (≈ 16 s). One-second window of the signals from the fifth electrode column are shown during the activity of index finger (d), little finger (e) and simultaneous activity of both fingers (f). It can be seen that the same electrode line captures muscle activity during activities of both fingers, therefore these muscles are sources of mutual inference.

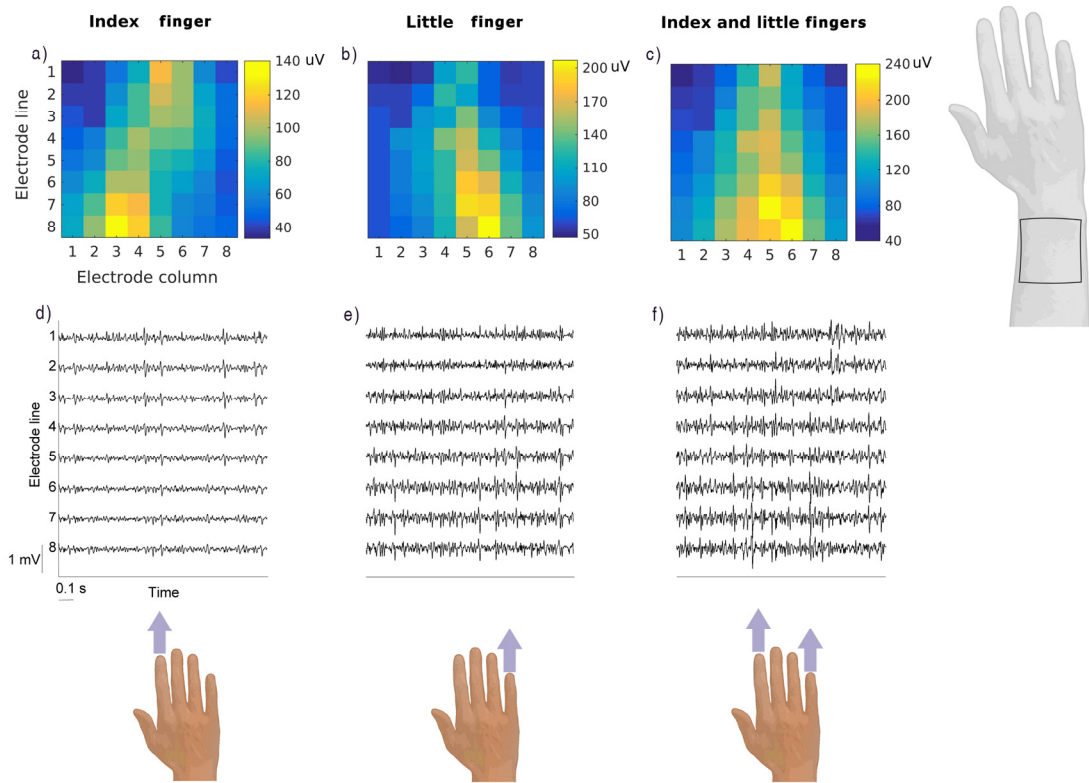


Figure 39. The RMS maps during the extension of index finger (a), little finger (b) and simultaneous extension of index and little finger (c). The corresponding one-second window of signals from the fifth electrode column are shown in figures d,e,f.

2.1.2. Simulated signals

We performed ten simulations of the signals from EI and EDM muscles, which were modeled as a set of parallel fibers. For each simulation we randomly defined such parameters, as the thickness of the fat layer (1.5...6.5 mm), depth and orientation of both muscles (8...14 mm, -20° ... -1° for EI and 4...6 mm, 1° ... 20° for EDM) and number of MUs (25...35 for EI and 5...15 for EDM). Each parameter was generated with a uniform distribution law. The number of fibers in each MU ranged from 25 to 500. Innervation zones of simulated muscles were situated out of the electrode matrix, i.e. the MUAPs in one muscle propagated in the same direction in the area of matrix. The parameters of the simulated recording system were used the same, as in experimental setup (8x8 round electrodes, interelectrode distances 10 mm). The example of signals of one simulation is shown in Figure 40.

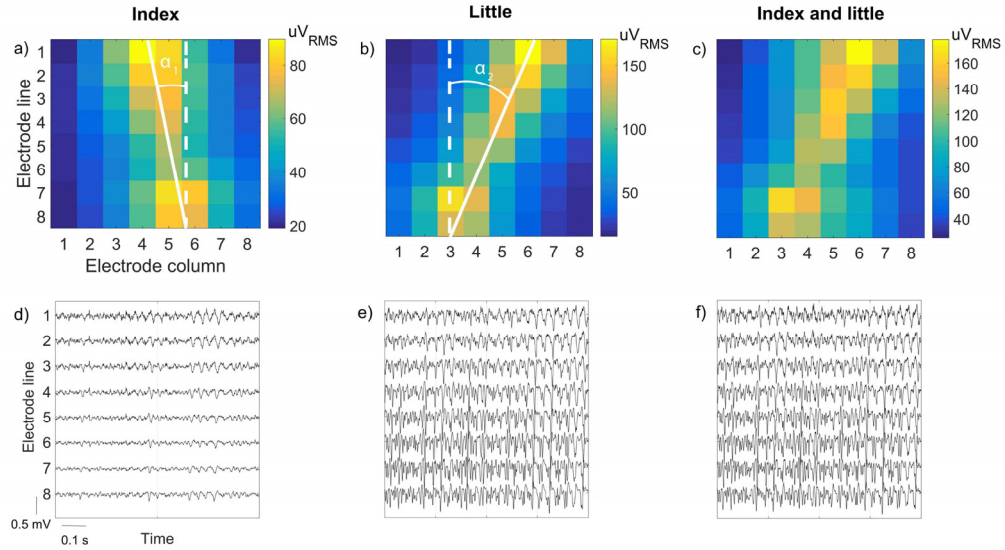


Figure 40. Example of RMS maps of simulated signals from EI (a), EDM (b), and simultaneous activation of EI and EDM (c). The muscle orientations α_1 and α_2 are shown. The corresponding one-second window of signals from the fifth electrode column are shown in figures d,e,f.

Similarly with real signals, we simulated signals, corresponding to 30%, 70% and 70% of MVF. The difference between the signals from different force level was in number of recruited MUs and their firing rates.

2.2. MUAP Classification (unmixed case)

Both real and simulated signals are the 64-channel signals from the electrode matrix. Although the MUAPs were detected in all channels, only one channel was chosen for the classification procedure. This channel was located close to both muscles and, hence, recorded MUAPs from both index and little finger extensors EI and EDM. MUAPs detected in the chosen channel can be described by their features, propagation direction $\hat{\alpha}$ and depth \hat{h} :

$$\mathbf{x}_i = \begin{bmatrix} \hat{\alpha}_i & \hat{h}_i \end{bmatrix}^T, \quad (47)$$

where $i = 1 \dots N$, and N is a number of detected MUAPs.

For the classification procedure we used the signal from individual extension of index and little finger, both recorded and simulated. In other words, the activities of both muscles, EI and EDM, were recorded one after another, and were not subjects to crosstalk. Therefore, for each detected MUAP the source is known *a priori*, which makes possible to label each detected MUAP according to a source muscle. If the number of detected MUAPs from the first muscle was less than the number of MUAPs from the second muscle, the smaller group was completed by randomly chosen MUAPs of the same group.

Given the features of the detected MUAP \mathbf{x}_i , the logistic regression may be used to predict the probabilities that this MUAP was produced either by EI or EDM muscle:

$$\Pr(\text{Index}|\mathbf{x}_i) = \frac{\exp(\beta_0 + \mathbf{x}_i^T \boldsymbol{\beta})}{1 + \exp(\beta_0 + \mathbf{x}_i^T \boldsymbol{\beta})}, \quad (48)$$

$$\Pr(\text{Little}|\mathbf{x}_i) = 1 - \Pr(\text{Index}|\mathbf{x}_i), \quad (49)$$

where β_0 and $\boldsymbol{\beta}$ are the regression coefficients, $\boldsymbol{\beta} \in \mathbb{R}^2$.

According to these probabilities, each detected MUAP may be classified as the index or little finger activity:

$$\begin{aligned} &\text{Index} \quad \text{if} \quad \Pr(\text{Index}|\mathbf{x}_i) > 0.5 \\ &\text{Little} \quad \text{otherwise} \end{aligned} \quad (50)$$

The model was trained and tested for each subject (or each simulation) individually. For a given subject (or simulation), MUAPs, detected in a selected channel during two types of movement were arbitrarily divided into two equal-sized sets, training and test set. The training set was used to estimate the regression coefficients β_0 and $\boldsymbol{\beta}$ for selected channel. The test set was used to calculate the classification performance.

The regression coefficients were estimated using `mnrfit` function (Matlab R2012b, MathWorks, Natwick, MA). Once the model was trained, the z-scores were calculated to estimate the significance of each feature. The z-score (z-value) is the value of the regression coefficient divided by its standard deviation, which is used to evaluate the contribution of the corresponding feature. The performance of trained model was estimated on the test group. We calculated the misclassification rates for each muscle individually, as well as the global misclassification rate. The misclassification rates for both muscles ε_1 and ε_2 were calculated as the ratio of misclassified MUAPs from one muscle to a whole number of detected MUAPs from this muscle. The total misclassification rate ε was calculated as a number of misclassified MUAP from both muscles to a total number of detected MUAPs. Below we firstly present the classification results in simulated signals, and secondly, in real signals.

2.2.1. Simulated signal study

The logistic regression model was trained and tested on each simulation individually. Figure 41 shows the features extracted from the signals from one simulation. Left column corresponds to simulated contraction of index finger (EI muscle), and the right column corresponds to simulated contraction of little finger (EDM muscle). The estimated propagation direction is shown in the upper line, and the estimated propagation depth is shown in lower line.

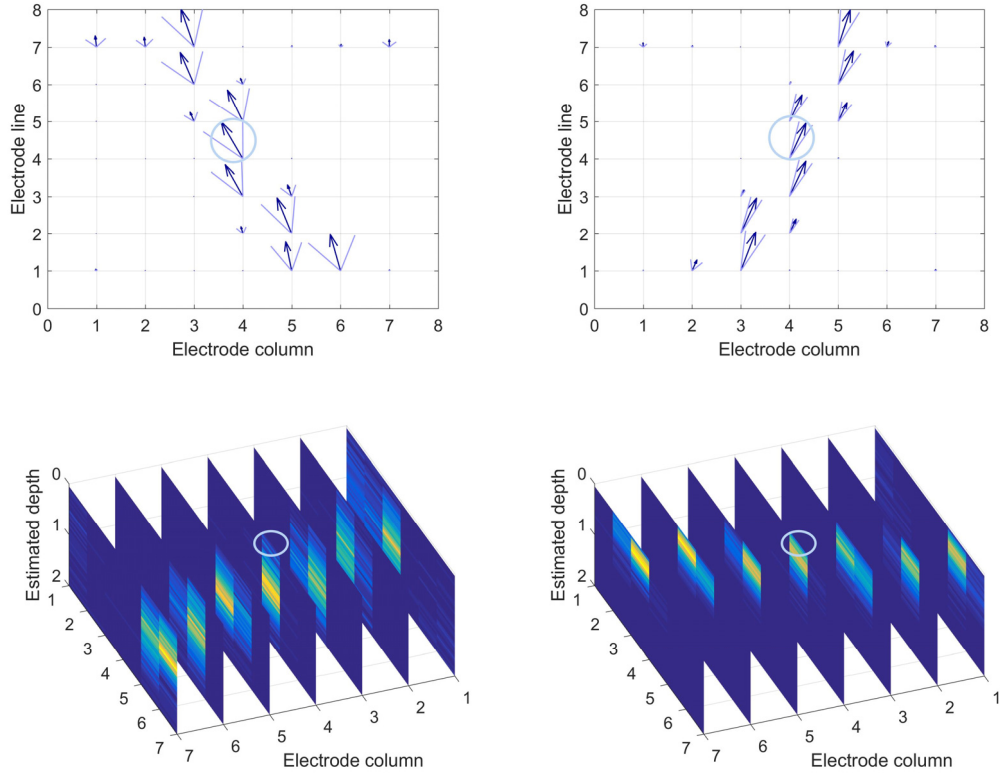


Figure 41. The features extracted from one representative HD EMG signal simulation, corresponding to index and little finger extension (left and right columns correspondingly). Upper line - propagation direction. The direction of each arrow corresponds to mean estimated direction by each electrode, with fine lines which show the standard deviation. Magnitude of each arrow is proportional to number of MUAPs detected by corresponding electrode. Lower line – estimated depth. The color corresponds to number of peaks detected by each electrode. The features are shown from one representative simulation.

The channel selected for MUAP classification is shown by a blue circle ($n_{row}=4, n_{col}=4$). Figure 42 shows the scatter plot of the features from this channel. The features from index finger extensor are represented by blue circles and the features from the little finger extensor by red circles.

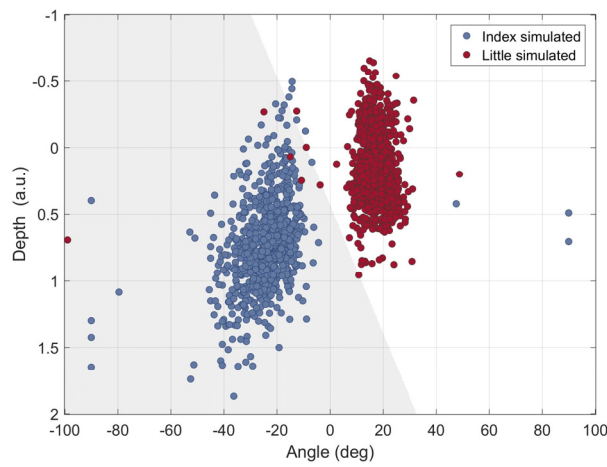


Figure 42, The scatter plot of MUAP features detected in one channel of simulated signals, corresponding to individual index and little finger contraction. The decision boundary is also shown. The features are shown from one representative simulation.

Two different classes of MUAPs, corresponding to activity of EI and EDM are clearly seen from the image. It may be noticed from the figure, that most of the MUAPs are linearly separable. The decision boundary, traced according to estimated regression coefficients is also shown.

For the features, shown in Figure 42, the regression coefficients β , estimated from the learning group was $\beta = [-9.0 \ 3.7]$. The first coefficient β_1 corresponds to propagation angle, and the second coefficient β_2 corresponds to MU depth. The negative value of β_1 indicates that the estimated propagation angle of simulated EI muscle (mean estimated -23.8°) is smaller than the estimated propagation angle of simulated EDM muscle (mean estimated 17.0°). The positive value of β_2 indicates that the estimated depth of simulated EI muscle (mean estimated 0.72 a.u.) is higher than the estimated propagation angle of simulated EDM (mean estimated 0.12 a.u.). The z-scores, corresponding to values of β were $z = [22.2 \ 9.2]$. As the values of z-score are high (z-score > 2) both features may be considered informative. The misclassification rate was low for both muscle activities. For the MUAPs corresponding to the extensor of index and little finger the misclassification rates were $\varepsilon_1 = 0.01$ and $\varepsilon_2 = 0.01$; the total misclassification rate was $\varepsilon = 0.01$.

The classifier was individually trained and tested on MUAPs from one selected channel of each simulation. The mean misclassification rates, regression coefficient and z-scores for all simulations at three force levels are given in Table 3.

Table 3. The mean misclassification rates, regression coefficient and z-score, calculated among all simulations at different force levels

Force, % MVC	$\bar{\varepsilon}_1$	$\bar{\varepsilon}_2$	$\bar{\varepsilon}$	$\bar{\beta}_1$	$\bar{\beta}_2$	\bar{z}_1	\bar{z}_2
30	0.08±0.07	0.03±0.03	0.06±0.05	-12.6±8.8	4.1±1.5	25.9±21.4	14.6±6.0
50	0.09±0.07	0.05±0.04	0.07±0.06	-9.8±7.5	4.2±1.5	24.8±19.1	16.6±5.6
70	0.08±0.07	0.05±0.05	0.07±0.06	-8.9±6.1	4.1±1.7	19.7±12.4	15.3±6.2

It may be seen from the table, that the misclassification rate was moderate for all simulated signals. The table also shows that there is no significant change of the misclassification rate with the increase of the force. It may be explained by the fact that the number of the recruited MUs do not considerably change when the force level increases from 30% to 70% MVC. High variability of regression coefficients corresponds to wide range of angles and depths among different simulation.

2.2.2. Real signal study

Real signals, recorded during individual activation of the extensors of index and little signals were also used. Below we present the classification of the MUAPs detected from the real signals. Figure 43 shows the features extracted during contraction of index (left) and little (right) fingers from the subject #4.

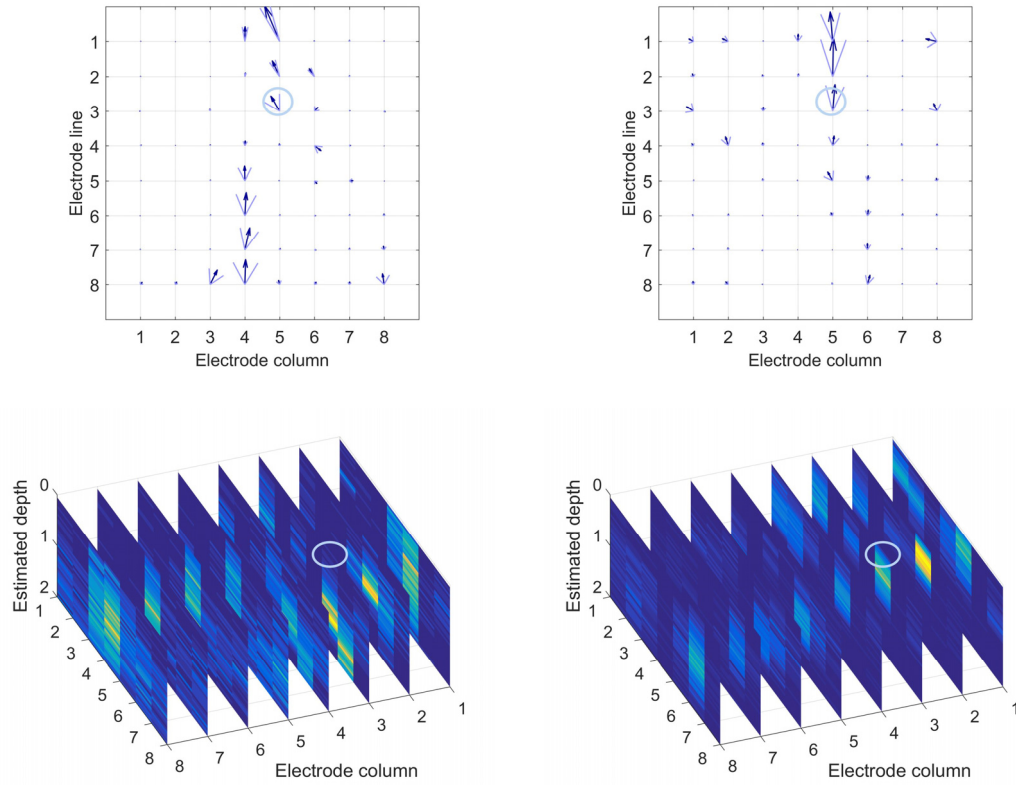


Figure 43. The features extracted from HD EMG signals (subject #4), during index and little finger extension (left and right columns correspondingly). Upper line - propagation direction. The direction of each arrow corresponds to mean estimated direction by each electrode, with fine lines which show the standard deviation. Magnitude of each arrow is proportional to number of MUAPs detected by corresponding electrode. Lower line – estimated depth. The color corresponds to number of peaks detected by each electrode.

The electrode, selected for MUAP classification is shown by a blue circle ($n_{row} = 3, n_{col} = 5$). Figure 44 shows the scatter plot of the features (directions and depth) extracted from the signal from the electrode selected during individual extensions of index and little finger. The features from index finger are represented by blue circles and the features from the little finger are shown by red circles.

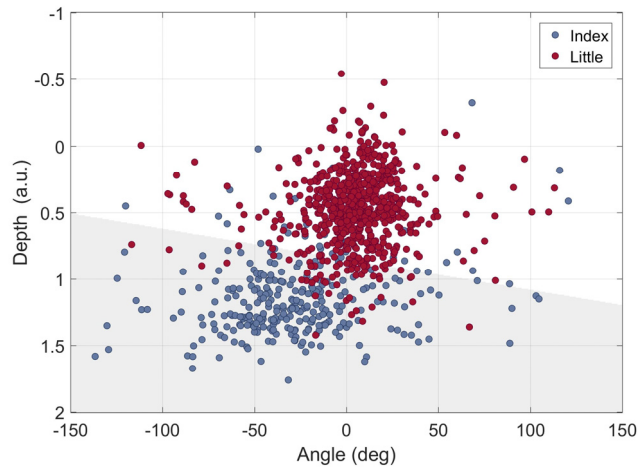


Figure 44. The scatter plot of MUAP features detected during index and little finger contraction for one channel of one representative subject. The decision boundary is also shown.

It can be seen from the figure that when both muscles are activated individually, the features are linearly separable. The potentials corresponding to index finger are characterized by higher depth and angle values. The decision boundary is shown at the same figure as well.

For the features, shown in Figure 44, the regression coefficients β , estimated from the learning group was $\beta = [-1.0 \ 7.3]$. The z-scores, corresponding to values of β were $z = [6.3 \ 18.4]$. As the values of z-score are high (z-score > 2) both features may be considered informative. The misclassification rate was low for both muscle activities. For the MUAPs corresponding to the extensor of index and little finger the misclassification rates were $\varepsilon_1 = 0.11$ and $\varepsilon_2 = 0.10$; the total misclassification rate was $\varepsilon = 0.11$.

The classifier was individually trained and tested on MUAPs from one selected channel of all ten real subjects. The mean misclassification rates for all subjects for three force levels are given in Table 4.

Table 4. The mean misclassification rates, calculated for all subjects at different force levels

Force, % MVC	$\bar{\varepsilon}_1$	$\bar{\varepsilon}_2$	$\bar{\varepsilon}$	$\bar{\beta}_1$	$\bar{\beta}_2$	\bar{z}_1	\bar{z}_2
30	0.15±0.08	0.15±0.07	0.15±0.07	-0.8±2.9	4.0±2.8	9.7±4.8	10.8±4.9
50	0.13±0.09	0.14±0.08	0.14±0.08	-1.5±4.4	4.3±3.0	11.0±4.6	10.5±5.4
70	0.11±0.10	0.13±0.09	0.12±0.09	-2.0±5.4	4.6±3.0	11.2±5.1	11.0±5.3

It may be seen from the table that the error is moderate for all three muscle levels for all subjects and is comparable with the error from the simulated signals. As distinct from simulated signal, the misclassification rate is highest for the muscle activation at the 30% MVC force level. This may be explained by the lower SNR at this force level. One can also notice high variability of regression coefficients. One possible explanation of this variability might be physiological variability between different subjects. Furthermore, it should be noticed that the electrode selected for MUAP classification was chosen according to number of detected MUAPs, and, therefore, was different for different subjects. This fact can also have an influence on variability of the regression model coefficients. One can also notice that the variability of the estimated propagation direction is higher than the variability of estimated depth.

In this section, the ability of the classifier to distinguish between the MUAPs from two muscles, EI and EDM was shown. Activations of these muscles was performed individually, hence, no overlapping of the MUAPs from different muscles was possible (i.e. no signal mixture was present). Each detected peak was either an individual MUAP or a sum of several MUAPs from different MUs of the same muscle. Therefore, each detected may be explicitly classified either as the activity of the index or little finger. In this section, the classifier was trained and tested on signals from each of ten subjects individually. Moreover, the classifier was also trained and tested on simulated signals. It was shown that the classifier correctly determines the class of most detected MUAPs in both real and simulated signals. The second

section presents the case when the muscles were active at the same time, and therefore, overlapping of a MUAP from one muscle by a MUAP from the second muscle was possible.

2.3. MUAP Classification (mixed case)

In this section, we focus on a case when both muscles, index and little finger extensor, were active at the same time. In this case, there were overlappings between MUAPs, produced by these muscles. Hence, most of the detected potential are sums of MUAPs, produced by both muscles, which will be called mixed (or aggregate) peaks.

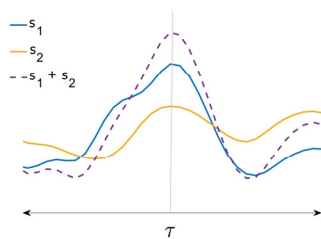
The features of each detected mixed peaks (propagation angle and depth) depend on contributions of two composing muscle activities, as it was shown in [previous chapter](#). When the classifier, presented in [previous section](#) is applied to a mixed peak, its output also depends on contributions of the muscles.

2.3.1. Local and global measure of muscle contributions

Below we propose two measures of muscle contributions, local and global. Local contribution measure may be used to quantify contribution of two active muscles to one mixed peak. For each detected mixed peak i , the ratio r_i between two composing muscle activities s_1 and s_2 was calculated in a short window around the peak τ , as shown in Figure 45a. In current study the length of the window τ was 11 ms.

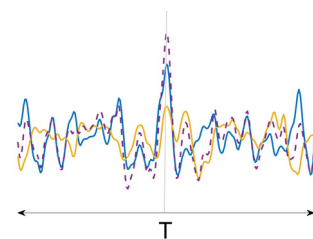
Global contribution measure R is power ratio of two composing signals of the duration T . The ratio R characterizes the contributions of two sources to a mixture during time longer then a duration of one MUAP ($T \gg \tau$), and was calculated as shown in Figure 45b. The value of R depends on the properties of two muscles (depth, PCSA) and on activation levels of both muscles. While the muscle properties stay constant, the muscle activation level may changes, producing the variation of R with time.

a) Energy ratio (one mixed potential)



$$r_i = 10 \cdot \log_{10} \frac{\int_{t_i - \tau/2}^{t_i + \tau/2} s_1^2(t) dt}{\int_{t_i - \tau/2}^{t_i + \tau/2} s_2^2(t) dt}$$

b) Power ratio (the signal)



$$R = 10 \cdot \log_{10} \frac{\int_0^T s_1^2(t) dt}{\int_0^T s_2^2(t) dt}$$

Figure 45. Energy ratio of overlapped MUAPs (a) and power ratio of EMG signals, composing the summarized signal (b)

2.3.2. Link between the muscle contribution and classification results

If both signals, composing the mixture are known, each detected mixed potential may be characterized by an energy ratio of initial signals r_i . From the other hand, each detected mixed potential may be characterized by its feature vector \mathbf{x}_i , which also depend on muscle contributions. A feature vector may be used as an input for logistic regression to estimate the likelihood that this mixed peak was produced by the index finger extensor $\Pr(\text{Index}|\mathbf{x}_i)$.

When the contribution of one muscle in a mixed potential increases, the features of this mixed potential converge to the features of a MUAP, produced by this muscle in absence of the activity of the second muscle. Therefore, the likelihood that the potential is produced by this muscle also increases. In other words, the higher the contribution of one muscle in a mixed potential is, the higher is the likelihood that the mixed potential is produced by this muscle.

A linear regression may be introduced to link the energy ratio r_i with the likelihood $\Pr(\text{Index}|\mathbf{x}_i)$.

$$r_i = a \cdot \Pr(\text{Index}|\mathbf{x}_i) + b + n, \quad (51)$$

where n is noise, a and b – regression coefficients.

The whole mixed signal may be characterized by the global power ratio R . On the other hand, the mixed signal is composed by MUAPs, which may be mixed or unmixed. We introduced a ratio γ to characterize a ratio between the number of potentials classified as activity of the first muscle to the number of potentials, classified as the activity of the second muscle in a mixed signals under study. This ratio was calculated as a logarithm of a ratio of a number of peaks classified as index finger activity N_1 to a number of mixed peaks classified as little finger activity N_2 :

$$\gamma = \log_{10} \frac{N_1}{N_2}. \quad (52)$$

When the power of one source increases, the number of mixed potentials, attributed to this source also increases. In extreme cases, when the power of one signal is zero, γ is equal to classification error in absence of the second muscle activity. In this section, we analyze if there is a relationship between the classification ratio γ and a global power ratio R :

$$R \propto \gamma. \quad (53)$$

If this ratio exists, γ may be used to estimate the power ratio of composing signals for mixed signals, when the composing signals are unknown.

In this section, we firstly present the classification of the mixed potential in simulated and pseudoreal mixtures. Simulated mixtures are the EMG signals of two muscles, created with an EMG

simulator. Pseudoreal mixtures (or artificial mixtures of real signals) are the sums of real EMG signals, recorded during individual muscle contractions. In these two cases, the information about the source signals is available, hence the energy ratio r_i may be calculated for each detected mixed potential, as well as power ratio R may be calculated for the whole mixture. Secondly, we present the mixed potential classification in real mixtures, recorded during simultaneous contraction of both muscles. Contrary to simulated and pseudoreal mixtures, no information about the source contribution is available in real mixtures.

2.3.3. Simulated mixture study

In this section we present the results of peaks classification in simulated mixtures, created as the sum of simulated signals of index and little finger extension. The contributions of the sources to the mixture (R and r_i) are known.

Figure 46 shows the scatter plot of features detected in the simulated signals, composing the mixture (left) and the scatter plot of the features detected from the simulated mixture.

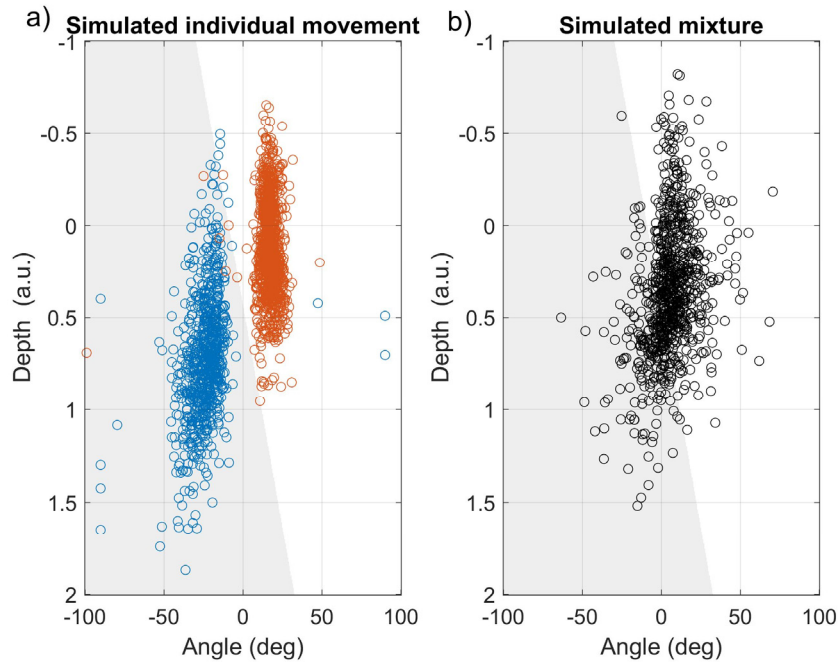


Figure 46. The scatter plot of the features detected in simulated signals (a) and in mixture of simulated signals (b)

It is seen from the figure that the form of the scatter of the features detected from the simulated mixture is close to the form of the joint scatter of the features detected during individual movements. Figure 47 shows the scatter plot of the likelihood that the i -th mixed potential was produced by index finger extensor versus the power ratio of the signals, composing this potential.

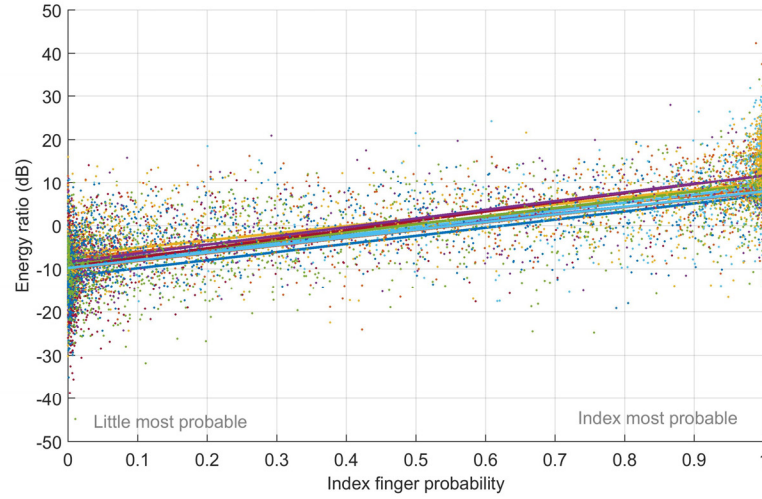


Figure 47. The relationship between the likelihood that the i -th detected MUAP to be produced by an index finger and a contribution of index finger extensor to mixed potential (all simulated subjects).

It can be seen from the figure that the likelihood that the mixed MUAP is produced by little finger extensor is high when the contribution of little finger extensor is also high. The values of the coefficients a and b of the regression model (51) among all ten simulations were -8.1 ± 1.9 and 9.0 ± 1.8 (mean \pm standard deviation). The values of R^2 were 0.11 ± 0.05 . These results shows that the regression does not completely explain the relationship between the energy ratio r and the estimated likelihood $\Pr(\text{Index}|\mathbf{x}_i)$. One possible explanation of this error may be that the model only takes into account the energy ratio between the source MUAPs and does not take into account possible delay between overlapped MUAPs.

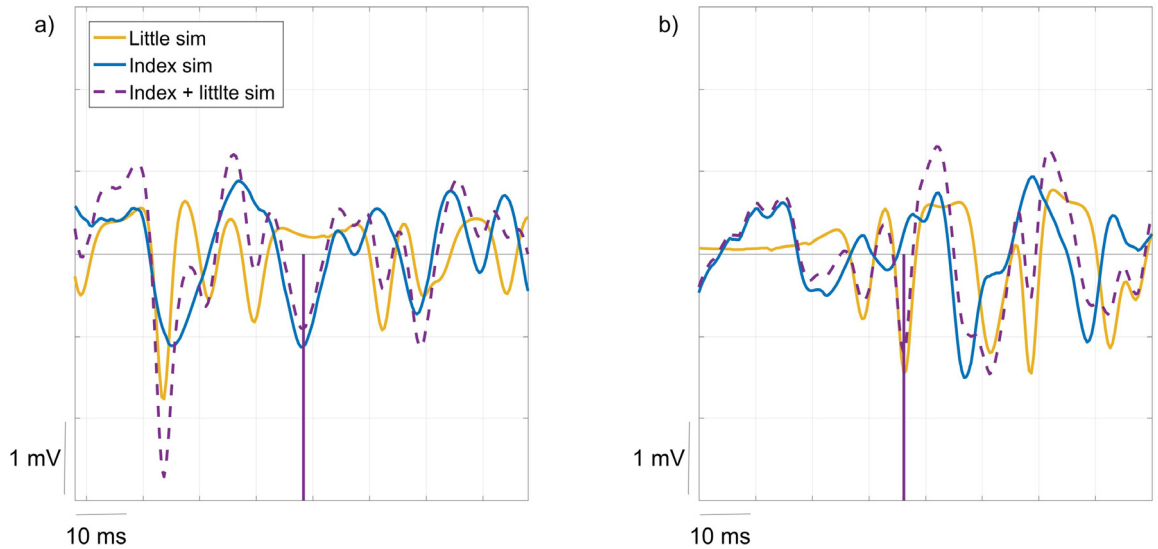


Figure 48. a) A peak detected in a simulated mixture and classified as a little finger with likelihood $P = 0.9$; b) A peak detected in a mixture and classified as a little finger activity with likelihood $P = 0.9$.

Figure 48 shows the simulated mixture (dotted line) and composing signals. Figure 48a shows a mixed MUAP with likelihood 0.9 to be produced by index finger extensors and Figure 48b shows a mixed

MUAP with likelihood 0.9 to be produced by little finger. It may be noticed that one source is prevailing in these peaks.

When the power ratio of the signals changes R (force of one muscle increases), it also changes the energy ratio between the MUAPs, composing the mixed potentials, therefore, it may influence the ratio γ between the number of peaks, classified as first muscle to a number of peaks, classified as second muscle. Figure 49 shows the relationship between R and γ for all ten simulations.

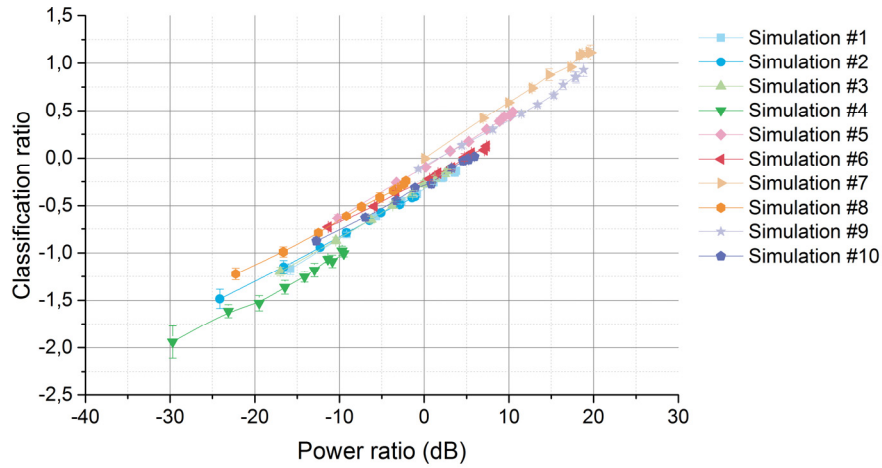


Figure 49. The relationship between the ratio of index and little finger muscle force and log-ratio of peaks classified as index and little finger (all simulations). The power ratio between index and little finger signal. Ordinate: log-ratio of the number of peaks classified as index and little finger.

It may be seen from the figure that linear relationship between R and γ may be observed for all simulations.

2.3.4. Pseudoreal mixture study

In this subsection, we present the results of peaks classification in pseudoreal mixtures, created as the sum of real signals, recorded during individual extension of index and little finger. The advantage of these mixtures is that they consist of real signals, but the components of the mixtures are known.

Figure 50 shows the scatter plot of features detected in the real signals, composing the sum (left), and the scatter plot of features, detected in the pseudomixture (right). The presented signals correspond to the subject #4.

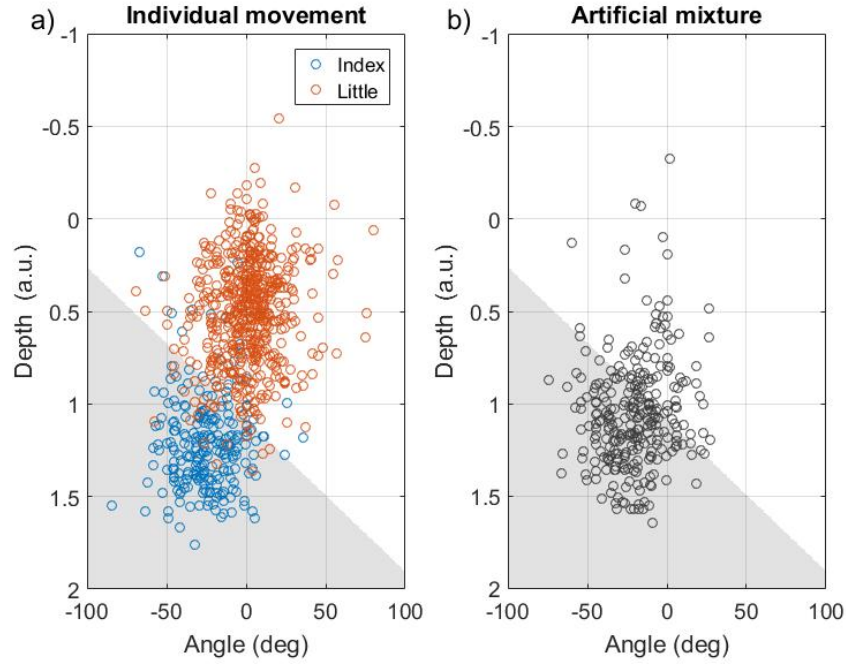


Figure 50. The scatter plot of the features detected in individual signals, subject #4 (a) and in the mixture of individual signals (psedoreal mixture) (b).

It is seen from the figure that the form of the scatter of the features detected from the pseudoreal mixture is close to the form of the joint scatter of the features detected during individual movements.

Figure 51 shows the relationship of the probability of a mixed potential to be classified as index finger activity and the power ratio of composing activities.

When the power ratio of the signals changes, it also changes the energy ratio between the MUAPs, composing the mixed MUAP.

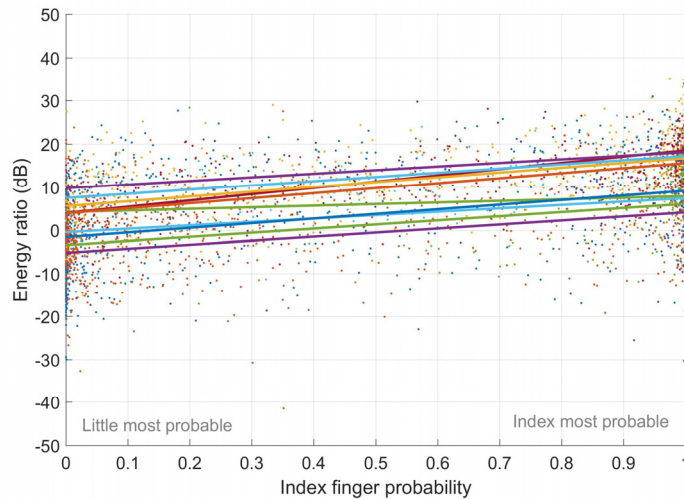


Figure 51. The relationship between the likelihood that the i -th detected MUAP to be produced by an index finger and a contribution of index finger extensor to mixed potential (all simulated subjects).

The values of the coefficients a and b of the regression model (51) among all ten subjects were 2.4 ± 2.8 and 9.6 ± 4.9 (mean \pm standard deviation). The values of R^2 were 0.18 ± 0.10 . These results shows that the regression does not completely explain the relationship between the energy ratio r and the estimated likelihood $\Pr(\text{Index} | \mathbf{x}_i)$. These results are similar with those from simulated mixtures study.

Figure 52 shows the pseudoreal mixture (dotted line) and composing signals. Figure 52a shows a mixed MUAP with likelihood 0.9 to be produced by index finger extensors and Figure 52b shows a mixed MUAP with high likelihood 0.9 to be produced by little finger.

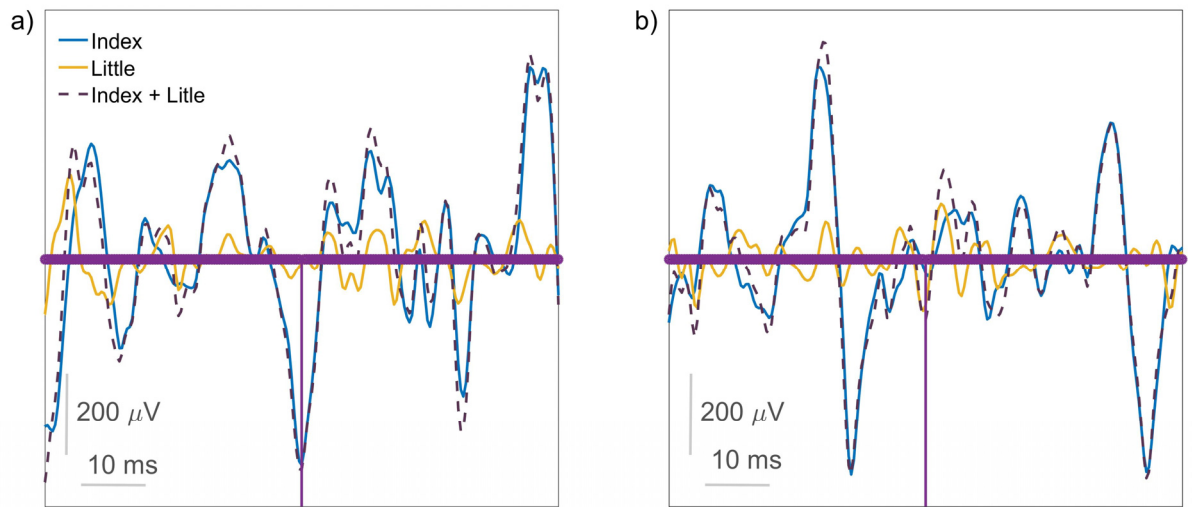


Figure 52. a) A peak detected in a mixture and classified as a little finger with likelihood $P = 0.9$; b) A peak detected in a mixture and classified as a little finger activity with likelihood $P = 0.9$.

It may be noticed from the figure that both selected MUAPs are only slightly overlapped by the MUAPs from the second muscle.

Figure 53 shows the relationship between the power ratio of composing signals R and a ratio between the number of potentials, classified as index finger to a number of potentials, classified as a little finger activity γ .

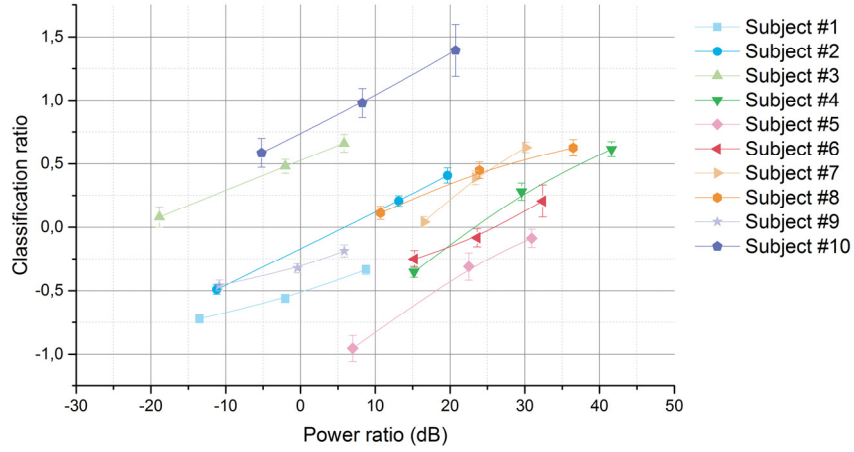


Figure 53. The relationship between the ratio of index and little finger muscle force and log-ratio of peaks classified as index and little finger (all subjects). Abscissa: The power ratio between index and little finger signal. Ordinate: log-ratio of the number of peaks classified as index and little finder.

A linear relationship between the ratio R and γ is seen for all subjects. A considerable variability between the curves may be explained by the physiological variability among the subjects.

2.3.5. Real mixture study

Below we present the results of peaks classification in real mixtures, recorded during simultaneous extension of index and little finger. Figure 54 shows the features extracted from one HD-sEMG channel of the subject #4 during individual extension of index and little finger (a) and during simultaneous extension of index and little finger. The force of both muscles was 50% of its MVF.

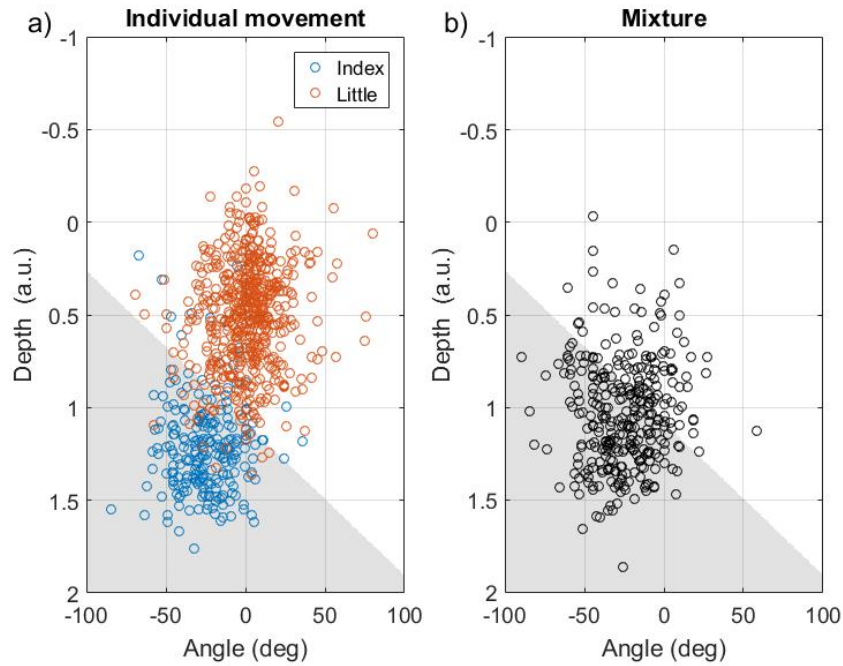


Figure 54. The scatter plot of the features detected in individual signals, subject #4 (a) and in the features, recorded during simultaneous activation of both fingers (real mixture) (b).

Among 318 detected peaks from the mixed signal 180 peaks were classified as activity of index finger extensor EI (57%) and 138 classified as activity of little finger extensor EDM (43%). Figure 55 shows a sequence of detected peaks in a mixed signals. For each peak a likelihood to be produced by the extensor of index finger is shown.

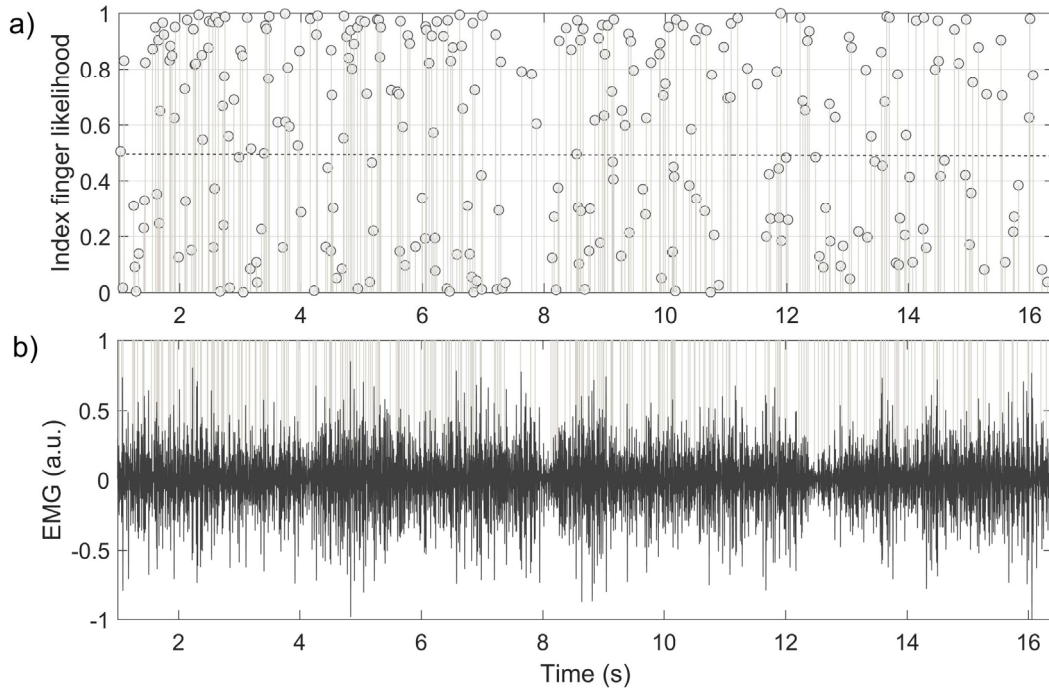


Figure 55 (a) A likelihood for each peak to be produced by the extensor of index finger (b) A time-localization of the peaks in EMG signals.

It is seen that among the peaks, detected in the signal mixture, the number of the peaks having high likelihood to be produced by EI muscle and having high likelihood to be produced by EDM muscle is approximately the same. It may also be noticed that the peaks with different likelihood are homogeneously allocated in signal.

In this subsection we have shown that the aggregated peaks detected from the real mixture of EMG signals have the same properties as the peaks detected from the artificial mixture of real EMG signals. Therefore, in a real mixture a ratio γ between the number of peaks classified as activity of EI to a number of peaks, classified as the activity of little finger might be used as an indicator of the ratio between the activations of two muscles. However, further studies are required to find a precise relationship between γ and muscle activations, and furthermore, muscle forces.

Conclusion

The purpose of this part was to estimate the activations of two finger extensor muscles, *extensor indicis* and *extensor digiti minimi*, which are the extensors of index and little finger correspondingly and are located in a distal part of the forearm. The activations of these muscles were estimated from the HD-sEMG signals, that were either individual activities of these muscles, or simultaneous activity of both muscles at the same time. In case, when these muscles were active at the same time, they created a significant amount of mutual crosstalk.

We proposed a method that can estimate the activations of these muscles either from signals, corresponding to individual muscle activities, or from the signal mixture, recorded during simultaneous finger activities. The proposed using HD-sEMG recordings. The method is based on detecting peaks in a channel of interest and applying a logistic regression to the peaks' features to determine the originating muscle of each detected peak. The detected peaks may be either individual MUAPs (or a sum of MUAPs, produced by the MUs of one muscle), or a sum of MUAPs produced by MUs in different muscles. In the first case, an output of the logistic regression is the class, corresponding to originating muscle. In the second case, the output of the logistic regression was shown to depend on power ratio of superposed MUAPs.

The first stage of this algorithm is the MUAP detection. The MUAPs we detected in the space of signal wavelet transform. We proposed the direction and depth estimators and evaluated their performance in estimating the features of individual (non-overlapped) MUAPs. We also analyzed how the performance of the estimator change when MUAPs becomes overlapped by MUAPs produced by other MUs of the same muscle. Moreover, we studied the feature estimation in case when MUAP was overlapped by MUAPs produced by another muscle (crosstalk case).

A logistic regression model was trained on a set of MUAPs, detected during individual extensions of index and little finger.

Finally, the potentials were detected in mixtures of signals: simulated signals, pseudoreal mixtures – artificial mixtures of the signals, recorded during individual activation of two muscles, and real mixtures, recorded during simultaneous extension of index and little finger. The logistic regression was applied to features of each detected peak to estimate the contributions of two muscles to this peak. Hence, from the sequence of detected peaks two firing sequences may be reconstructed.

As a perspective of this work, the obtained firing sequences may be used to estimate activations of two muscles. As one possibility of calculating muscle activation, the firing sequences may be convoluted with a mechanical impulse response of the MU.

Figure 56 shows the recorded HD-sEMG signals and reconstructed activations of two muscles, that were obtained by convoluting the estimated firing sequence of two muscles by Gaussian function. It may be seen from the image, that reconstructed activations follow the measured muscle force.

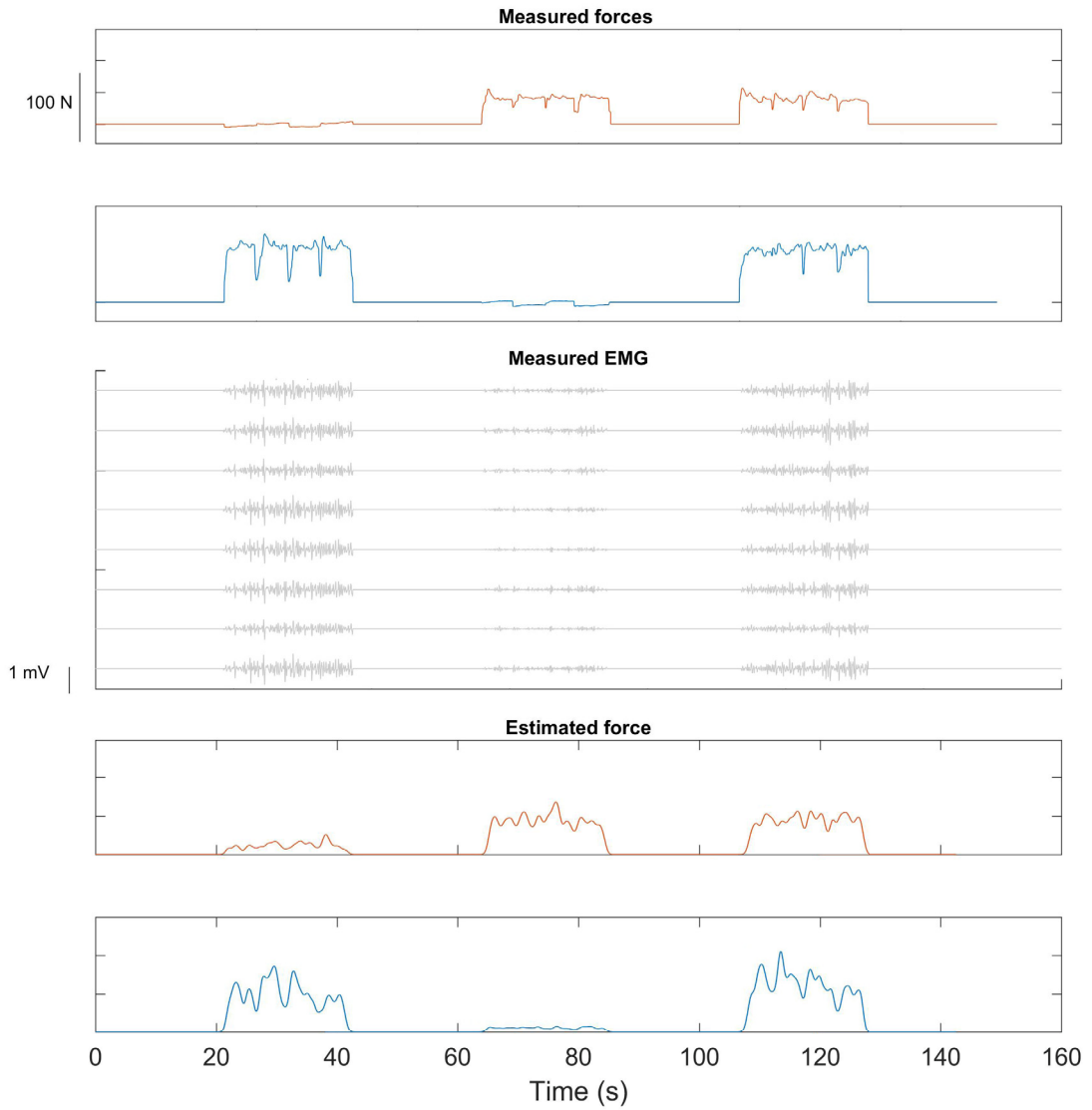


Figure 56. Measured finger forces, HD-SEMG signals, and reconstructed activations of two muscles.

However, the activation is measured in relative units. To convert the estimated activation to muscle force, the further study must be performed.

Once the activations are transformed to a muscle force in Newton, it may be used as an input of the biomechanical model, i.e., applied to the extensor mechanism model. The modelling of the extensor mechanism is presented in detailed in the next part.

Part 3. The extensor mechanism modelling


$$\mathbf{w}(\mathbf{q}) = \mathbf{J}(\mathbf{q})^{-T} \mathbf{R}(\mathbf{q}) \mathbf{E}(\mathbf{q}) \mathbf{F}(\mathbf{q}) \mathbf{a}$$

Introduction

This part of the thesis is devoted to extensor mechanism modelling. The extensor mechanism (EM) of the finger (the extensor apparatus, extensor expansion, extensor assembly, dorsal aponeurosis, etc.) is a complex anatomical structure, which transmits the forces of the extrinsic and intrinsic hand muscles to the finger joints. It is situated on the dorsal surface of the finger bones. The EM is involved in both extension and flexion of the finger joints.

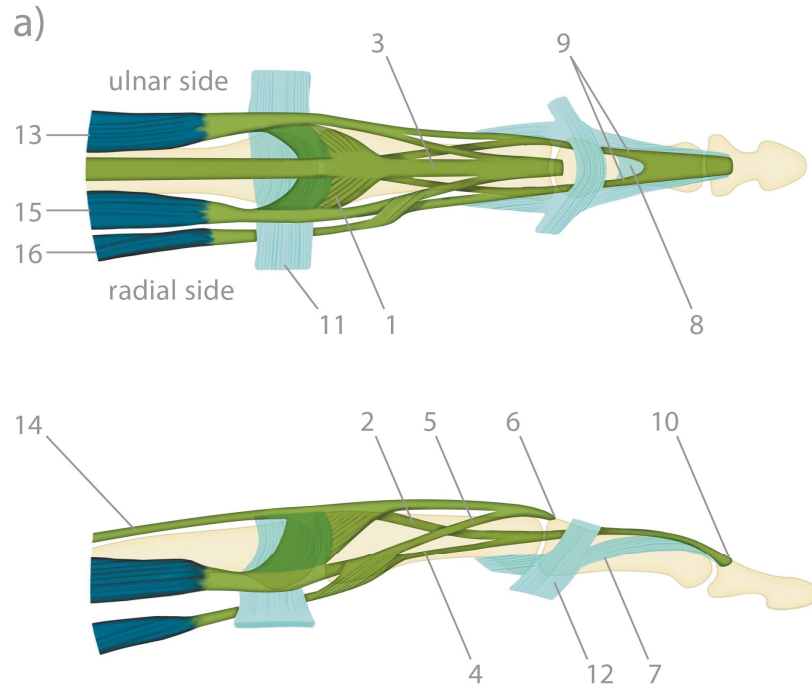


Figure 57. The simplified anatomic view of the extensor mechanism including muscles (blue; 13, 15, 16), tendons (green; 1, 6, 9, 10), and ligaments (light blue; 7, 8, 11, 12);

Figure 57 represents the anatomic view of the long finger EM (Dogadov et al., 2017). It consists of the tendons, which convey the muscle forces to the joints (shown in green), and the ligaments (shown in light-blue) which maintain the tendons and stabilize the joints (el-Gammal et al., 1993; Rockwell et al., 2000). With reference to equation (16), the state of the extensor mechanism depends on posture \mathbf{q} , defined by the joints angles. Variations of the finger posture changes the force distribution among the extensor mechanism bands $\mathbf{E}(\mathbf{q})$ and their moment arms $\mathbf{R}(\mathbf{q})$.

Owing to its important role in force transmission, the EM has been incorporated into biomechanical models of the finger (Hu et al., 2014; Vigouroux et al., 2007). It is usually modeled by an equation system (8), proposed by Chao *et al.* (1989), which represents the internal-force distribution in the tendon network:

$$\begin{cases} f_{te} = 1.000 f_{ub} + 1.000 f_{rb} \\ f_{rb} = 0.167 \varphi_{ed} + 0.133 \varphi_{ri} + 0.667 \varphi_{lu} \\ f_{ub} = 0.313 \varphi_{ui} + 0.167 \varphi_{ed} \\ f_{me} = 0.313 \varphi_{ui} + 0.167 \varphi_{ed} + 0.133 \varphi_{ri} + 0.333 \varphi_{lu} \end{cases},$$

This equation system has already been presented in introduction (section 1.2.). This system is widely used for muscle force estimation (Vigouroux et al., 2007) but present one major limitation. This is that the coefficients in (8) are constant numbers experimentally defined only for fully extended posture. In other words, this approach models the force distribution among the extensor mechanism bands by a constant matrix \mathbf{E} . However, the EM deforms with finger flexion, which makes the values of \mathbf{E} vary. Hence, the equation system (8) is valid only for fully extended finger and can not be directly used for any postures different from the full extension. To overcome this limitation, finger models usually include optimization procedures in order to determine these coefficients for various finger postures (Brook et al., 1995; Vigouroux et al., 2007). However, to our knowledge, no deep analysis of determined coefficients has been performed, making their relevance hard to determine.

The purpose of this section was to perform a deeper analysis of the extensor mechanism deformation with posture to estimate the evolution of matrices $\mathbf{E}(\mathbf{q})$ and $\mathbf{R}(\mathbf{q})$ with posture.

Part 3

$$\mathbf{w}(\mathbf{q}) = \mathbf{J}(\mathbf{q})^{-T} \mathbf{R}(\mathbf{q}) \mathbf{E}(\mathbf{q}) \mathbf{F}(\mathbf{q}) \mathbf{a}$$

Two models of the extensor mechanism with different topologies were compared. These models were

- 1) the individual band model, which presents all elements of the extensor mechanism as individual elastic strings (Figure 58). This model was published in (Dogadov et al., 2017);
- 2) the membrane model, including the extensor hood and a triangular ligament as membranes (Figure 59). This model also contains two layers of intercrossing fibers. This model was created in collaboration with Brain-Body Dynamics Lab (USC, Los Angeles).

This part is organized as follows: section 2 presents the computation algorithm used for the extensor mechanism simulation with different topologies; section 3 focuses on the influence of the model parameters on output force; section 4 analyzes how the extensor mechanism deformation with postural variation changes the fingertip force; finally, section 5 analyzes how the extensor mechanism deformation with the level muscle activation variation influences the fingertip force.

Chapter 1. Model description

The purpose of this section is to present the computational model of the extensor mechanism. We will firstly present the algorithm, used for modelling, and secondly we will describe three topologies of the extensor mechanism, compared in current part.

1.1. Simulation algorithm

The computational environment for the extensor mechanism modeling was written using Matlab 2015 (MathWorks, Natwick, MA) and C++. The developed environment allows representing of the extensor mechanism by principal building blocks: strings, membranes and fiber layers. Each building block consist of a sequence of points, pairwise connected by elastic elements with a linear law. Hence, the EM position was represented by the array \mathbf{x} of x,y,z-coordinates of points forming the EM. Each two sequential points, discretizing an EM band, were connected by a spring with a linear elasticity model.

The bone system was represented by four cylindrical surfaces, corresponding to metacarpal (mc), proximal phalanx (p_1), intermediate phalanx (p_2), distal phalanx (p_3) and three spherical surfaces, corresponding to DIP, PIP and MCP joints (Fig. 1b). The distances between the centers of two neighboring joints (or, in the case of p_3 , between the joint and the end of the bone) are called the segment lengths. They were calculated using the anthropometric survey (Buchholz et al., 1992) as 81.60 ± 5.97 mm (mc) 48.66 ± 3.78 mm (p_1) 31.10 ± 2.62 mm (p_2) and 19.76 ± 1.86 mm (p_3). The diameters of the cylinders and spheres were estimated from (Darowish et al., 2015).

The bone surface σ was completed by three cylinders, perpendicular to the bones (a, b, c in Figure 58). The first two cylinders at MCP level replace the function of pulleys that prevent tendons from bowstringing (Stack, 1963). The third cylinder at PIP level prevents the tendons from descending lower than the joint axes. In real finger, this effect could be partially reached due to the condyle protuberances of p_2 head (Zancolli, 1979).

The forces of dorsal ulnar interosseous, extensor digitorum, dorsal radial interosseous and lumbrical muscle were used as external ones. Their values will henceforth be denoted as $\Phi = [\Phi_{ui} \ \Phi_{ed} \ \Phi_{ri} \ \Phi_{lu}]^T$. The force values Φ were chosen to be in the same range, that the forces used in the cadaveric studies by (Garcia-Elias et al., 1991) and (Hurlbut and Adams, 1995).

The forces were directed from the ends of the tendons to fixed points around the shaft of mc -bone. The points were fixed at the middle of the mc -bone length. The locations of these points were estimated from the tomographic images (Landsmeer, 1976). In the system of the mc -bone the polar coordinates (r ; φ) of these points were: for ui -muscle ($1,4 \cdot r_{mc}$; 103°), for ed -muscle ($1,4 \cdot r_{mc}$; 0°) for ri -muscle ($1,4 \cdot r_{mc}$; -100°) for lu -muscle ($1,4 \cdot r_{mc}$; -134°).

The initial geometrical arrangement of the EM nodal points was made according to anatomical data (Chao et al., 1989). All points forming the bands were located between the main points, connecting them by the shortest possible path. The fingertip was considered to be counterbalanced by an external force and torque, hence no skeleton movement was allowed. The algorithm described below was used to find a state

of the EM in which the internal forces in the bands balance the muscle forces, applied to the EM. The system was assumed to be a conservative one, as the friction between the tendons and the bones is known to be insignificant because of lubrication (Theobald et al., 2012). Thus, the principle of Minimum Potential Energy (MPE) was used to find the equilibrium state. The potential energy PE of the EM was calculated as a sum of the strain energy SE of the system and work potential of the muscle forces WP . The PE of the extensor mechanism, defined by array \mathbf{x} , was calculated according to (54) at iteration k .

$$PE(\mathbf{x}_{k+1}) = SE(\mathbf{x}_{k+1}) + WP(\mathbf{x}_{k+1}, \mathbf{x}_k, \Phi) + g_{1,2}(\mathbf{x}_{k+1}), \quad (54)$$

where $g_{1,2}$ represents penalty terms, defined below.

The SE of the system at $k + 1$ iteration was calculated as a sum of the potential energy of all springs forming the EM. The WP at $k + 1$ iteration was calculated as the work of muscle forces Φ required to displace four points of muscle force application from their previous positions at iteration k .

The penalty terms were added to take into account the following constraints

1. The points were required not to penetrate the bone surface σ . For points violating this constraint the penalty term was added, that was equal to a square of penetration depth d weight by a coefficient β ($\beta=0.04$ N/mm).

$$g_1(x_i) = \beta \cdot d(x_i, \sigma)^2. \quad (55)$$

2. The points lying on the medial plane Π (AB, BC, CD, and EI) were required not to shift from the plane.

$$g_2(x_i) = \beta \cdot d(x_i, \Pi)^2, \quad (56)$$

The Broyden–Fletcher–Goldfarb–Shanno method (BFGS) was used to find the minimum of potential energy. The array \mathbf{x} at iteration $k+1$ was calculated as:

$$\mathbf{x}_{k+1} = \mathbf{x}_k - \mathbf{H}_k \cdot \nabla PE, \quad (57)$$

where \mathbf{H} is a BFGS approximation to the Hessian matrix. The coordinates \mathbf{x} of the points, forming the EM, were iteratively recalculated until convergence.

1.2. Analyzed topologies

Two topologies of the extensor mechanism were created and compared: the individual band model and the membrane model.

1.2.1. Individual band model

Figure 58 shows the components of the EM included to the individual bands model (see Table 5 for details).

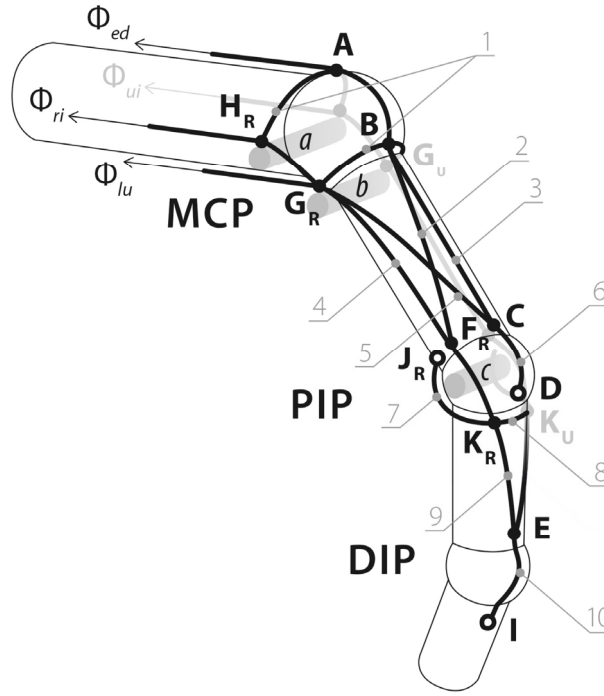


Figure 58. The view of the individual band model of the extensor mechanism. The structures included in the model are denoted by numbers from 1 to 10 and listed in Table 5.

Letters from A to J denoted the main points, among which there were four insertions of the EM into the bones and 12 nodal points of bands disjoining or junction (unfiled points and filed points in Figure 58, respectively). For the points lying outside the medial plane the index *u* denotes ulnar, *r* denotes radial.

Due to a lack of published data, the insertion points *J_u*, *D*, and *J_r* were fixed at the middle phalanx surface, respectively at 0.9, 0.2 and 0.9 of the segment length. Point *I* was fixed at the distal phalanx surface at 0.1 of the segment length.

The smallest building block of this model is a band, which is an element of the model, lying between two main points. It is represented by a sequence of points, connected by springs. The stiffness of each spring, connecting two sequential points in one band was calculated as a function of the band's elasticity modulus, cross-area, and the number of springs in the series forming the band. This number is inversely proportional to the linear density of the points forming the element. Therefore, the stiffness of the springs forming the band *i* was:

$$k_i = A_i \cdot E_i \cdot v_i, \quad (58)$$

where

A is an EM band cross-sectional area, *E_i* –elasticity modulus, *v_i* – linear density of the points forming the band.

The linear density of the points in a band is a quantity inverse to a distance between two points in a band when no load is applied. A length of the band can be adjusted by defining the number of points in a band and their linear density. Increasing the density of the points leads to higher precision but also increases the simulation time. In absence of the precise skeleton model, we chose the density of each band in the range from 0.5 to 1.5 points by millimeter. Hence, to adjust the length of the band we adjusted the linear density of the points in this rang, and if needed, changed the number of the points in a band.

The EM parameters, including length, cross-sectional area and the modulus of elasticity of the bands were obtained from literature and are detailed in Table 1.

Table 5. The elements of the extensor mechanism, included into the model

Element number	Extensor mechanism element name	Abbreviation	Length (mm)	Cross-sectional area (mm ²)	Modulus of elasticity (MPa)
1	Proximal interosseous hood	-	18.4±2.5 ^a	1.11±0.62 ^c	64.87±29.30 ^d
	Distal interosseous hood	-	18.5±3.0 ^a		
2	Extensor lateral band	<i>el</i>	N/A	N/A	N/A
3	Extensor medial band	-	33.6±4.4 ^a	1.50±0.63 ^c	114.03±61.34 ^d
4	Interosseous lateral band	-	37.1±2.6 ^a	N/A	N/A
5	Interosseous medial band	<i>im</i>	36.2±1.9 ^a	N/A	N/A
6	Medial extensor tendon	<i>me</i>	11.2±1.8 ^a	1.13±0.58 ^c	125.31±62.06 ^d
7	Oblique retinacular ligament	-	15 ^e	N/A	N/A
8	Triangular ligament	-	5.4±1.1 ^b	N/A	N/A
9	Radial and ulnar lateral band	<i>rb</i> and <i>ub</i>	18.4±4.3 ^a	1.13±0.74 ^c	157.02±138.37 ^d
10	Terminal extensor tendon	<i>te</i>	10.0±2.6 ^b	0.90±0.34 ^c	96.97±51.29 ^d

^a(Garcia-Elias et al., 1991);

^b(Schweitzer and Rayan, 2004);

^cEstimation for circular cross-section based on tendon thickness (Qian et al., 2014);

^d(Qian et al., 2014);

^e(Shrewsbury and Johnson, 1977);

N/A denotes non-available data

1.2.2. Membrane model

The developed environment allows representing of the extensor mechanism by principal building blocks: strings (shown with black in Figure 59), membranes (cyan) and fiber layers (red and blue). Each building block consist of a sequence of points, pairwise connected by elastic elements with a linear law.

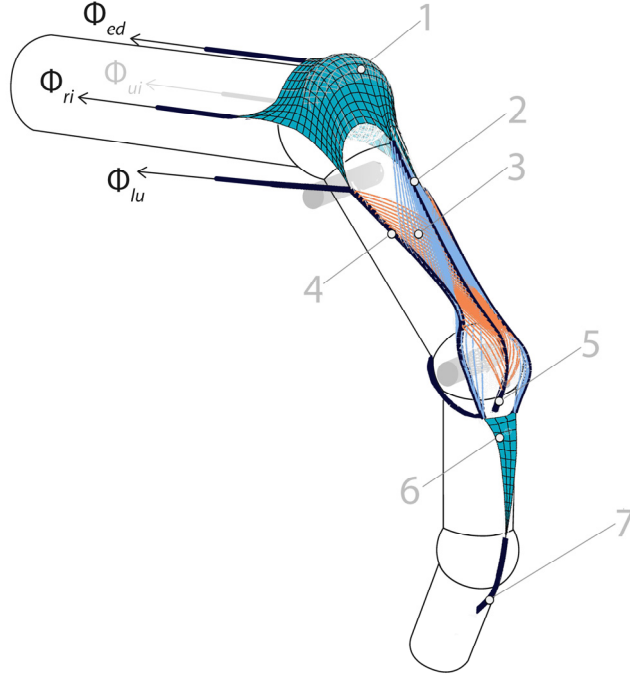


Figure 59. The view of the membrane model of the extensor mechanism. The strings are shown in black, membranes in cyan and fiber layers in red and blue. 1 – the extensor hood, 2 – extensor medial band, 3 – intercrossing fibers, 4 – interosseous lateral band, 5 – medial extensor tendon, 6 – triangular ligament, 7 – terminal extensor tendon.

1.3. Force distribution coefficient estimation

The equation (8) contains 11 coefficients which determine the force distribution among the bands of the EM, acquired experimentally for the extended posture. Their values depend on the properties of the tendons and the angles between them. The distribution of the forces among the tendons of the proposed model with any topology can be described in the same way:

$$\begin{cases} \tilde{F}_{te} = C_1 F_{ub} + C_2 F_{rb} \\ \tilde{F}_{rb} = C_3 \Phi_{ed} + C_4 \Phi_{ri} + C_5 \Phi_{lu} \\ \tilde{F}_{ub} = C_6 \Phi_{ui} + C_7 \Phi_{ed} \\ \tilde{F}_{me} = C_8 \Phi_{ui} + C_9 \Phi_{ed} + C_{10} \Phi_{ri} + C_{11} \Phi_{lu} \end{cases}, \quad (59)$$

where \tilde{F} are the internal forces in the model tendons, Φ are the muscle forces applied to a model.

A tilde of the tendon forces \tilde{F} is used to emphasize that they are estimated to be accurate within a certain degree of error.

The coefficients of (59) will be denoted as the vector $\mathbf{C} = [C_1 \dots C_{11}]^T$ and the corresponding coefficients of the equation system (8) will similarly be denoted as the vector $\hat{\mathbf{C}} = [1.00 \dots 0.33]^T$.

As there are more unknown coefficients than equations in (59), different muscle force sets should be applied to the model to determine all unknowns. We used the assumption that the model is linear for small variations in the muscle forces. Four different muscle force sets were applied to the model, which corresponds to the number of muscles. The four force sets were created on the base of the initial muscle force set Φ by sequentially adding a 0.5 N increment to the force of each muscle. Thus, to find the coefficients \mathbf{C}^* , the equation (60) was solved:

$$\mathbf{A}^* = \mathbf{B} \mathbf{C}^*, \quad (60)$$

where

$$\mathbf{A} = \begin{pmatrix} \mathbf{A}_1 \\ \mathbf{A}_2 \\ \mathbf{A}_3 \\ \mathbf{A}_4 \end{pmatrix}, \mathbf{B} = \begin{pmatrix} \mathbf{B}_1 & \mathbf{0} & \mathbf{0} & \mathbf{0} \\ \mathbf{0} & \mathbf{B}_2 & \mathbf{0} & \mathbf{0} \\ \mathbf{0} & \mathbf{0} & \mathbf{B}_3 & \mathbf{0} \\ \mathbf{0} & \mathbf{0} & \mathbf{0} & \mathbf{B}_4 \end{pmatrix}, \mathbf{C} = \begin{pmatrix} C_1 \\ \vdots \\ \vdots \\ C_{11} \end{pmatrix}. \quad (61)$$

The diagonal elements of the matrix \mathbf{B} are the matrices $\mathbf{B}_1 \dots \mathbf{B}_4$, corresponding to the forces from right parts of the four equations (59) and $\mathbf{0}$ are zero matrices. The matrix-column \mathbf{A} consists of the matrices $\mathbf{A}_1 \dots \mathbf{A}_4$ of the forces from the left parts of (59). For example, the coefficients $C_8 \dots C_{11}$ from the fourth line of (59) depends on matrices \mathbf{A}_4 and \mathbf{B}_4 :

$$\mathbf{A}_4 = \begin{pmatrix} \tilde{F}_{me1} \\ \tilde{F}_{me2} \\ \tilde{F}_{me3} \\ \tilde{F}_{me4} \end{pmatrix}, \mathbf{B}_4 = \begin{pmatrix} \Phi_{ui} + \Delta\Phi_{ui} & \Phi_{ed} & \Phi_{ri} & \Phi_{lu} \\ \Phi_{ui} & \Phi_{ed} + \Delta\Phi_{ed} & \Phi_{ri} & \Phi_{lu} \\ \Phi_{ui} & \Phi_{ed} & \Phi_{ri} + \Delta\Phi_{ri} & \Phi_{lu} \\ \Phi_{ui} & \Phi_{ed} & \Phi_{ri} & \Phi_{lu} + \Delta\Phi_{ri} \end{pmatrix} \quad (62)$$

As the forces in model tendons are estimated to be accurate within a certain degree of error, solving (60) directly can lead to improper results. To overcome this problem, the solution of (60) was calculated by Tikhonov regularization:

$$\mathbf{C}^* = \arg \min_{\mathbf{C}} \left(\|\mathbf{B}\mathbf{C} - \mathbf{A}\|^2 + \alpha \|\mathbf{C}\|^2 \right) \quad (63)$$

where a regularization parameter α was set to 0.01.

This procedure allows one to find \mathbf{C}^* which minimizes the squared norm of the difference between \mathbf{A} and \mathbf{BC} . The anomalous values were avoided by adding the weighted squared norm of \mathbf{C}^* to a minimized term.

1.4. Tendon moment and fingertip wrench estimation

1.4.1. Tendon moment estimation

To calculate the moments about the joint angles, the contact forces were calculated. The extensor mechanism was replaced by the contact forces, produced by the points of the extensor mechanism on bones.

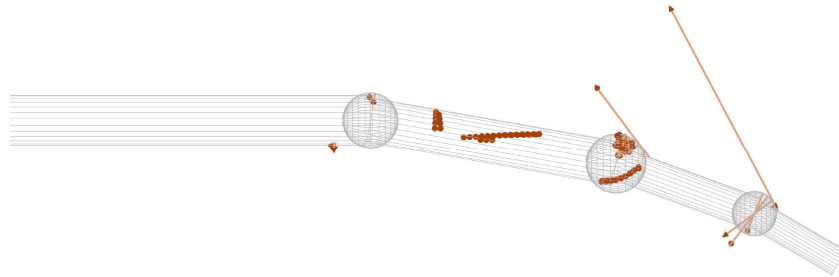


Figure 60. The contact forces produced by the points of the extensor mechanism on bones.

Finally, the moments $\mathbf{m}(\mathbf{q})$ about each joint axes were calculated:

$$\mathbf{m}(\mathbf{q}) = \begin{bmatrix} M_y^{MCP} & M_x^{MCP} & M_x^{PIP} & M_x^{DIP} \end{bmatrix}^T$$

1.4.2. Fingertip wrench estimation

The Jacobian $\mathbf{J}(\mathbf{q})$ of the skeleton model, defined by the bone lengths, was calculated.

The finger Jacobian was used to calculate the fingertip wrench vector \mathbf{w} , i.e. the vector containing the components of the force and the moment, produced by a fingertip.

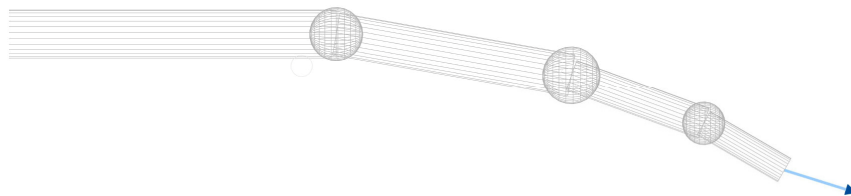


Figure 61. The output force, produced by fingertip.

Chapter 2. Extensor mechanism simulations

In current chapter, we simulated the EM using both topologies, individual bend and membrane, to study how the force distribution among the tendons depends on model parameters, posture and applied muscle forces.

2.1. Study of the parameter influence

Extensor mechanism model can have a high number of parameters. For a chosen topology, the parameters are the length of the elastic elements, connecting two points, and their stiffnesses. However, the extensor mechanism model may contain a very high number of points, therefore to reduce the number of parameters, the lengths and stiffness of individual building blocks (bands, membranes) may be used as the parameters. The purpose of this section was to analyze how the EM model behavior depends on model parameters and propose a parametrization algorithm to make the force transition among the modeled EM bands fit the experimental data.

2.1.1. Significance of the parameter choice

Variation of parameters can considerably change the model behavior. Figure 62 gives an example how the variation of the parameters switches the individual-band model from a normal state (a) to pathological ones (b-e). Figure 62a shows a model with initial set of parameters which corresponds to a normal finger. Figure 62b shows the extensor mechanism with increased length of the medial extensor tendon and the triangular ligament. This state of extensor mechanism leads to the boutonniere deformity (Figure 62d). Figure 62c shows the extensor mechanism with increased length of the terminal extensor tendon and the oblique retinacular ligaments. This state of extensor mechanism leads to the swan-neck deformity (Figure 62e).

Images b – c show changes in the extensor mechanism form with the change of its parameters, while all joint angles are fixed at 10. Approximate bone configurations, which correspond to each pathological state, are shown below.

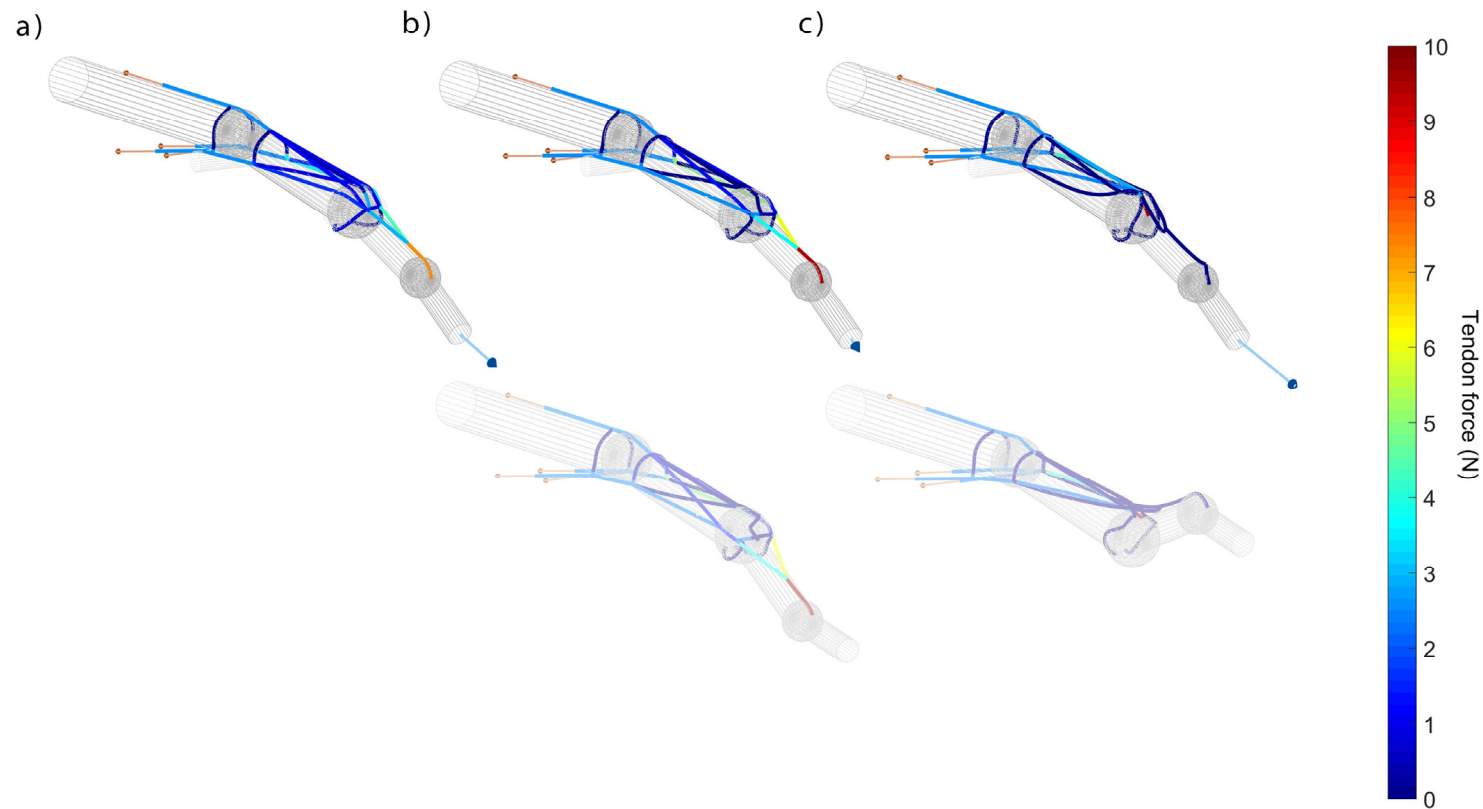


Figure 62. The influence of the extensor mechanism model parameters on its geometry and force distribution. a) parameters corresponding to a normal state; b) length of the medial extensor tendon and triangular ligament. Deformation of the posture, that may be produced by a parameter set b (boutonniere deformity) is shown below; c) increased lengths of the terminal tendon and oblique retinacula ligament. Deformation of the posture that may be produced by a parameter set c (swan-neck deformity) is shown below.

The variation of parameters change the force distribution among the extensor mechanism. Figure 64 shows the force distribution coefficients for an individual band model with three parameter sets from the Figure 62 a,b,c. The force distribution coefficients were calculated with equation (63).

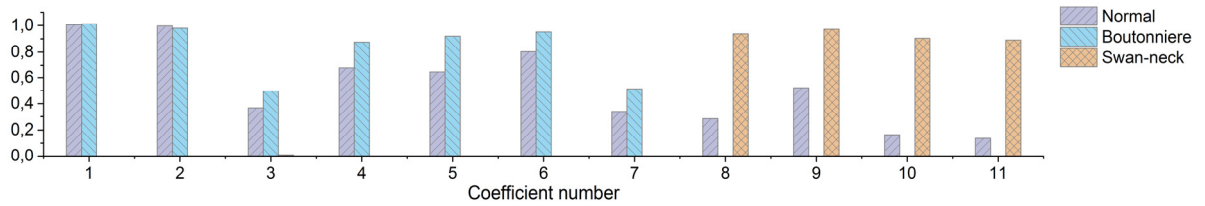


Figure 63. The force distribution coefficients calculated for three individual-band model (normal, swan-neck, boutonniere)

It may be seen from Figure 7 that at the normal state the forces are transmitted by all bands. However, in case of boutonniere deformity, the forces are transmitted only to distal part of the EM (coefficients 1-7), and in case of the swan-neck deformity the forces are transmitted only to the proximal part of the EM (coefficients 8-11).

The changes of the force distribution makes the moments in joints, produced by the tendons, also vary. The moments across the joint axes, created by the extensor mechanism model with three sets of parameters from the figure the Figure 62 a,b,c is shown in Figure 64a.

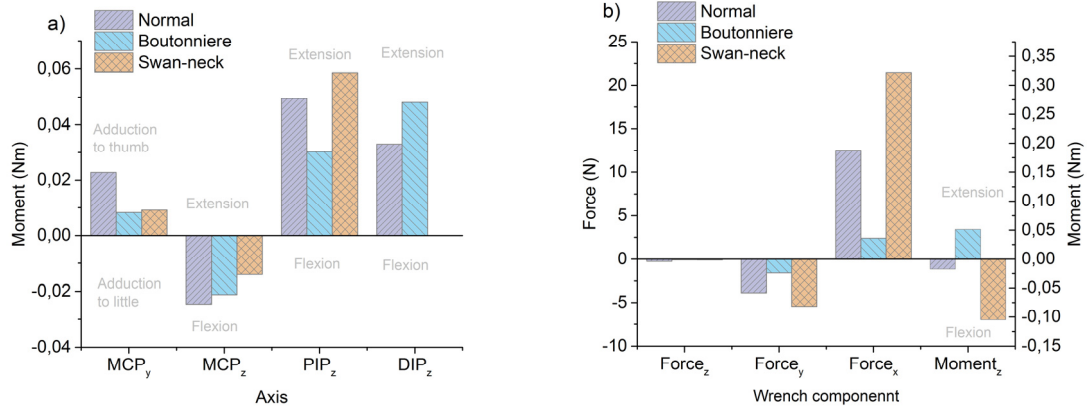


Figure 64.a) the moments in joints produced by the EM with different parameter sets; b) A fingertip wrench produced by the EM with different parameter sets.

It may be seen how the changes in EM parameters changes the moments in joints. For the EM with the normal set of parameters the following moments may be observed: flexion across x-axis of MCP joint and extension across the x-axes of PIP and DIP joints. For the EM corresponding to boutonniere deformity the directions of the moments are the same, but the moment of extension in PIP joint is higher. Finally, for the EM corresponding to swan-neck deformity there is no moment in DIP joint.

The corresponding fingertip wrenches for these three cases (Figure 62 a,b,c) are shown in Figure 64b. It may be seen from the figure that the output force significantly differs according to the model parameter, i.e. the lengths of medial and terminal extensor tendon.

Another important part of the extensor mechanism are the intercrossing bands: extensor lateral band l_{el} and interosseous medial band l_{im} (2 and 5 in Figure 58 or 7 in Figure 59). These bands are situated on both ulnar and radial sides of the EM and have a strong influence on the EM configuration (R. Schultz et al., 1981). Below we show how variation of the length of the intercrossing bands influence the individual band model of and membrane model of the EM.

2.1.2. Individual band model

We firstly studied how the length of two intercrossing bands, extensor lateral band l_{el} and interosseous medial band l_{im} change the model behavior. We assumed that corresponding bands from ulnar and radial sides have the same length. We studied the influence of parameters for the finger with the angles in all joints equal to 10° and all muscle forces equal to 3N.

Figure 65 shows how the variation of the parameters l_{im} and l_{el} changes the force distribution among the median and terminal tendon extensors.

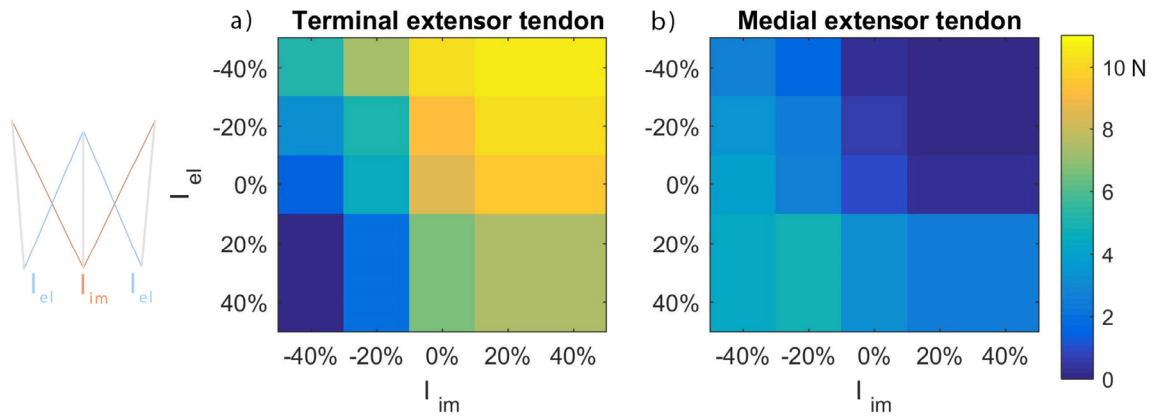


Figure 65. The influence of the lengths of the intercrossing bands on force transmitted to the terminal tendon extensor (a) and medial tendon extensor (b). Individual band model

It may be seen from Figure 9 that all muscle forces are transmitted to terminal tendon when the im -band is lengthened and el -band is shortened. Vice versa, when the im -band is shortened and el -band is lengthened, the force is transmitted to medial extensor. When both im - and el -band are lengthened, the extensor mechanism becomes trivial: the force from the EDC is transmitted only to medial extensor band and the force of the interosseous and lumbrical muscle are transmitted to the terminal extensor tendon without any force transition by intercrossing bands.

Parametrization

It is important to parametrize the EM model to make the force distribution in the model fit given experimental data. We performed a parametrization of the individual-band EM model to make the coefficients \mathbf{C}^* , showing the force transmission among the model bands fit the coefficients $\hat{\mathbf{C}}$, reported by (Chao et al., 1978), which appear in the equation system (8). The lengths of two intercrossing bands,

extensor lateral band el and interosseous medial band im , were used as the identified parameters, denoted by a vector $\mathbf{l} = [l_{el} \ l_{im}]^T$.

The parametrization was performed for the finger in extension (MCP=0°, PIP=0°, DIP=0° of flexion) as it is the only posture for which the coefficients \mathbf{C} were experimentally defined. The muscle forces applied to the model $\Phi = [1.96N \ 4.66N \ 2.45N \ 1.47N]^T$ were taken from (Hurlbut and Adams, 1995).

The root-mean-square error between \mathbf{C}^* and $\hat{\mathbf{C}}$ was used as a cost-function $J(\mathbf{l})$,

$$J(\mathbf{l}) = \sqrt{\frac{\sum_{q=1}^Q (\hat{C}_q(\mathbf{l}) - C_q^*(\mathbf{l}))^2}{Q}}, \quad (64)$$

where Q denotes the number of coefficients ($Q=11$)

The Nelder-Mead algorithm (`fminsearch` function in Matlab R2012b, MathWorks, Natwick, MA) was used to solve the unconstrained problem of $J(\mathbf{l})$ minimization.

$$\mathbf{l}_{opt} = \arg \min_{\mathbf{l}} J(\mathbf{l}), \quad (65)$$

The starting point of the algorithm corresponded to such EM configuration, in which all lateral and medial bands were tight (2 and 3, 4 and 5 in Figure 58).

The identified tendon lengths for l_{el} and l_{im} are given in Table 6.

Table 6. The parametrization results

Parameter	Value
Length of extensor lateral band l_{el} (mm)	37.8
Length of interosseous medial band l_{im} (mm)	32.6
Cost-function J	0.17

The identified value of l_{im} is 10% lower than the value defined by anatomical survey (Table 1). No comparison was possible for l_{el} as no published data exists. The identified parameters results in a very good fit for C_1 , C_2 , C_6 , and C_8 . Coefficients C_1 and C_2 represent the fraction of the force in ub and rb transmitted to te -tendon. C_6 and C_8 represent the fraction of the ui -muscle transmitted to ub and me -tendon. The major difference concerns coefficients C_5 , and C_{11} , related to the fraction of lu -muscle transmitted to rb and me -tendon.

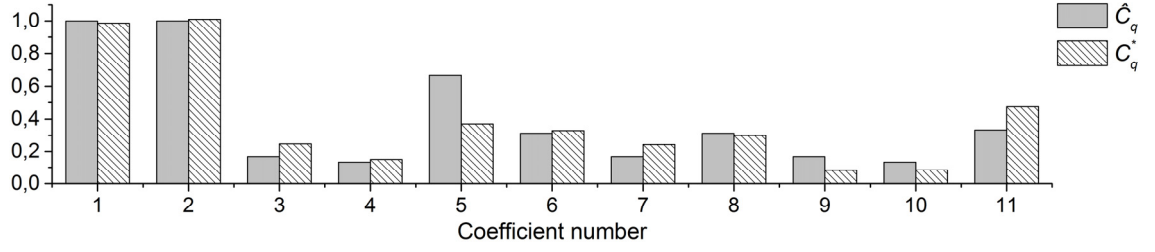


Figure 66 The experimentally defined coefficients \hat{C}_q from the equation shown in comparison with the corresponding model-characterizing coefficients C_q^* . The former values are depicted by filed bars, the latter values are depicted by the hatched bars.

Sensitivity analysis

We focused on the sensitivity of the coefficients C_q^* , characterizing the parametrized model to variation of the model parameters \mathbf{l} in the neighborhood of the identified parameter values \mathbf{l}_{opt} . The sensitivity of the model with the identified parameters was calculated for the same conditions as the parametrization (muscle forces, extension posture).

The sensitivity indices $S1(C_q^*)_j$ were calculated as the partial derivative of the model coefficients C_q^* values with respect to the parameter values. These indices show how the force distribution among tendons is sensitive to the variation of the tendons lengths l_{el} and l_{im} :

$$S1(C_q^*)_j = \frac{C_q^*(l_1, \dots, l_j + \Delta l_j, \dots, l_n, \Phi) - C_q^*(l_1, \dots, l_j - \Delta l_j, \dots, l_n, \Phi)}{2\Delta l_j}, \quad (66)$$

Where Δp_j was 0.1 mm.

The positive value of a sensitivity index $S1(C_q^*)_j$ indicates that q -th coefficient increases when the length of the j -th band increases.

Figure 67 represents the sensitivity indices $S1(C_q^*)_j$, which show how the values of C^* change with respect to tendon length variation. It can be seen that C_6^* , C_7^* , and C_{11}^* are less sensitive to parameter variation whereas the most significant variations were observed for C_3^* and C_5^* .

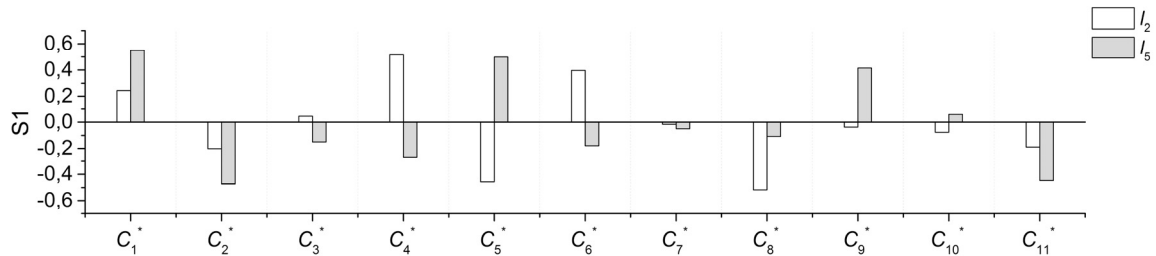


Figure 67. The sensitivity indices, $S1$, showing the sensitivity of model-characterizing coefficients C_q^* to variation of tendon lengths

2.1.3. Membrane model

We also studied how the parameters of the model influence on the output force of the membrane model. The vector of parameters $\mathbf{l} = [l_{el} \ l_{im}]$ was used to define the length of the four lowest intercrossing bands (Figure 68). The length of all other intercrossing bands are proportional to the length of these bands. Hence, the vector \mathbf{l} controls the form of two layers of intercrossing fibers. We studied the influence of parameters for the finger with the angles in all joints equal to 10° and all muscle forces equal to 3N.

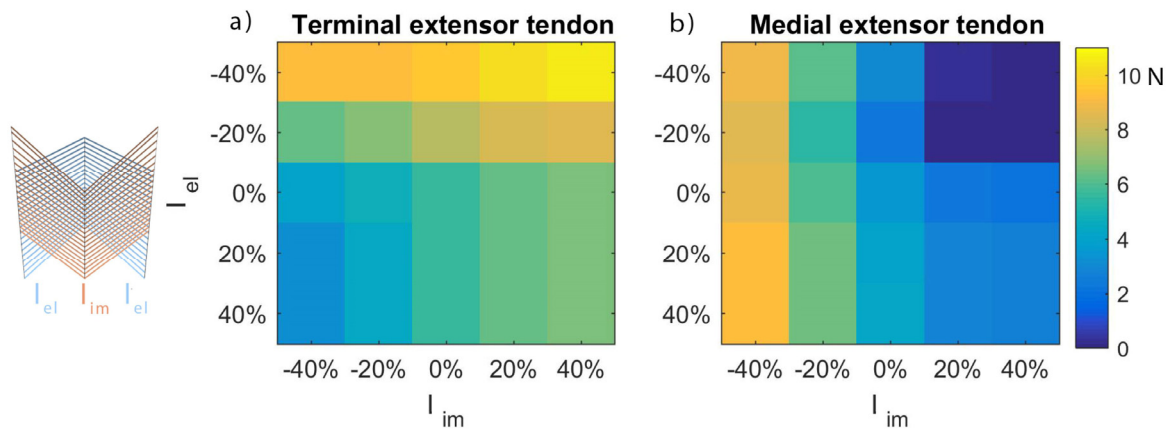


Figure 68. The influence of the lengths of the intercrossing fibers on force transmitted to the terminal tendon extensor (a) and medial tendon extensor (b). Membrane model

It may be seen that the force transition in the membrane model changes the same way as in the individual band model (Figure 65).

In this section, it was shown that the extensor mechanism is a complex structure. The model of the extensor mechanism contains high number of parameters, which are the stiffnesses of the springs between the points, representing the EM and distances between them in unloaded state. More the model is complicated, more unknown parameters it has. To reduce the number of unknown parameters, one can control the parameters of individual blocks, *i.e.* bands and membranes.

The choice of parameters is crucial as it defines will the models behavior. To simulate ether the normal EM or the pathological state, the parametrization procedure must be performed. The parametrization procedure allows one to define the model parameters, which makes the model behavior fit the experimental data. We proposed the parametrization algorithm, which fits the force transmission among the modeled EM bands to experimental data.

Nevertheless, the other parametrization techniques may be proposed, for example, the data about the length between the bands may be also included into parametrization procedure.

It should be noticed that we studied the influence of the parameters of the model and performed a parametrization of the model for a given posture. The next section is devoted to analyze of the influence of the posture on the EM model.

2.2. Study of the postural influence

When the posture changes, the geometry of the extensor mechanism elements over the bones also changes, which leads to variation of the force distribution among the extensor mechanism and changes moments in joints and fingertip wrench. The coefficients describing the force transmission reported by (Chao et al., 1978), which appear in the equation system (8) does not take into account the EM deformation with posture. The purpose of this section was to study how the behavior of the simulated EM depends on a finger posture.

2.2.1. Individual band model

In this section, we analyze how the finger posture influences the geometry of the individual band EM model and force transmission in it. We also study, how the moments in joints and the output fingertip force change with the posture.

Geometrical changes

The parameter set, identified in previous section was used to model three finger postures observed in (Garcia-Elias et al., 1991; Hurlbut and Adams, 1995): full extension, mid-flexion and full flexion. The simulation results are shown in Figure 69.

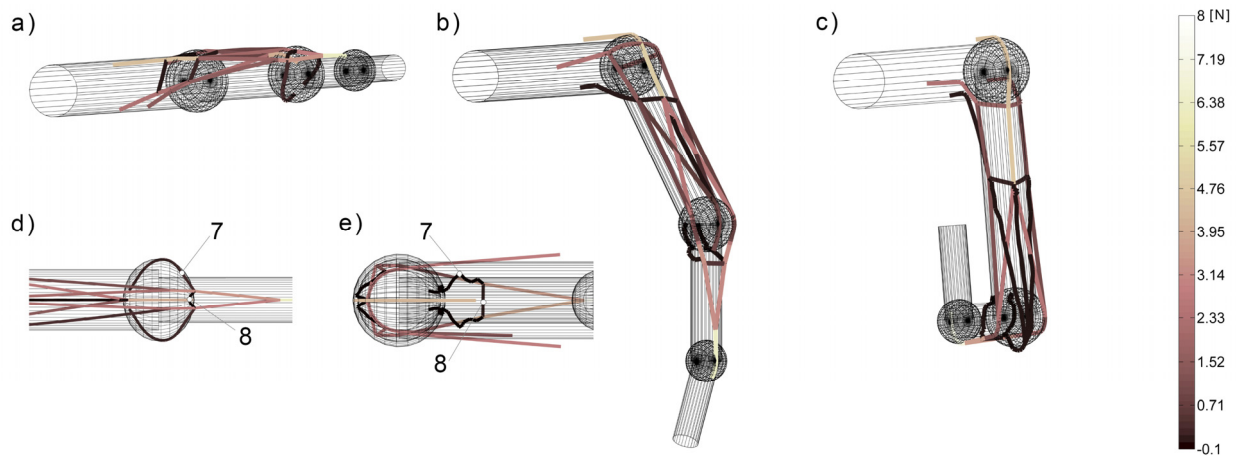


Figure 69. The extensor mechanism simulations using individual band model for three finger postures. Left to right: (a) full extension [$DIP = 0^\circ$; $PIP = 0^\circ$; $MCP = 0^\circ$], (b) mid-flexion [$DIP = 30^\circ$; $PIP = 45^\circ$; $MCP = 45^\circ$], (c) full flexion [$DIP = 90^\circ$; $PIP = 90^\circ$; $MCP = 90^\circ$]; the scaled-up retinacular and triangular ligaments (d) in extension and (e) flexion.

The changes of the EM configuration with flexion can be seen from Figure 69. The extensor hood shifts distally while *ub* and *rb* tendons shift laterally. The retention apparatus is also affected by changes: the retinacular ligament relaxes and triangular ligament becomes tight with flexion.

The evolution of angle F_uAC and F_uG_uC , shows the lateral shift of the *ub* and *rb* tendons (Figure 70). The evolution of this angle was comparable to reported values obtained in (Garcia-Elias et al., 1991).

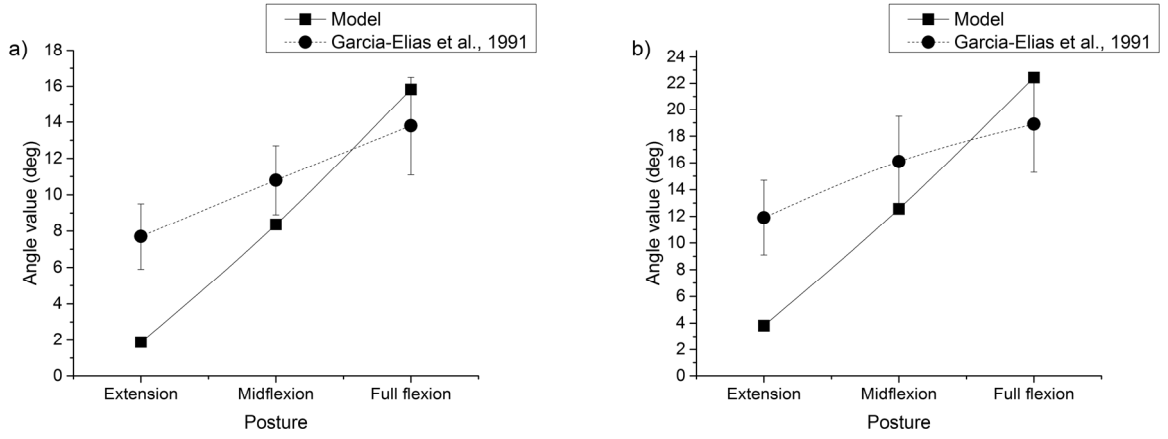


Figure 70. Model predicted values of the angle F_uAC (a) and F_uGuC (b) compared with the data reported by Garcia-Elias et al. (1991)

Both angles increase with flexion in the model and in experimental data. Angle F_uAC increases from 1.9° to 15.8° for the model and from 7.7° to 13.8° for the experimental data. Angle F_uGuC increases from 3.8° to 22.4° for the model and from 11.9° to 18.9° for the experimental data. For both angles, the major difference concerns the value in the extended posture, which is four times lower in the simulated data.

Changes of the force transmission

The changes of the extensor mechanism geometry with posture makes vary the force transmission among the tendons. The extensor mechanism is principally attached to bones by two tendons: medial extensor tendon and terminal extensor tendon. All bands of the extensor mechanism are coupled either with the former or latter tendon. Hence, the change of the force distribution among the extensor mechanism bands changes the ratio between the forces in these tendons.

To characterize this effect the feasible tendon force set (FTFS) was calculated. We will define a feasible tendon force set as a set of all possible combinations of the forces in terminal tendon extensor te and medial tendon extensor me that the extensor mechanism can produce at the given activation level. To find a feasible tendon force set we applied all possible combinations of input muscle forces to the EM:

$$\Phi = [0 \ 0 \ 0 \ 0]^T; [F \ 0 \ 0 \ 0]^T; [0 \ F \ 0 \ 0]^T; \dots [0 \ F \ 0 \ 0]^T. \quad (67)$$

The value of the force of one muscle F was set to 3 N.

Each applied muscle force combination corresponds to a combination of the forces in the te and me bands, or to a point in a te -force vs. me -force plane. A feasible tendon force set was calculated as a convex hull of the points in a tendon force plane.

Figure 71 shows a feasible tendon force set for three postures:

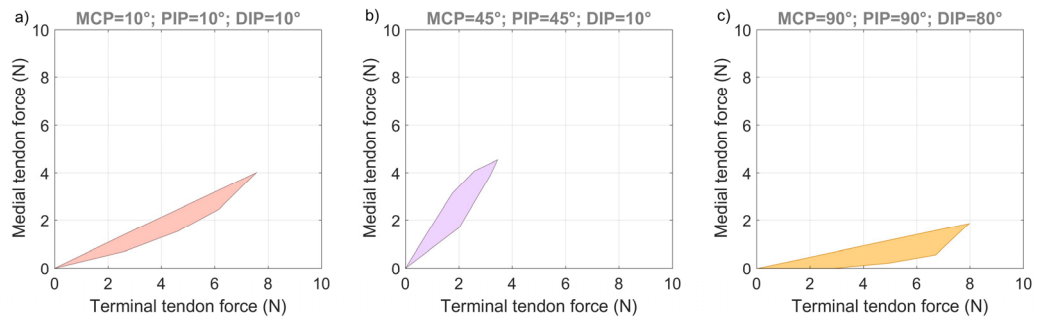


Figure 71. The feasible tendon force set produced by a individual band EM model in three postures: (a) extension [DIP = 10°; PIP = 10°; MCP = 10°], (b) mid-flexion [DIP = 10°; PIP = 45°; MCP = 45°], (c) full flexion [DIP = 90°; PIP = 90°; MCP = 90°]

It can be seen from the figure that in the individual band model, the fraction of the muscle force that may be transmitted to the *me*-tendon decreases with flexion. It may be explained by the fact that some bands may become slack with the change of the posture.

Changes of output force with posture

The change of the force distribution among the EM-bands changes the moments, produced by the tendons in joints and, as a result, change the wrench, produced by a fingertip. To characterize how the finger output changes with posture, a feasible force set (FFS) was calculated. An FFS was calculated as a convex hull of all possible fingertip forces, that the fingertip can produced at the given activation level. To find a feasible tendon force set we applied all possible combinations of input muscle forces (67) to the EM, as in case of the feasible tendon force set.

Figure 72 shows changes of the xOy projections of the FFS, produced by the individual band model, with posture.

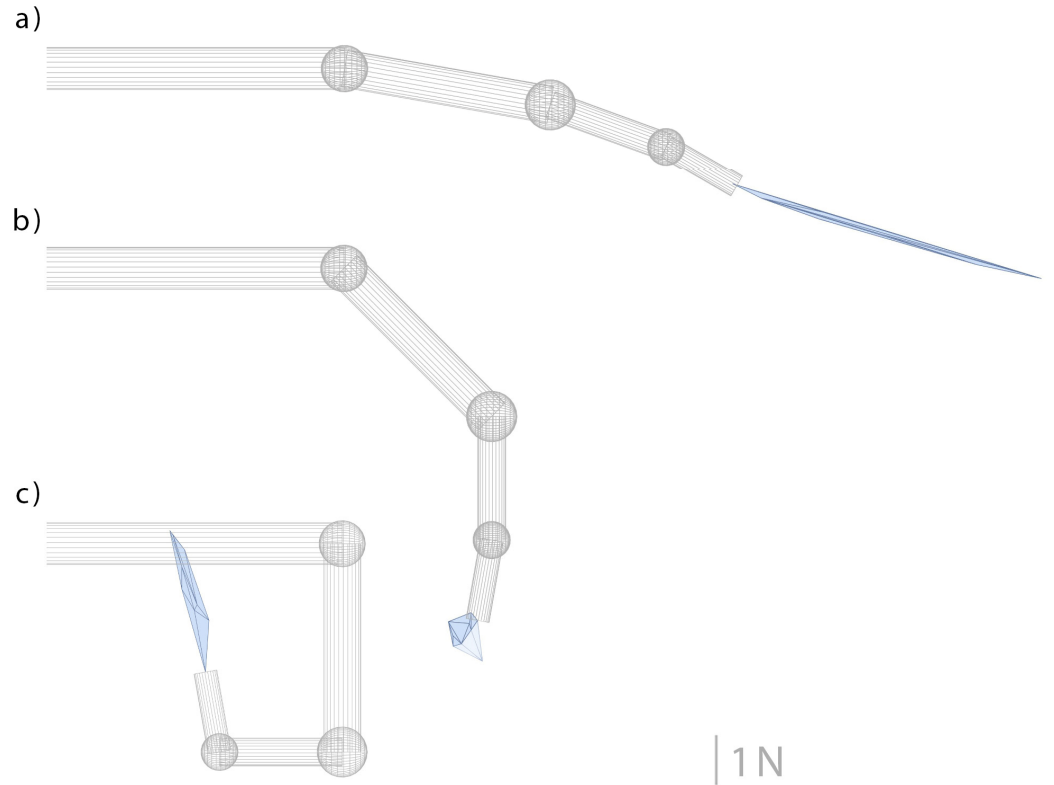


Figure 72. The feasible force set produced by a individual band EM model in three postures: (a) extension [$DIP = 10^\circ$; $PIP = 10^\circ$; $MCP = 10^\circ$], (b) mid-flexion [$DIP = 10^\circ$; $PIP = 45^\circ$; $MCP = 45^\circ$], (c) full flexion [$DIP = 90^\circ$; $PIP = 90^\circ$; $MCP = 90^\circ$]. Projections at xOy plane are shown.

The variation of the FFS form, area and orientation with posture can be seen from the figure.

It should be noticed that the FFS, shown in the Figure 72 are calculated for a set of parameters, identified in previous section. However, the variation of the model parameters can modify the FFS.

2.2.2. Membrane model

We also analyzed how the membrane model deforms with posture.

Geometrical changes

Figure 73 shows the simulated membrane model of the EM. The simulations were performed for the same postures that in the Figure 69.

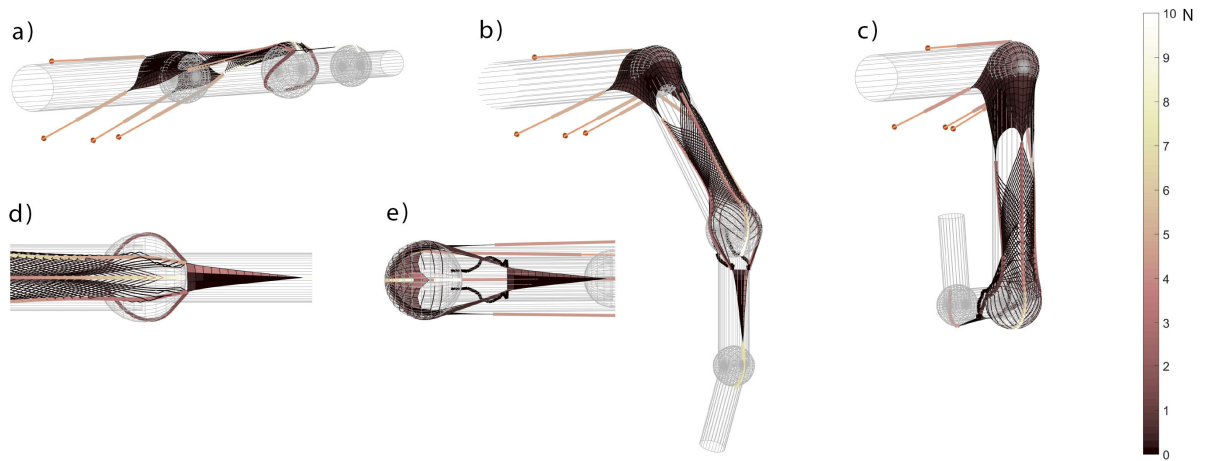


Figure 73. The extensor mechanism simulation using membrane model for three finger postures. Left to right: (a) full extension [DIP = 0°; PIP = 0°; MCP = 0°], (b) mid-flexion [DIP = 30°; PIP = 45°; MCP = 45°], (c) full flexion [DIP = 90°; PIP = 90°; MCP = 90°]; the scaled-up retinacular and triangular ligaments (d) in extension and (e) flexion.

The changes of EM configuration, simulated by membrane are similar with those, simulated by individual-bands model (Figure 69). They consist in distal displacement of the extensor hood, lateral shift of *ub* and *rb* tendons, and relaxation of retinacular ligament.

Changes of the force transmission

To characterize how the force distribution change with posture, feasible tendon force sets were calculated for three postures (Figure 74):

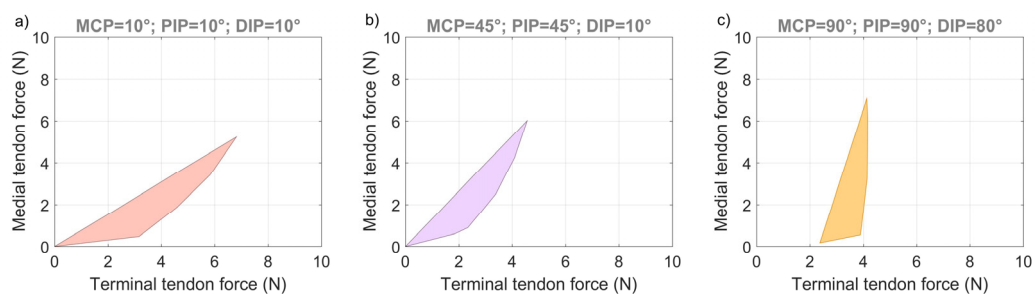


Figure 74. The feasible tendon force set (force in terminal and medial extensor tendon) for different postures

One can notice the difference between the evolution of the FFS created by the membrane and individual band EM. In the individual band model, the *me*-tendon forces decreased with flexion for a given parameter set and activation level. On the contrary, in the membrane model, the *me*-tendon forces increased with flexion. Moreover, the passive forces in *te*-tendon may be observed. These forces were produced by the intercrossing fibers, stretched over the PIP joint.

Changes of output force

The effects of the posture on the FFS, produced by the membrane model was studied. Figure 75 shows the xOy projections of the FFS for three finger postures.

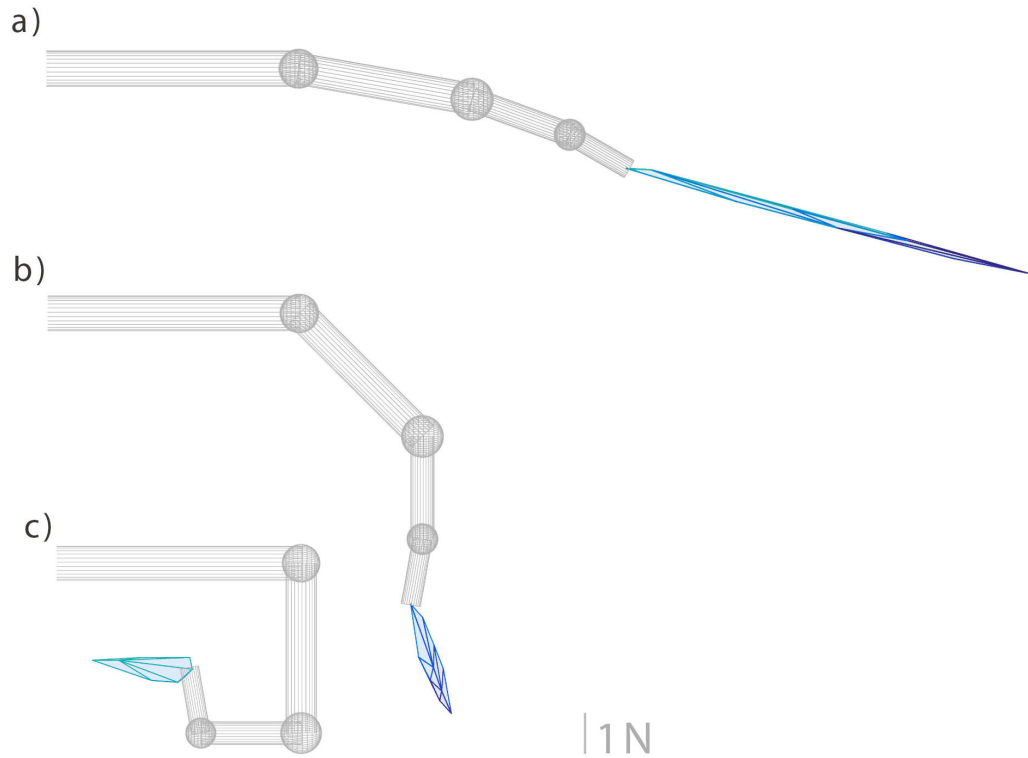


Figure 75. The feasible force set produced by a membrane EM model in three postures: (a) extension [DIP = 10°; PIP = 10°; MCP = 10°], (b) mid-flexion [DIP = 10°; PIP = 45°; MCP = 45°], (c) full flexion [DIP = 90°; PIP = 90°; MCP = 90°]. Projections at xOy plane are shown.

Significant differences between the FFS produced by the individual-band model and the membrane model may be seen in mid-flexion and flexion. These differences concern the direction and the shape of the FFS.

As it was shown above, the extensor mechanism deforms and displaces with the finger movement. As a result, the tension in bands may change with posture for the same input muscle force. Figure 22 compares the force in *te* tendon predicted by an individual band model, membrane model, and experimental data, reported by (Hurlbut and Adams, 1995).

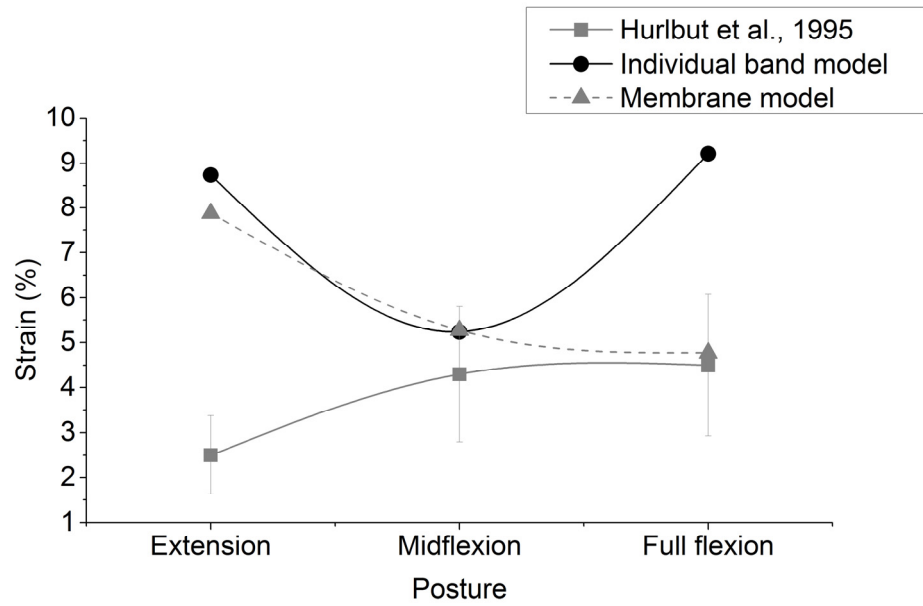


Figure 76. The strain in *te*-tendon predicted by an individual band model (purple) and a membrane model (orange) compared with the experimental data (blue), measured by (Hurlbut and Adams, 1995)

It can be seen from the figure that the force in *te*-tendon changes with flexion. Hence, the experimentally defined coefficients in (8), describing the force distribution in the extensor mechanism bands of the extended finger becomes inaccurate for other postures.

Individual band model has only four intercrossing bands: two extensor lateral bands and two interosseous medial bands (Figure 58) these bands may become slack for some postures. Hence, the individual band model is sensible to posture variation (see Figure 72b).

On the contrary, the membrane model contain of high number of intercrossing fibers, which enables the force transmission by the intercrossing fibers for higher range of postures (see Figure 75). We believe that this better represents a real extensor mechanism as it is conforms to anatomical (R. Schultz et al., 1981) and biomechanical (Leijnse and Spoor, 2012) studies.

In this section. we studied the influence of the parameters of the EM model and the posture on the force transmission among the bands of the model and, as a result, on output fingertip force. The next section analyzes the influence of the muscle activation level on the EM.

2.3. Study of the activation level influence

The extensor mechanism, which mostly consist of collagen fibers and is therefore a stiff structure (Garcia-Elias et al., 1991; Schultz et al., 1981), which tensile properties are nit homogeneous among the bands (Garcia-Elias et al., 1991).

In this section, we studied the influence of the force level on the extensor mechanism models to analyze, how the fore activation level can influence the behavior of the EM models. We compared the individual band and the membrane model.

2.3.1. Individual band model

Geometrical changes

We firstly present the geometrical changes of the individual-band EM model with the muscle activation level. Figure 77 shows the view of the EM model in case when all muscle forces are equal to 3N, 6N, and 9N.

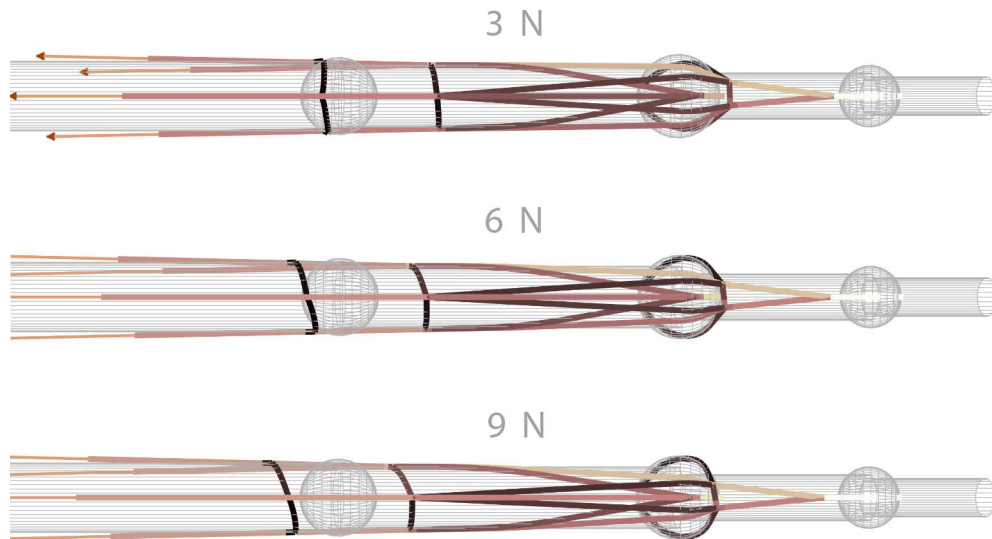


Figure 77 The influence of the force level on the extensor mechaism. Individual band model.

The proximal displacement of the extensor hood may be observed. The EM becomes more narrow at the level of the proximal phalanx p_1 .

Changes of the force transmission

Changes of the extensor mechanism geometry with the force level makes the force distribution among the tendons also vary. To show, how the coefficients, describing the force distribution C_q^* vary with the force level, the model sensitivity to the variation in muscle force was also calculated:

$$S2(C_q^*)_j = \frac{C_q^*(\mathbf{l}_{opt}, \Phi_1, \dots, \Phi_j + \Delta\Phi_j, \dots, \Phi_n) - C_q^*(\mathbf{p}_{opt}, \Phi_1, \dots, \Phi_j - \Delta\Phi_j, \dots, \Phi_n)}{2\Delta\Phi_j}, \quad (68)$$

Where $\Delta\Phi_j$ was 0.5 N.

The positive value of a sensitivity index $S2(C_q^*)_l$ indicates that q -th coefficient increases when the force of j -th muscle increases. Figure 78 represents the sensitivity indices $S2(C_q^*)_j$, which show how the values of C^* change with respect to muscle force variation.

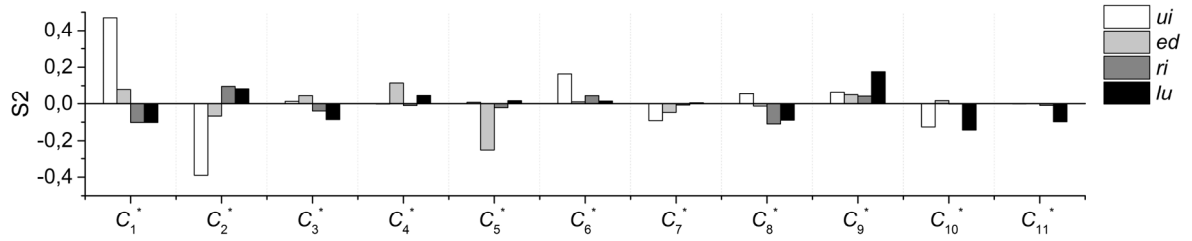


Figure 78. The sensitivity indices $S2$, showing the sensitivity of model-characterizing coefficients C_q^* to variation of muscle force values.

We also studied how the feasible tendon force set, produced by the individual band model (Figure 71) vary with posture. Figure 79 shows the feasible tendon force set at two activation levels: 3 N and 6 N on each muscle.

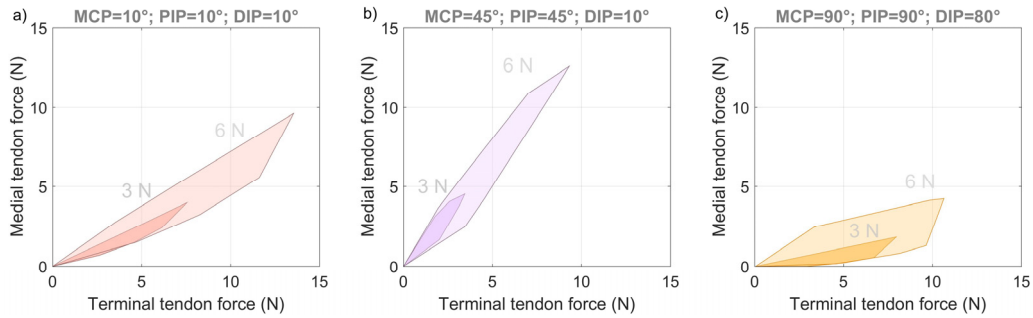


Figure 79. The feasible tendon force sets for different postures at different force levels.

It may be seen from the figure that the area of the feasible tendon force set increases with the activation level with slight variation of the form.

Changes of the output force

The changes in the FFS with the muscle activation level was also calculated. Figure 80 shows how the xOy projection of the FFS produced by the individual band model (Figure 72) vary with posture.

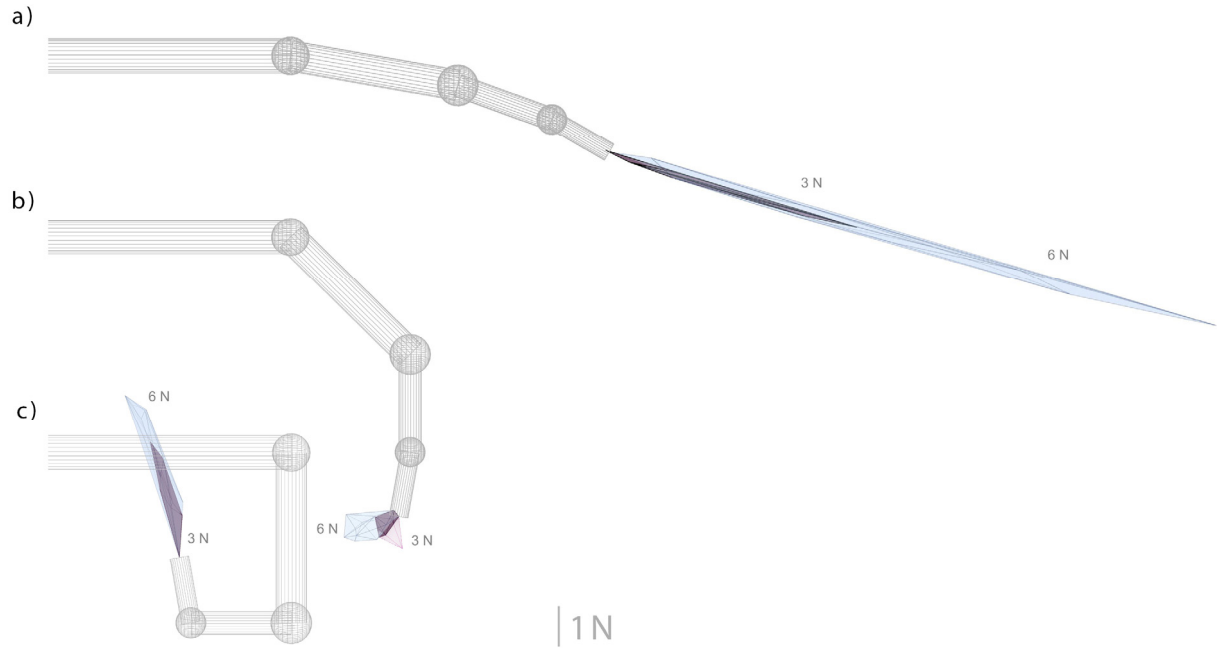


Figure 80. The FFS produced by aEM model in three postures: (a) extension, (b) mid-flexion (c) full flexion. The FFSs related to low activation force level is shown in purple, the FFSs, related to high activation level are shown in blue.

It may be seen from the figure, that the main changes concern only the FFS area. The shape of the FFS may also slightly change (especially in b).

2.3.2. Membrane model

As for the individual band model, we firstly present the geometrical changes of the membrane EM model with the muscle activation level.

Geometrical changes

Figure 81 shows the view of the EM model in case when all muscle forces are equal to 3N; 6N; 9N.

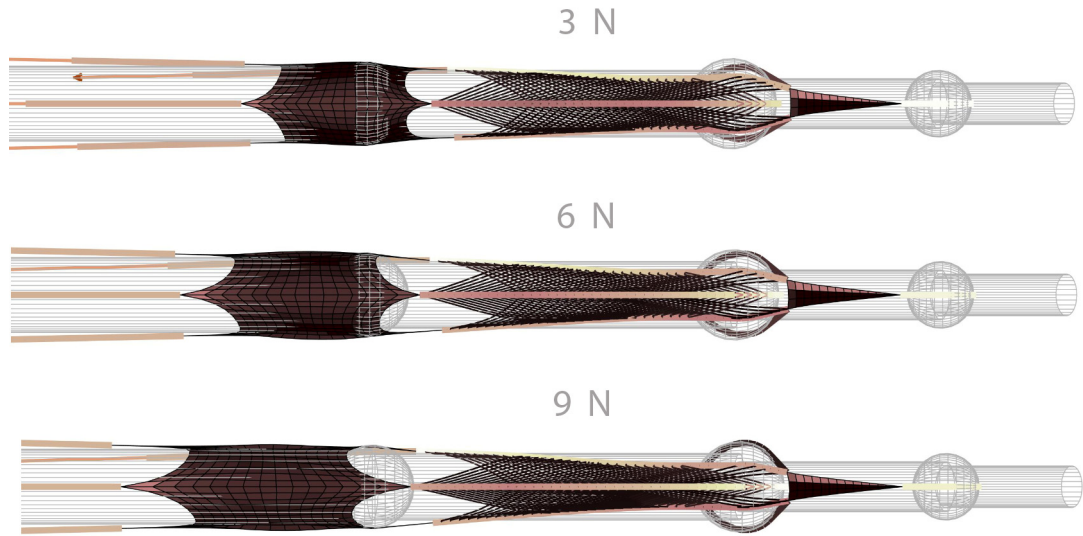


Figure 81. The influence of the force level on the extensor mechanism geometry using membrane model

As for the individual band model, the proximal displacement of the extensor hood may be observed.

Changes of the force transmission

We studied how the feasible tendon force set (Figure 74) vary with posture. Figure 82 shows the feasible tendon force set at two activation levels: 3 N and 6 N on each muscle.

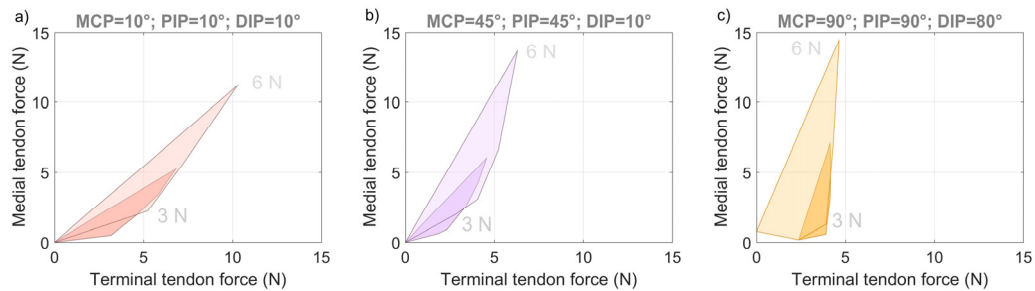


Figure 82, The feasible tendon force sets for different postures at different force levels.

As in case of the individual band model, the main changes concern the increase of the feasible tendon force set area with muscle activation level.

Changes of the output force

The xOy projections FFS for high and low activation level are shown in Figure 83 for extension (a), mid-flexion (b) and flexion (c). To facilitate the comparison of the FFS for two activation levels, each FFSs was normalized by the modulus of the maximal force in it.

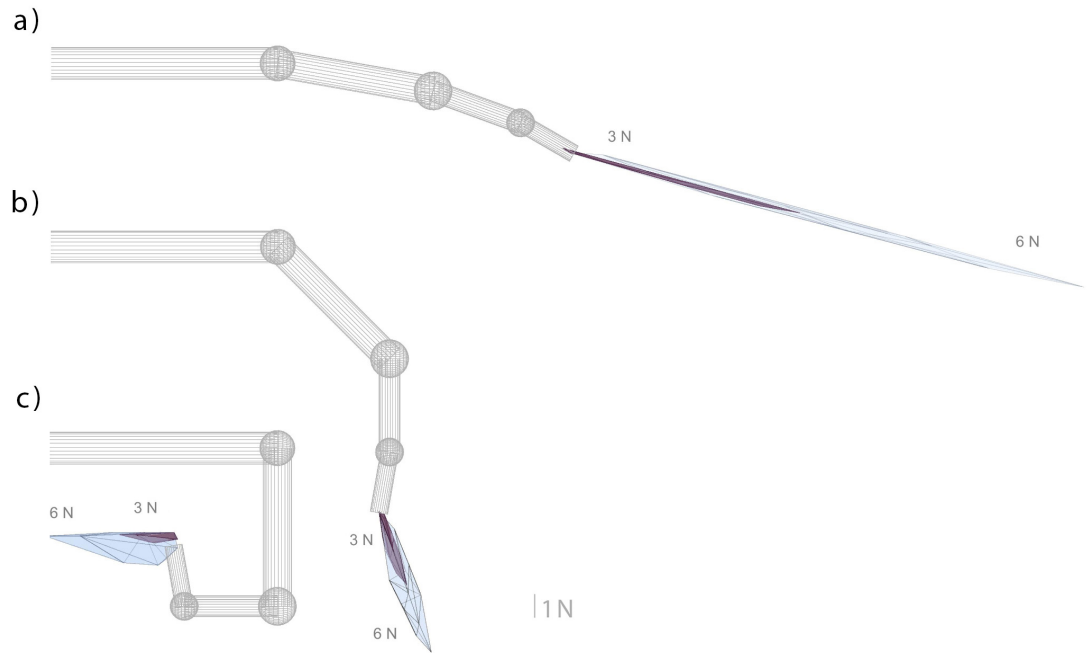


Figure 83. The FFS produced by a membrane EM model in three postures: (a) extension, (b) mid-flexion, (c) full flexion. The FFSs related to low activation force level is shown in purple, the FFSs, related to high activation level are shown in blue.

It can be seen from this figure that there is no significant difference concerning the FFS orientation, *i.e.* the direction of the maximal force in FFS stays similar for both levels of muscle activation. For example, in mid-extension, the angle of the maximal force is 21.1° for low activation level and 20.4° for the high one (Figure 83b). However, the shape of FFSs slightly changed when passing from the low activation level to high one for all postures. These results are comparable with those from the individual band model.

In this section, it was shown that the extensor mechanism is a stiff structure, which may elongate up to 5% of its length in normal conditions (Garcia-Elias et al., 1991). In this section, we studied how the EM model behavior depends on the muscle activation level. It was shown that no significant changes of the feasible tendon force set orientation appears neither for the individual band-model nor for membrane model. The shape of the feasible force set may slightly vary with muscle activation level for both models. The main changes of the feasible tendon force set, produced by both models, concern its area, which increases with muscle force activation. That means that the forces in tendons increase proportionally to input muscle forces. These observations confirm the experimental data, reported by (Hurlbut and Adams, 1995).

Conclusion

In this part, a computational environment was created to simulate the biomechanical model of the extensor mechanism. Two topologies of the extensor mechanism were compared:

1. The individual band model, which consist of a net of individual bands;
2. The membrane model, which contains membranes and two layers of intercrossing fibers.

Table 7 compares the both topologies.

Table 7 Comparison of the individual band model with the membrane model.

	Individual band model	Membrane model
Number of points	504	2179
Number of unknown parameters	Low	High
Influence of the intercrossing band length on model output	High	Low
Influence of the posture on model output	High	Low
Influence of the muscle activation level on model output	Low	Low

First of all, the membrane model contains much more points than the individual band model (504 vs. 2179) and as the result, much more unknown parameters to be identified. These unknown parameters may be a source of error if estimated incorrectly.

At the other hand, the membrane model is less sensitive to the variation of the intercrossing band lengths, because it contains a set of intercrossing fibers, unlike the former model, which contains four intercrossing individual bands. Hence, the individual band model is more sensitive to variation of the lengths of intercrossing bands. For some values of the lengths, these bands can become slack, which considerably change the force distribution among the extensor mechanism bands. For the same reason, the individual band model poorly adapts to change of the posture. Hence, if the individual band model was parametrized for the extended finger it can be imprecise in modeling the flexed finger.

Finally, both topologies seem to have a low sensitivity to the muscle activation level, which complies with the experimental data, reported in (Hurlbut and Adams, 1995).

Therefore, the individual band model seems to be an efficient tool to simulate an extensor mechanism in normal or in pathological state at one given posture or in a small range of motion. As this model contains less parameters than the membrane model, it can be parametrized easier than the latter. However, if one aims at modeling the extensor mechanism at wide range of movement, the membrane model is preferable, as it better adapts to the postural variation.

Several assumptions were made, which can limit the model accuracy.

1. *Bones.* The friction between the EM and the surface was not taken into account. Moreover, the bone and joint anatomy was simplified: the bones were modeled as cylinders with spheres at the ends, the joints were modeled as the ideal constraints, and hence the increase of the digit skeleton length with flexion was not taken into account.
2. *Tendons and ligaments.* EM insertions at the base of p_1 were taken into account as posture-independent coefficients. The transverse retinacular ligament was not modeled.
3. *Muscles.* The muscle forces were represented by the vectors directed to the center of the muscle body, or, in the case of the extrinsic *ed*-muscle, the force vector was directed along the long extensor tendon. To increase the model precision the muscle body shift during the flexion should be taken into account. This is particularly true for lumbrical muscles, which shift distally during the finger flexion movement and change the orientation of the force.

The proposed model could be a tool to simulate the EM deformation during finger flexion-extension and could improve the precision of the existing biomechanical finger models in a way to better understand the force transmission in EM. It could be either directly included to finger model or used to recalculate the coefficients in (8) for individual finger posture, muscle force level, and bone geometry. Furthermore, more complex models, representing the EM as a membrane instead of the set of the elastic bands may be created.

General conclusion

The first purpose of the thesis was to estimate the activations of two nearby finger extensor muscles from the mixture of electromyographic signals. We focused on extensors of little and index fingers, which intersect in the forearm, and, therefore, are the sources of mutual crosstalk. The second purpose of the thesis was to build a model of the finger extensor mechanism. In each finger, an extensor mechanism transmits the forces of the corresponding extensor muscle to finger joints.

Figure 84 summarizes the methods, proposed in this thesis:

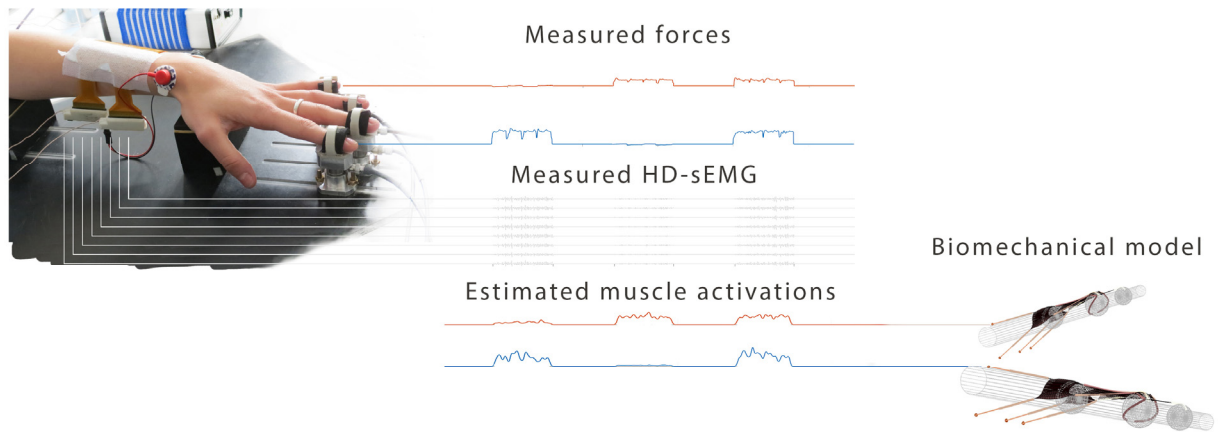


Figure 84. Summary of the proposed methods

The Part 2 of the thesis is devoted to estimation of two nearby muscles activations from the electromyographical signal. For this purpose, we used high-density electromyographical recordings from a matrix of electrodes, placed in a forearm over the intersection area of index and little finger extensors. We proposed a method of estimating the contributions of the extensors muscles from the signals. As a result of the algorithm, the activations of both muscles may be found and used as the entry of the finger biomechanical model. However, before conclusions can be drawn, further researches should be conducted to generalize the method to other biomechanical systems in the human body, especially with muscles that cannot be activated sequentially as currently.

The Part 3 is devoted to modeling of the extensor mechanism of the finger. The extensor mechanism is a complicated structure, transmitting the forces of several extrinsic and intrinsic muscles to finger joints. We created a computation environment, in which two topologies of the extensor mechanism were compared: an individual band model and a membrane model. Furthermore, a parametrization algorithm was created. This algorithm has been used to estimate the model parameters, which makes the force transmission among the extensor mechanism bands fit the experimental data. As a conclusion, it can be proposed that there is no a better model than another one. Individual and membrane models have their own limits each. We suppose that individual-band model seems to be more appropriated for studying a fixed posture, either in normal or pathological conditions (e.g. swan-neck or boutonniere deformity). The individual-band has a low number of unknown parameters, hence the parametrization of this model may be

easily performed. The membrane model runs well when simulation of finger movement in wide range of joint angles is required. This model contains two wide layers of intercrossing fibers, in contrast to the individual band model, which has only four intercrossing bands. During the finger movement, the fiber layers can transmit the muscle force even for the postures, in which individual-band model becomes slack. Moreover, such a topology of a membrane model corresponds to anatomical data (Leijnse and Spoor, 2012; R. Schultz et al., 1981)

As a future work, firstly, the precision of the firing sequence reconstruction from the mixture must be improved. It may be achieved, for example, by fusion of information about muscle activation, received from all matrix channels.

Secondly, a model, linking the estimated firing sequences with muscle activations and forces must be proposed. For that purpose, different solutions may be engaged. One of the possible solutions may be to reconstruct the firing sequences of the MUAPs in each muscle and convolute them with the mechanical impulse response of the muscle (twitch, see Figure 5 in introduction).

Finally, the proposed extensor mechanism models must be validated. For that purpose, studies in controlled environment with cadaveric data are planned to validate deformations and force transmission.

Moreover, the proposed method of the muscle activation estimation, as well as the biomechanical model of the extensor mechanism, may be used for solving the inverse biomechanical problem, *i.e.*, to calculate the muscle forces when the fingertip force is known. The EMG-assisted approach of solving the inverse biomechanical problem was proposed by (Vigouroux et al., 2007). It required the needle EMG recordings from the active muscles to make the first approximation of their force. Then the forces in all muscles, involved into production of the fingertip force, were searched in the neighborhood of the EMG-estimated forces by minimizing the overall muscle stress. The proposed algorithm of the muscle force estimation may be used in the described procedure to replace the needle EMG, which has a number of limitations due to its invasiveness. Furthermore, the proposed extensor mechanism model may be also taken into account for solving the inverse problem to improve the accuracy of the force estimations.

References

- Botter, A., Marateb, H.R., Afsharipour, B., Merletti, R., 2011. Solving EMG-force relationship using Particle Swarm Optimization. *Proc. Annu. Int. Conf. IEEE Eng. Med. Biol. Soc. EMBS* 3861–3864. [doi:10.1109/IEMBS.2011.6090959](https://doi.org/10.1109/IEMBS.2011.6090959)
- Botterman, B.R., Iwamoto, G.A., Gonyea, W.J., 1986. Gradation of isometric tension by different activation rates in motor units of cat flexor carpi radialis muscle. *J. Neurophysiol.* 56, 494–506. [doi:10.1152/jn.1986.56.2.494](https://doi.org/10.1152/jn.1986.56.2.494)
- Brook, N., Mizrahi, J., Shoham, M., Dayan, J., 1995. A biomechanical model of index finger dynamics. *Med. Eng. Phys.* 17, 54–63. [doi:10.1016/1350-4533\(95\)90378-O](https://doi.org/10.1016/1350-4533(95)90378-O)
- Buchholz, B., Armstrong, T.J., Goldstein, S.A., 1992. Anthropometric data for describing the kinematics of the human hand. *Ergonomics* 35, 261–273. [doi:10.1080/00140139208967812](https://doi.org/10.1080/00140139208967812)
- Chao, E.Y., 1989. *Biomechanics of the Hand: A Basic Research Study*. World Scientific.
- Chao, E.Y., Cooney, W.P., Linscheid, L., 1978. Normative model of human hand for biomechanical analysis.
- Darowish, M., Brenneman, R., Bigger, J., 2015. Dimensional analysis of the distal phalanx with consideration of distal interphalangeal joint arthrodesis using a headless compression screw. *Hand* 100–104. [doi:10.1007/s11552-014-9679-x](https://doi.org/10.1007/s11552-014-9679-x)
- de Luca, C.J., 1997. The use of surface electromyography in biomechanics. *J. Appl. Biomech.* 13, 135–163. [doi :10.1123/jab.13.2.135](https://doi.org/10.1123/jab.13.2.135)
- Dogadov, A., Alamir, M., Serviere, C., Quaine, F., 2017. The biomechanical model of the long finger extensor mechanism and its parametric identification. *J. Biomech.* [doi:10.1016/j.jbiomech.2017.04.030](https://doi.org/10.1016/j.jbiomech.2017.04.030)
- Doyle, J.R., 1989. Anatomy of the flexor tendon sheath and pulley system: a current review. *J. Hand Surg. Am.* 14, 349–351.
- Farina, D., Févotte, C., Doncarli, C., Merletti, R., 2004. Blind Separation of Linear Instantaneous Mixtures of Nonstationary Surface Myoelectric Signals. *IEEE Trans. Biomed. Eng.* 51, 1555–1567.
- Farina, D., Fortunato, E., Merletti, R., 2000. Noninvasive Estimation of Motor Unit Conduction Velocity Distribution Using Linear Electrode Arrays 47, 380–388.
- Farina, D., Merletti, R., 2001. A novel approach for precise simulation of the EMG signal detected by surface electrodes. *IEEE Trans. Biomed. Eng.* 48, 637–646. [doi:10.1109/10.923782](https://doi.org/10.1109/10.923782)
- Fenn, W.O., Marsh, B.S., 1935. Muscular force at different speeds of shortening. *J. Physiol.* 85, 277–297. [doi:10.1113/jphysiol.1935.sp003318](https://doi.org/10.1113/jphysiol.1935.sp003318)
- Garcia-Elias, M., An, K.N., Berglund, L., Linscheid, R.L., Cooney, W.P., Chao, E.Y., 1991. Extensor

- mechanism of the fingers. I. A quantitative geometric study. *J. Hand Surg. Am.* 16, 1130–1136.
[doi:10.1016/S0363-5023\(10\)80079-6](https://doi.org/10.1016/S0363-5023(10)80079-6)
- Garcia-Elias, M., An, K.-N., Berglund, L.J., Linscheid, R.L., Cooney, W.P., Chao, E.Y.S., 1991. Extensor mechanism of the fingers. II. Tensile properties of components. *J. Hand Surg. Am.* 16, 1136–1140.
[doi:10.1016/S0363-5023\(10\)80080-2](https://doi.org/10.1016/S0363-5023(10)80080-2)
- Hill, A. V., 1938. The Heat of Shortening and the Dynamic Constants of Muscle. *Proc. R. Soc. B Biol. Sci.* 126, 136–195. [doi:10.1098/rspb.1938.0050](https://doi.org/10.1098/rspb.1938.0050)
- Hill, A. V., 1922. The maximum work and mechanical efficiency of human muscles, and their most economical speed. *J. Physiol.* 56, 19–41. [doi:10.1113/jphysiol.1922.sp001989](https://doi.org/10.1113/jphysiol.1922.sp001989)
- Holobar, A., Farina, D., 2014. Blind source identification from the multichannel surface electromyogram. *Physiol. Meas.* 35, R143–R165. [doi:10.1088/0967-3334/35/7/R143](https://doi.org/10.1088/0967-3334/35/7/R143)
- Hu, D., Ren, L., Howard, D., Zong, C., 2014. Biomechanical Analysis of Force Distribution in Human Finger Extensor Mechanisms. *Biomed Res. Int.* 2014.
- Hurlbut, P.T., Adams, B.D., 1995. Analysis of finger extensor mechanism strains. *J. Hand Surg. Am.* 20, 832–840. [doi:10.1016/S0363-5023\(05\)80439-3](https://doi.org/10.1016/S0363-5023(05)80439-3)
- Jiang, N., Farina, D., 2011. Covariance and time-scale methods for blind separation of delayed sources. *IEEE Trans. Biomed. Eng.* 58, 550–556. [doi:10.1109/TBME.2010.2084999](https://doi.org/10.1109/TBME.2010.2084999)
- Kandel, E.R., Jessell, T.M., Schwartz, J.H., Siegelbaum, S.A., Hudspeth, A.J., 2013. Principles of Neural Science, Fifth Edition, Principles of Neural Science. McGraw-Hill Education.
- Kay, S.M., 1993. Fundamentals of Statistical Signal Processing : Estimation Theory. Prentice-Hall.
- Landsmeer, J.M.F., 1976. Atlas of Anatomy of the Hand. Churchill Livingstone, Edinburgh; London; New York.
- Laterza, F., Olmo, G., 1997. Analysis of EMG signals by means of the matched wavelet transform. *Electron. Lett.* 33, 357. [doi:10.1049/el:19970250](https://doi.org/10.1049/el:19970250)
- Lee, H.B., 1975. A Novel Procedure for Assessing the Accuracy of Hyperbolic Multilateration Systems. *IEEE Trans. Aerosp. Electron. Syst.* 11, 2–15.
- Leijnse, J.N. a L., Spoor, C.W., 2012. Reverse engineering finger extensor apparatus morphology from measured coupled interphalangeal joint angle trajectories - a generic 2D kinematic model. *J. Biomech.* 45, 569–578. [doi:10.1016/j.jbiomech.2011.11.002](https://doi.org/10.1016/j.jbiomech.2011.11.002)
- Leijnse, J.N.A.L., Carter, S., Gupta, A., McCabe, S., 2008. Anatomic Basis for Individuated Surface EMG and Homogeneous Electrostimulation With Neuroprostheses of the Extensor Digitorum Communis 64–75. [doi:10.1152/jn.00706.2007](https://doi.org/10.1152/jn.00706.2007)

- Léouffre, M., Quaine, F., Servière, C., 2013. Testing of instantaneity hypothesis for blind source separation of extensor indicis and extensor digiti minimi surface electromyograms. *J. Electromyogr. Kinesiol.* 23, 908–15. [doi:10.1016/j.jelekin.2013.03.009](https://doi.org/10.1016/j.jelekin.2013.03.009)
- Li, Z.M., Zatsiorsky, V.M., Latash, M.L., 2000. Contribution of the extrinsic and intrinsic hand muscles to the moments in finger joints. *Clin. Biomech.* 15, 203–211. [doi:10.1016/S0268-0033\(99\)00058-3](https://doi.org/10.1016/S0268-0033(99)00058-3)
- Merletti, R., Holobar, A., Farina, D., 2008. Analysis of motor units with high-density surface electromyography. *J. Electromyogr. Kinesiol.* 18, 879–90. [doi:10.1016/j.jelekin.2008.09.002](https://doi.org/10.1016/j.jelekin.2008.09.002)
- Merletti, R., Parker, P.A., 2004. *Electromyography. Physiology, Engineering, and Noninvasive Applications.*
- Merletti, R., Parker, P.A., Parker, P.J., 2004. *Electromyography: Physiology, Engineering, and Non-Invasive Applications*, IEEE Press Series on Biomedical Engineering. Wiley.
- Mesin, L., Smith, S., Hugo, S., Viljoen, S., Hanekom, T., 2009. Effect of spatial filtering on crosstalk reduction in surface EMG recordings. *Med. Eng. Phys.* 31, 374–383. [doi: 10.1016/j.medengphy.2008.05.006](https://doi.org/10.1016/j.medengphy.2008.05.006)
- Monster, A.W., Chan, H., 1980. Surface Electromyogram Potentials of Motor Units ; Relationship between Potential Size and Unit Location in a Large Human Skeletal Muscle 297, 280–297.
- Moutet, F., 2003. Les poulies de l'appareil fléchisseur: Anatomie, pathologies, traitement. *Chir. Main* 22, 1–12. [doi: 10.1016/S1297-3203\(02\)00010-0](https://doi.org/10.1016/S1297-3203(02)00010-0)
- Naik, G.R., Selvan, S.E., Nguyen, H.T., 2016. Single-channel EMG classification with ensemble-empirical-mode-decomposition-based ICA for diagnosing neuromuscular disorders. *IEEE Trans. Neural Syst. Rehabil. Eng.* 24, 734–743. [doi: 10.1109/TNSRE.2015.2454503](https://doi.org/10.1109/TNSRE.2015.2454503)
- Paclet, F., Quaine, F., 2012. Motor control theories improve biomechanical model of the hand for finger pressing tasks. *J. Biomech.* 45, 1246–51. [doi: 10.1016/j.jbiomech.2012.01.038](https://doi.org/10.1016/j.jbiomech.2012.01.038)
- Qian, K., Traylor, K., Lee, S.W., Ellis, B., Weiss, J., Kamper, D., 2014. Mechanical properties vary for different regions of the finger extensor apparatus. *J. Biomech.* 47, 3094–3099. [doi:10.1016/j.jbiomech.2014.06.035](https://doi.org/10.1016/j.jbiomech.2014.06.035)
- Schultz, R.J., Furlong, J., Storace, a, 1981. Detailed anatomy of the extensor mechanism at the proximal aspect of the finger. *J. Hand Surg. Am.* 6, 493–498. [doi: 10.1016/S0363-5023\(81\)80110-4](https://doi.org/10.1016/S0363-5023(81)80110-4)
- Schweitzer, T.P., Rayan, G.M., 2004. The terminal tendon of the digital extensor mechanism: Part I, anatomic study. *J. Hand Surg. Am.* 29, 903–908. [doi:10.1016/j.jhsa.2004.04.025](https://doi.org/10.1016/j.jhsa.2004.04.025)
- Shrewsbury, M.M., Johnson, R.K., 1977. A systematic study of the oblique retinacular ligament of the human finger: its structure and function. *J. Hand Surg. Am.* 2, 194–199. [doi:10.1016/S0363-5023\(77\)80069-5](https://doi.org/10.1016/S0363-5023(77)80069-5)

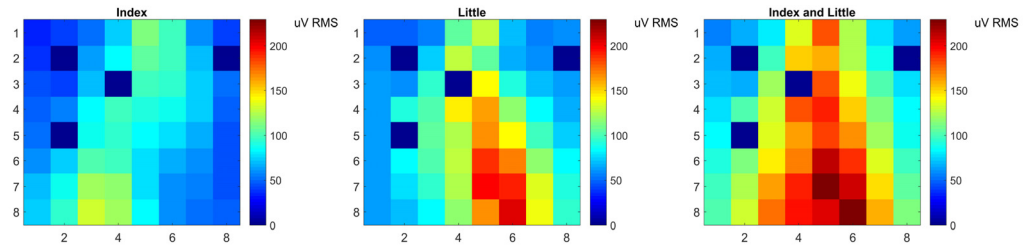
- Stack, H.G., 1963. A study of muscle function in the fingers. *Ann. R. Coll. Surg. Engl.* 33, 307–322.
- Theobald, P.S., Dowson, D., Khan, I.M., Jones, M.D., 2012. Tribological characteristics of healthy tendon. *J. Biomech.* 45, 1972–1978. [doi:10.1016/j.jbiomech.2012.05.005](https://doi.org/10.1016/j.jbiomech.2012.05.005)
- Valero-Cuevas, F.J., 2015. *Fundamentals of Neuromechanics, Biosystems & Biorobotics*. Springer London, London. [doi:10.1007/978-1-4471-6747-1](https://doi.org/10.1007/978-1-4471-6747-1)
- Valero-Cuevas, F.J., Yi, J.W., Brown, D., McNamara, R. V., Paul, C., Lipson, H., 2007. The tendon network of the fingers performs anatomical computation at a macroscopic scale. *IEEE Trans. Biomed. Eng.* 54, 1161–1166. [doi:10.1109/TBME.2006.889200](https://doi.org/10.1109/TBME.2006.889200)
- Vigouroux, L., Quaine, F., Labarre-Vila, A., Amarantini, D., Moutet, F., 2007. Using EMG data to constrain optimization procedure improves finger tendon tension estimations during static fingertip force production. *J. Biomech.* 40, 2846–2856. [doi:10.1016/j.jbiomech.2007.03.010](https://doi.org/10.1016/j.jbiomech.2007.03.010)
- Zajac, F.E., 1989. Muscle and tendon: properties, models, scaling, and application to biomechanics and motor control. *Crit. Rev. Biomed. Eng.* 17, 359–411.
- Zancolli, E., 1979. *Structural and Dynamic Bases of Hand Surgery*. J.B. Lippincott Company, Philadelphia; Toronto.
- Chao, E.Y.S., An, K.-N., Cooney III, W.P., Linscheid, R.L., 1989. *Biomechanics of the hand. A basic research study*. World Scientific, Singapore.

Annex. Experimental data

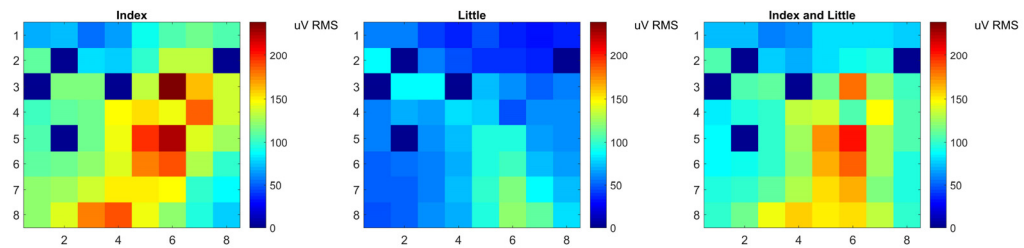
RMS maps

This part contains the RMS maps for ten subjects during the extension of index, little finger and instantaneous extension of index and little finger.

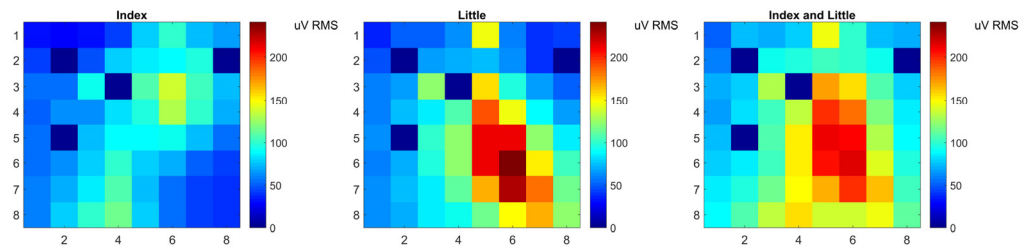
Subject #1



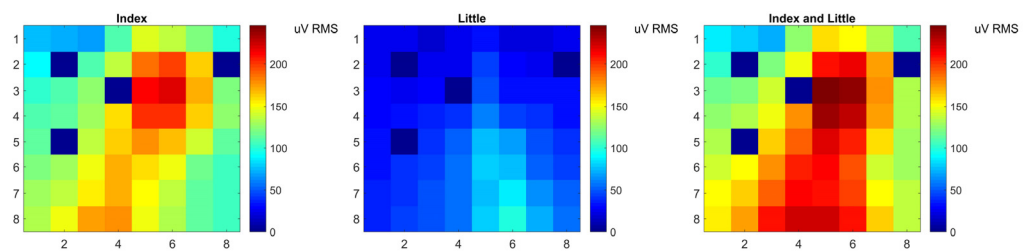
Subject #2



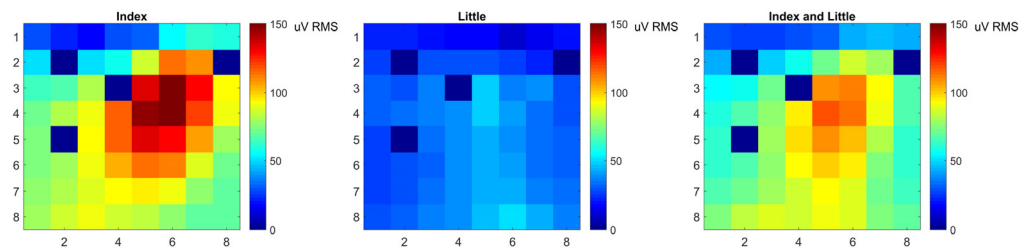
Subject #3



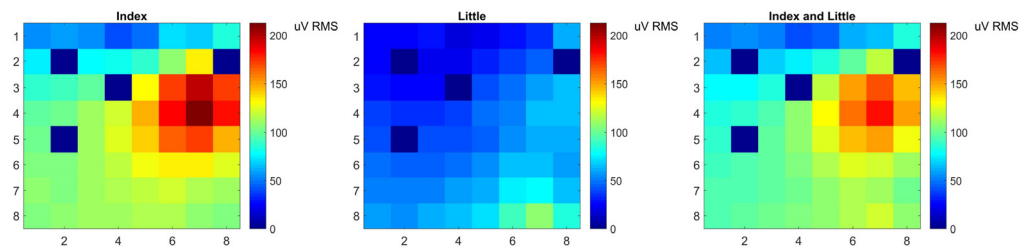
Subject #4



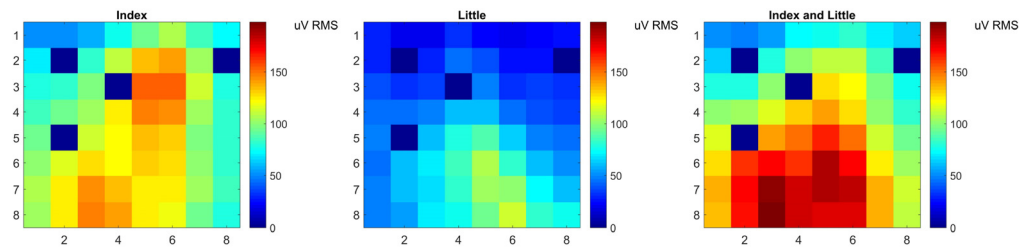
Subject #5



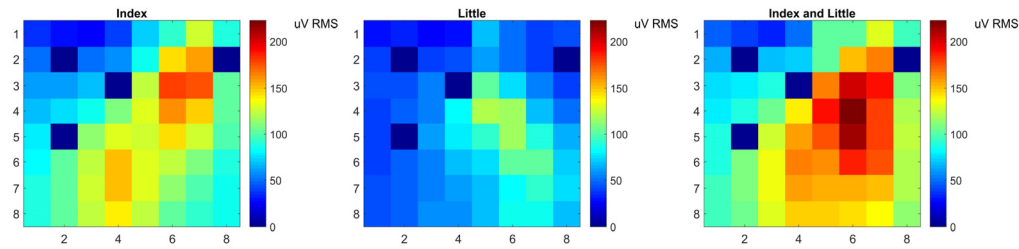
Subject #6



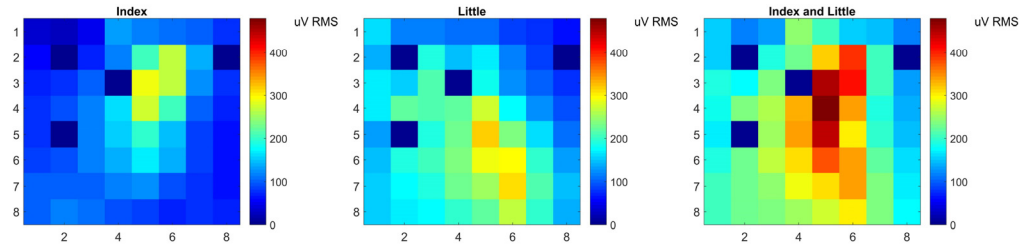
Subject #7



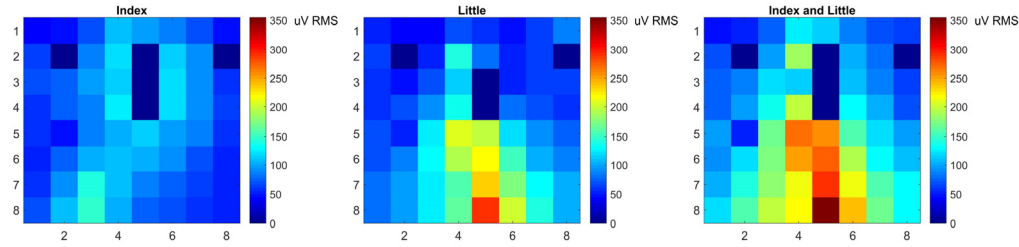
Subject #8



Subject #9



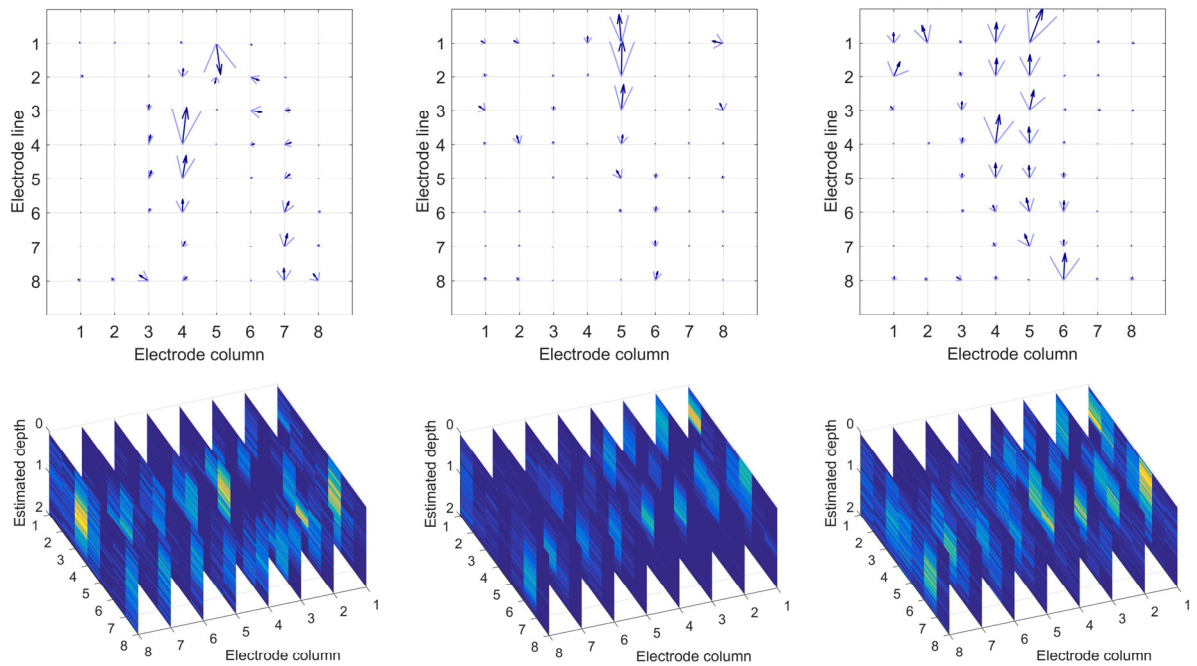
Subject #10



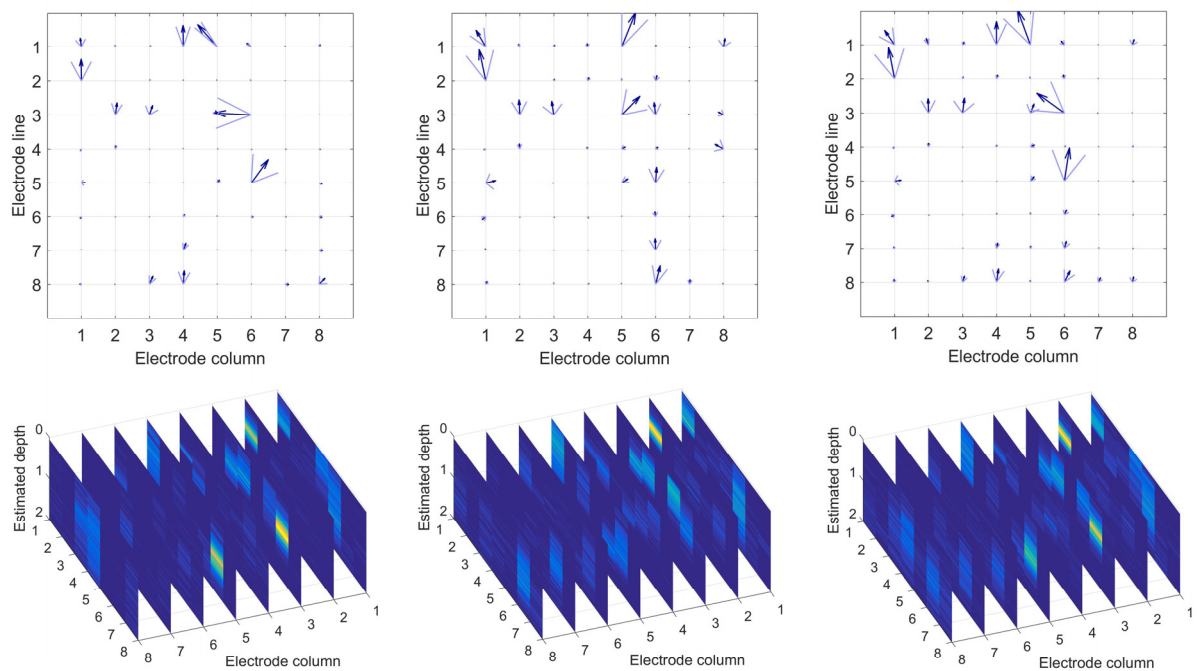
Estimated features

This part contains the estimated propagation direction and depth for ten subjects during the extension of index, little finger and instantaneous extension of index and little finger.

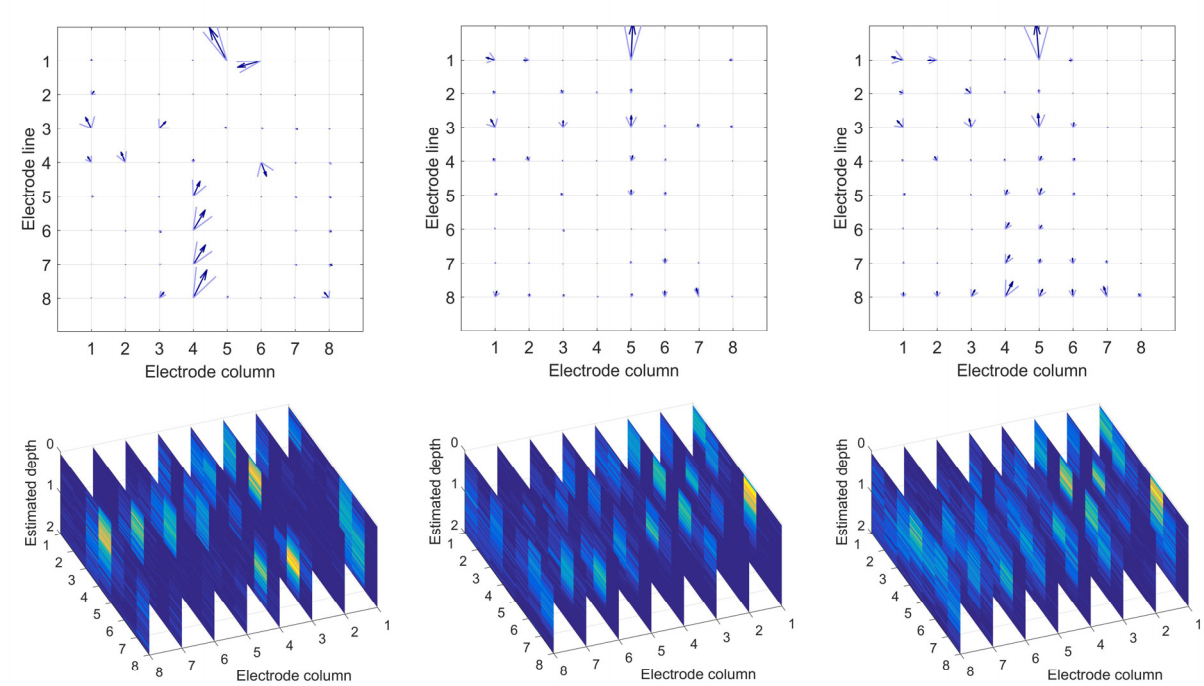
Subject #1



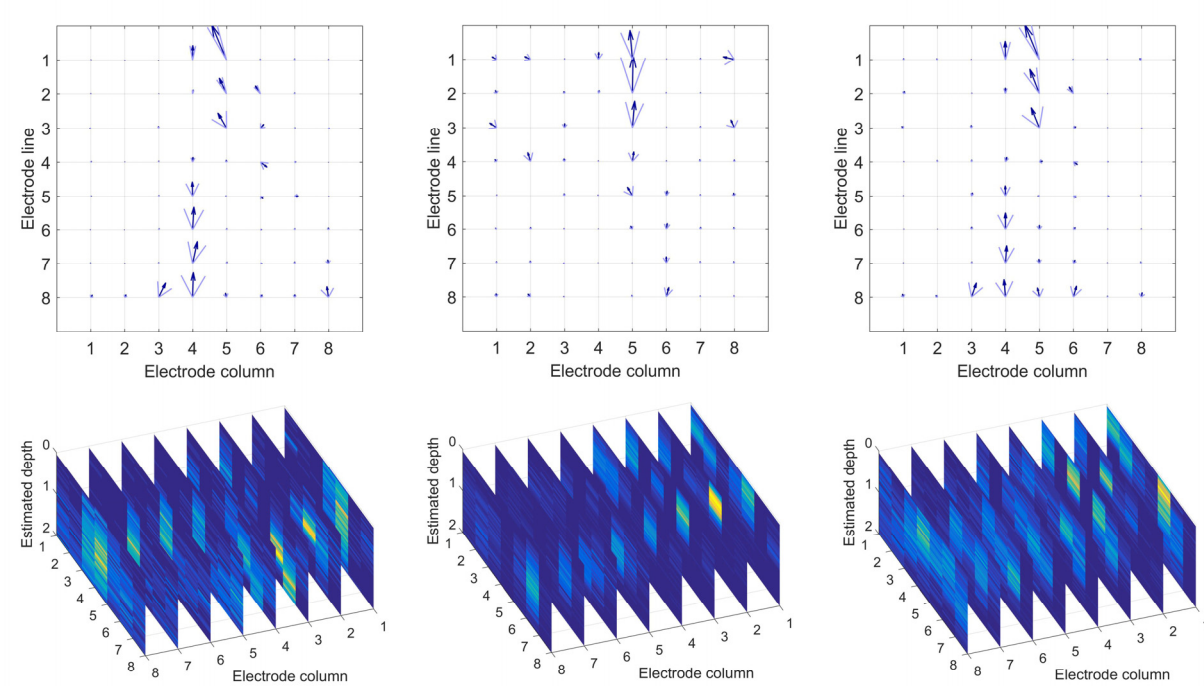
Subject #2



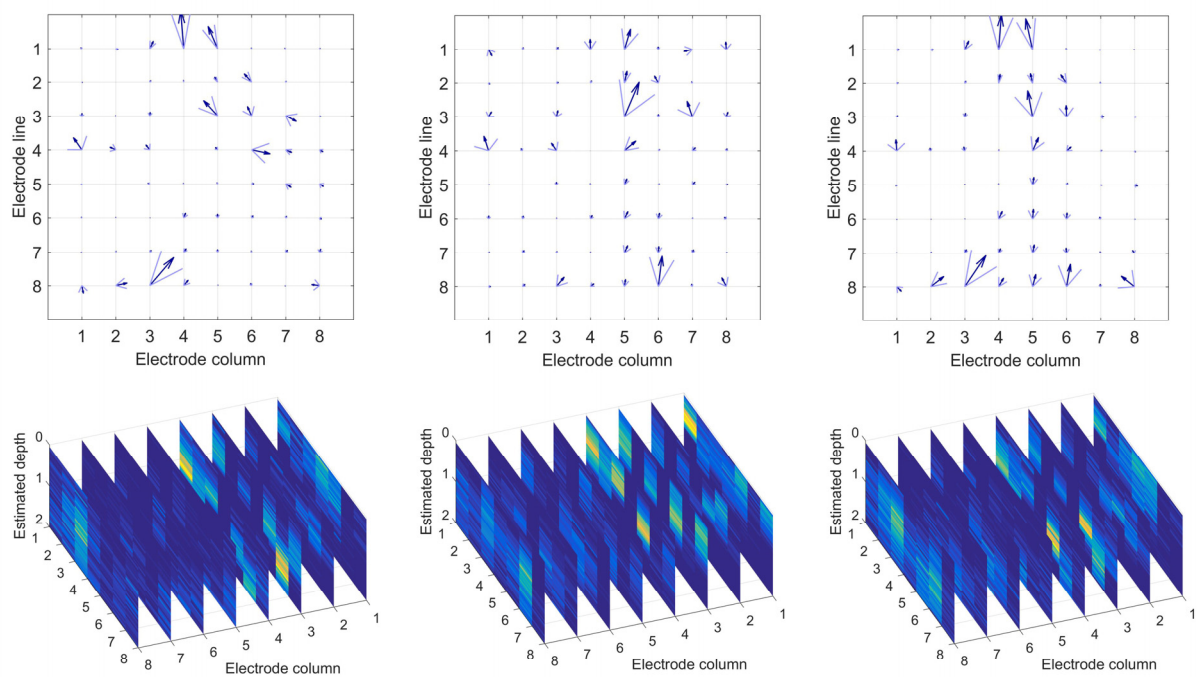
Subject #3



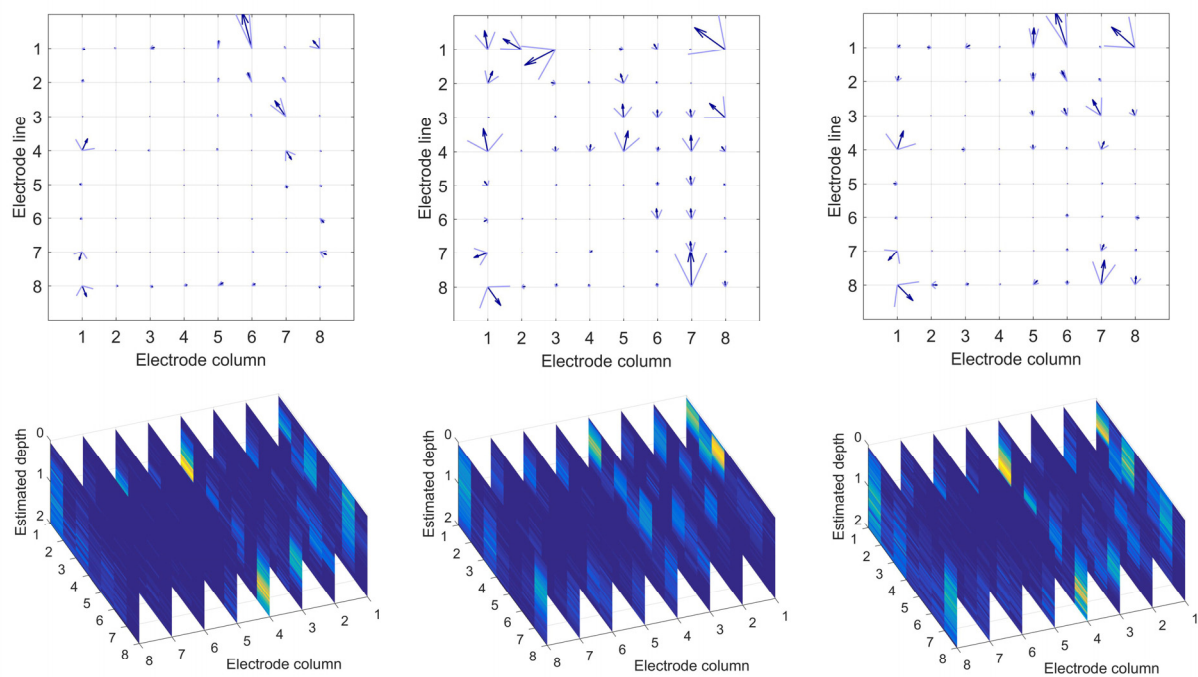
Subject #4



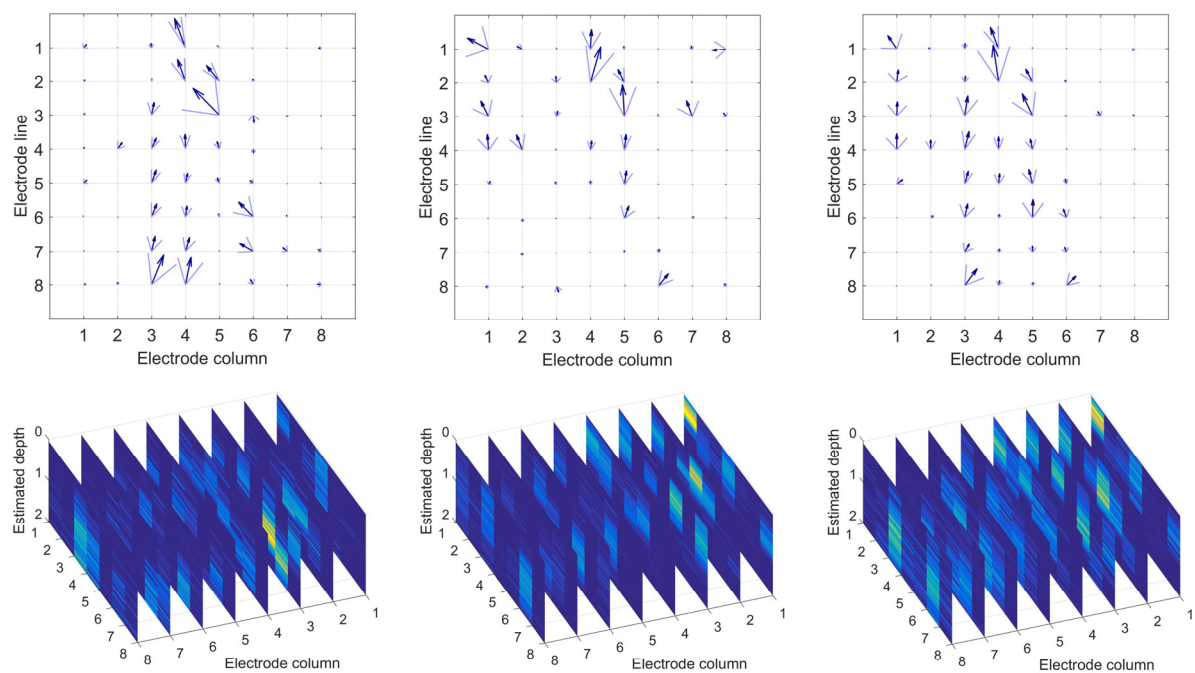
Subject #5



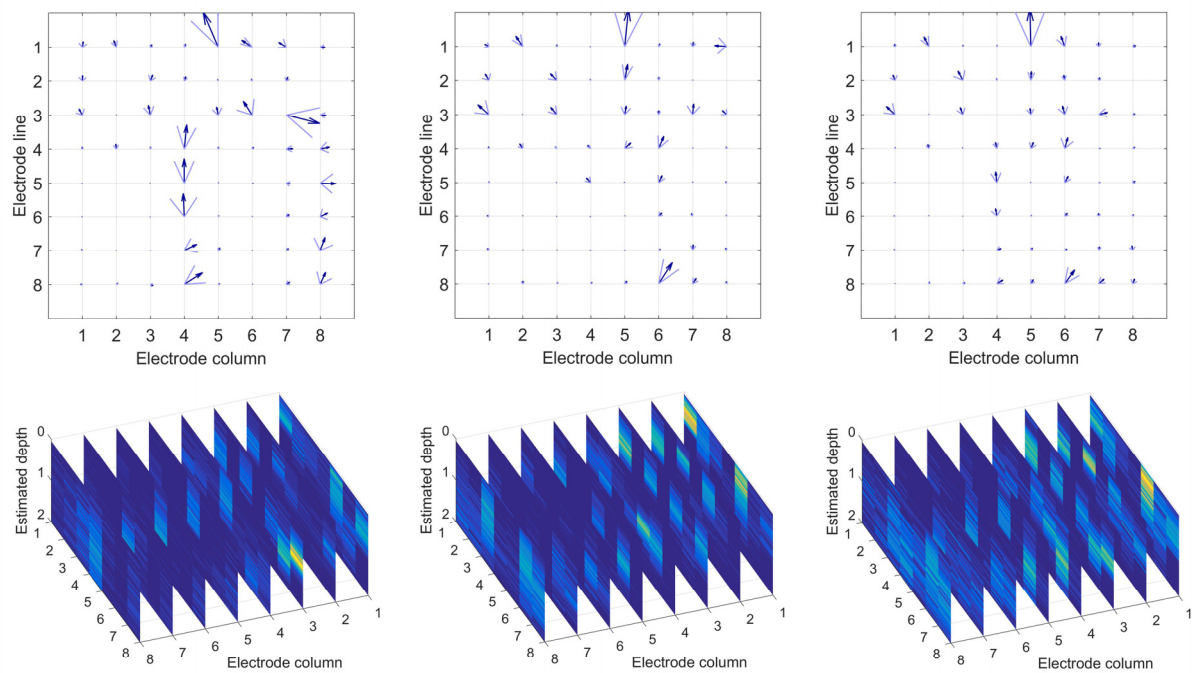
Subject #6



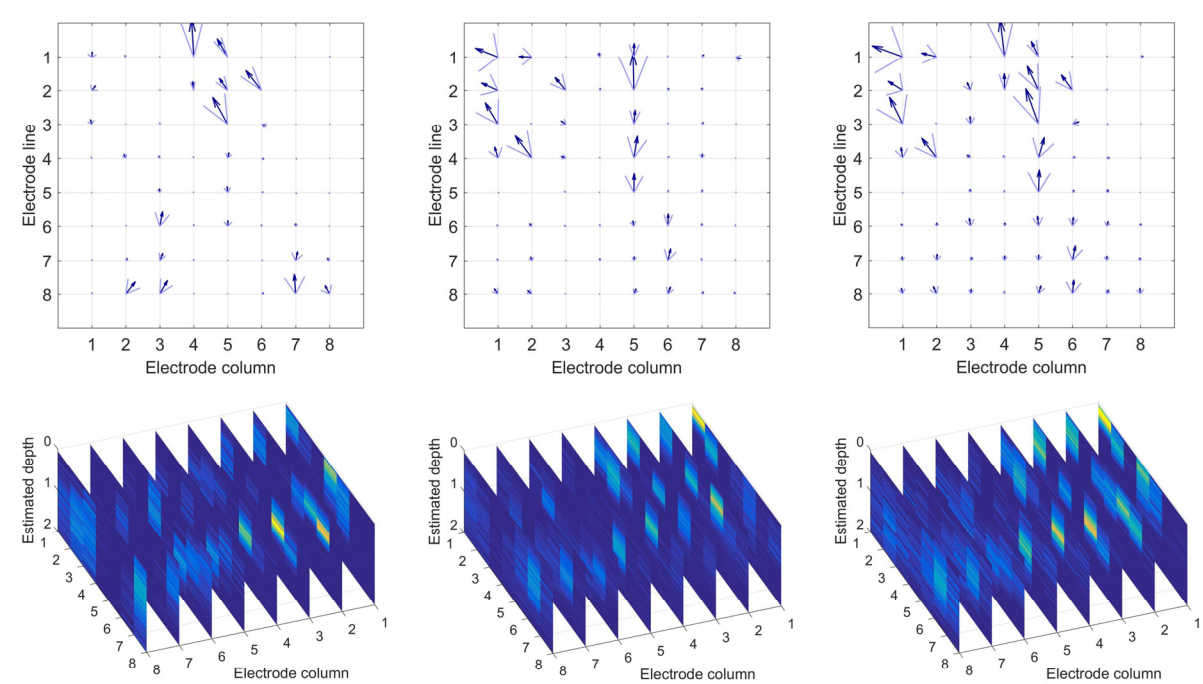
Subject #7



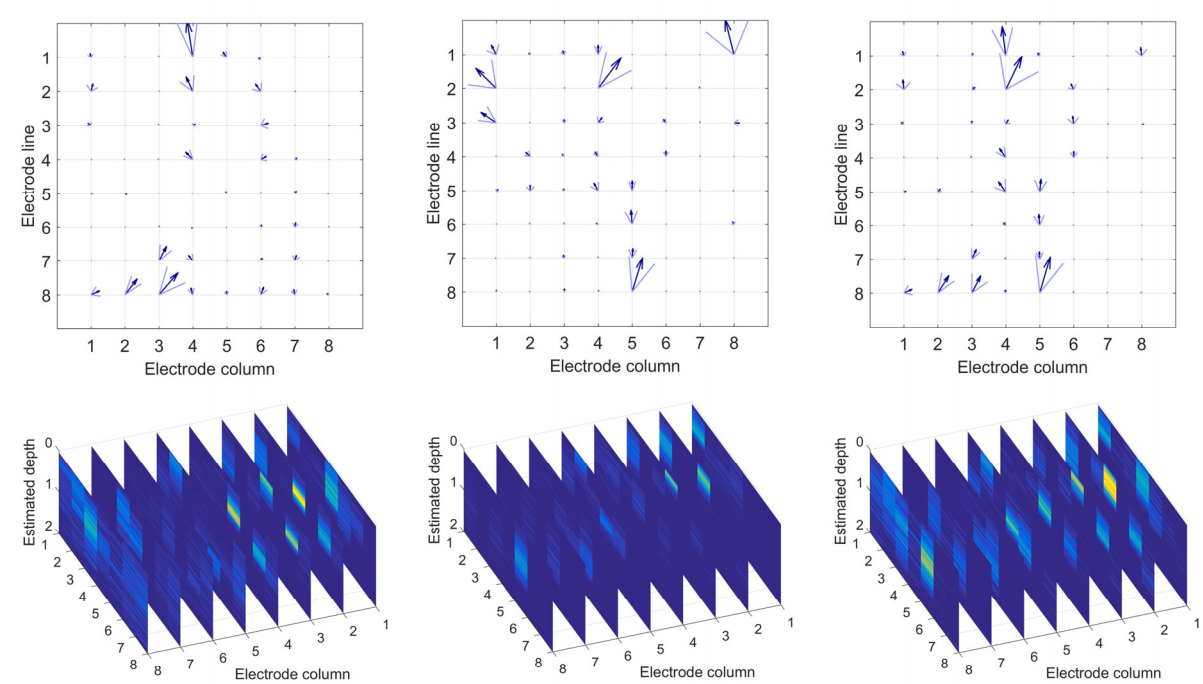
Subject #8



Subject #9

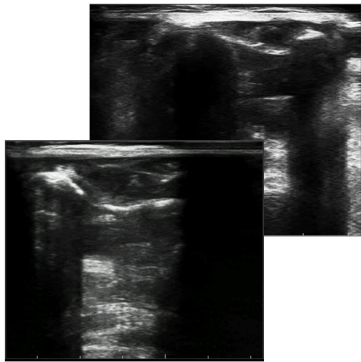


Subject #10

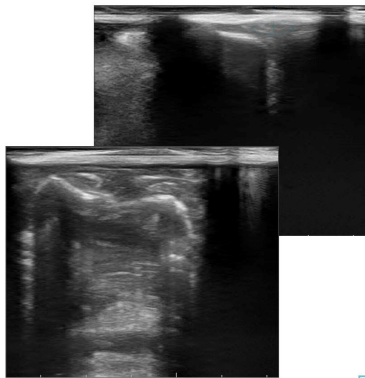


Ultrasonic images

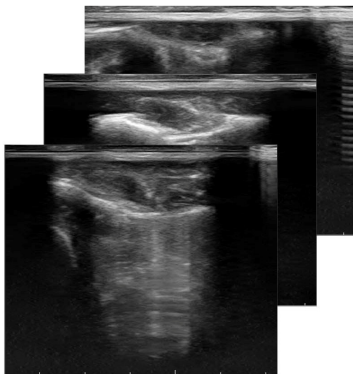
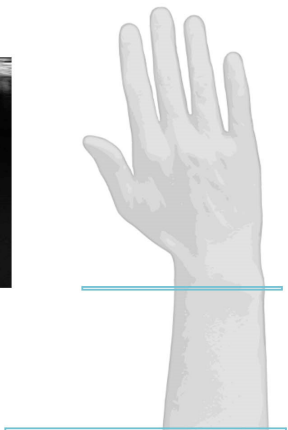
This part contains the ultrasonic images from all subjects. For the subjects #1, 2, 9, and 10 only two sections were visualized.



Subject #1



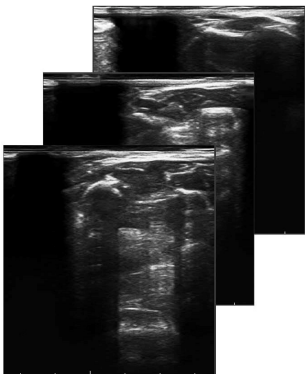
Subject #2



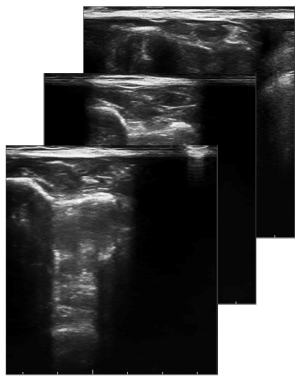
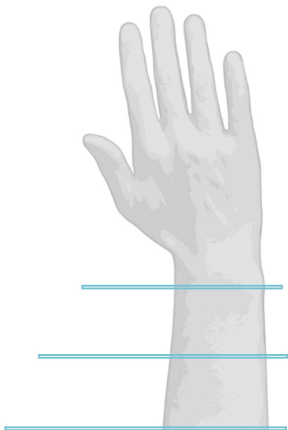
Subject #3



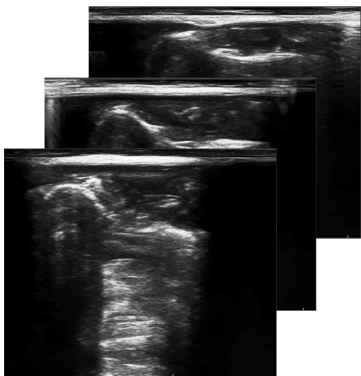
Subject #4



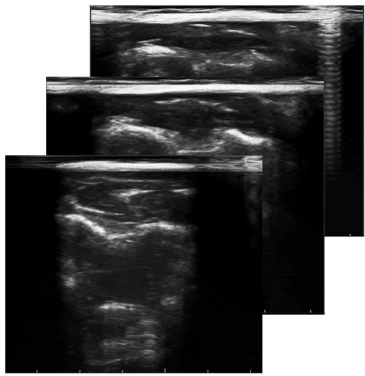
Subject #5



Subject #6

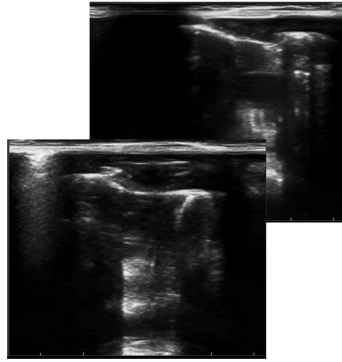


Subject #7

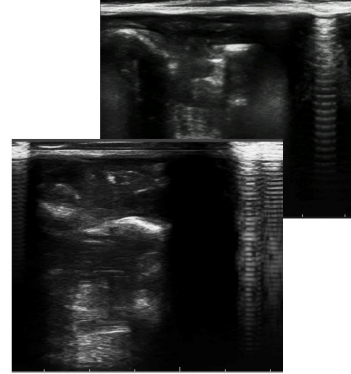


Subject #8

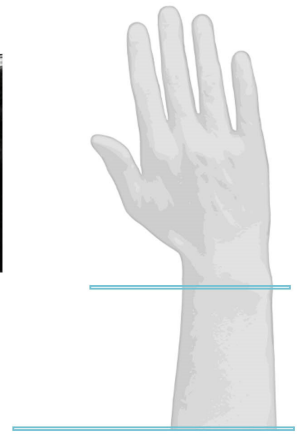




Subject #9



Subject #10



Résumé — Les signaux électromyographiques de surface (sEMG) correspondent aux signaux électriques composés par les potentiels d'action produits par les unités motrices d'un muscle actif et enregistrés par des électrodes de surface. Les signaux sEMG sont largement utilisés dans la médecine, le contrôle des prothèses et plus généralement dans les études biomécaniques portant sur l'analyse du mouvement humain. Les signaux sEMG sont très souvent utilisés comme un indicateur d'activation musculaire.

Bien que présentant un intérêt évident, l'utilisation de ces signaux reste difficile compte tenu qu'ils sont souvent susceptibles d'interférence (diaphonie, ou plus communément « cross-talk ») entre les muscles contigus, parfois même éloignés. Cette contamination croisée est particulièrement présente pour des muscles présents dans un volume restreint, ce qui est le cas des muscles extenseur de l'index et du petit doigt, extensor indicis et extensor digiti minimi. Afin que les signaux sEMG puissent être utilisés de manière plus robuste en biomécanique, il convient de réduire cette interférence avant de procéder à l'estimation des activations musculaires. Les activations individuelles des muscles participant au mouvement correctement estimées peuvent être utilisées comme données d'entrées d'un modèle biomécanique. Ainsi, l'objectif de ce travail de thèse était double : (1) améliorer l'estimation activations musculaires à partir des mélanges des sEMG des muscles extensor indicis et extensor digiti minimi, et (2) modélisation biomécanique du mécanisme extenseur du doigt.

Pour cela, les signaux sEMG ont été enregistrés avec une matrice d'électrodes de surface haute densité à 64 capteurs. Ensuite, l'extraction des activations musculaires a été réalisée sur la base d'une procédure de classification des potentiels détectés en utilisant les invariants musculaires que sont la direction de propagation et la profondeur de l'unité motrice à l'origine du signal.

Dans un deuxième temps, un modèle biomécanique précis du mécanisme extenseur du doigt a été créé, qui contient les tendons et les principaux ligaments représentés par des bandes et des surfaces élastiques. Un algorithme de paramétrage du modèle a été proposé. Ce type d'approche est nécessaire pour mieux décrire les déformations du système anatomique dans des situations de mouvement sain ou pathologique.

Au final, l'association des activations musculaires et du modèle du doigt avec le mécanisme extenseur correctement modélisé a été utilisée pour calculer la force externe produite au bout du doigt. Les déformations des structures tendineuses observées pour certaines pathologies sont également décrites. Cette démarche a montré qu'elle était pertinente pour l'étude biomécanique du doigt. Elle présente des utilisations judicieuses pour les études biomécaniques portant sur l'optimisation de l'évaluation clinique, l'adaptation de la réhabilitation et le contrôle des prothèses myoélectriques.

Mots-clés : Electromyographie ; Séparation de sources ; Mécanisme extenseur du doigt ; Modélisation Biomécanique

Abstract — The surface electromyographic signals (SEMG) are the electric signals, composed of electric potentials. These potentials are produced by the recruited motor units of an active muscle and captured by the surface electrodes. The SEMG signals are widely used in medicine, prosthesis control, and biomechanical studies as an indicator of muscle activity.

However, SEMG measurements are usually subjects of crosstalk or interference from nearby muscles. It appears when two or more nearby muscles are active during a SEMG recording. An example of such muscles are the extensors of index and little finger, extensor indicis and extensor digiti minimi, situated close to each other and creating a significant amount of mutual crosstalk when simultaneously active. The crosstalk causes precision decrease of SEMG-based estimation of muscle activations. Hence, the crosstalk-reducing problem must be preliminary solved before muscle activation evaluation.

Once the activations of individual finger muscles are estimated from the mixture, they may be used as an input of a finger biomechanical model to calculate a fingertip force. These models usually take into account an extensor mechanism of the finger, which is a structure, transmitting the force from the extensor muscles to the finger joints. This structure is often represented as a set of coefficients. However, there is a lack of study about how these coefficients vary with posture, applied force, and subject variability.

The purpose of this work is to improve the finger force estimation from the crosstalk-contaminated signals for isometric tasks by extracting the activations of individual muscles and improving the finger biomechanical model. Firstly, the SEMG signals were recorded with high-density surface electromyographic (HD-EMG) electrode matrix. The extraction of individual muscle activation was based on classifying the detected potentials according to their propagation direction and depth of originating motor unit.

Secondly, a precise biomechanical model of the finger extensor mechanism was created, containing the principal tendons and ligaments, which are represented by a set of elastic bands and convex surfaces. The algorithm of the model parametrization was proposed as well. The proposed methods of muscle activation estimation along with the created extensor mechanism model may be used for calculating the fingertip force and internal tissues deformations for normal or pathological fingers. These methods can be applied to biomechanical studies as well as find a use in hand rehabilitation or prosthesis control.

Keywords : Multi-channel EMG ; Motor unit action potentials ; HD-sEMG technique ; Source separation ; Extensor mechanism ; Biomechanical modeling
